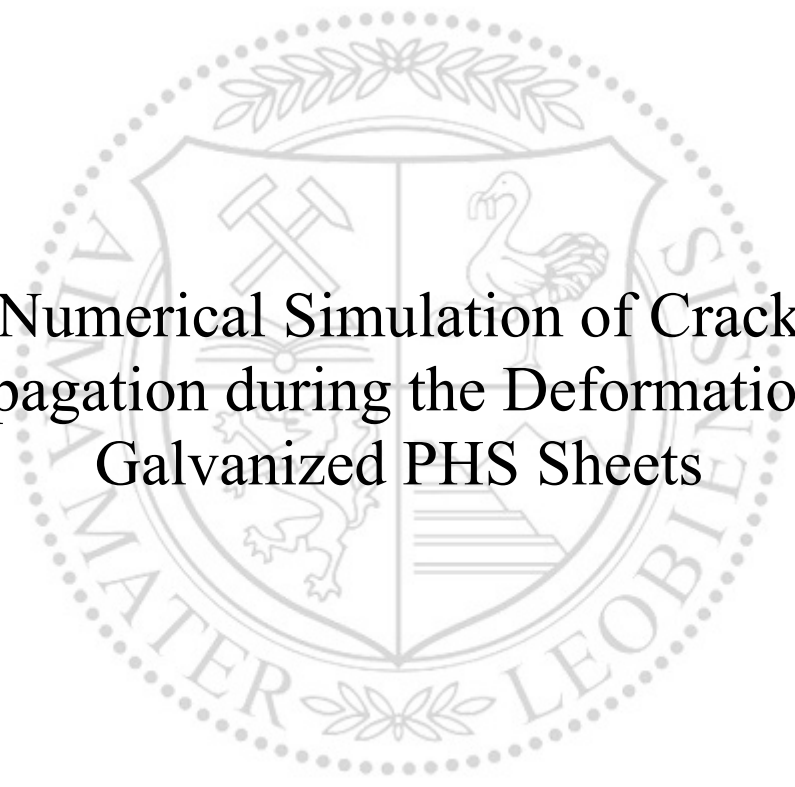




Chair of Mechanics

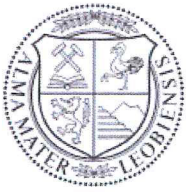
Master's Thesis

The background features a large, faint watermark of the University of Leoben seal. The seal is circular and contains a shield with various symbols, including a hammer and pickaxe, a swan, and a lion. The text 'UNIVERSITAS LEOBENSIS' is visible around the perimeter of the seal.

Numerical Simulation of Crack  
Propagation during the Deformation of  
Galvanized PHS Sheets

Philipp Jörg Hammer, BSc

September 2020



**EIDESSTÄTLICHE ERKLÄRUNG**

Ich erkläre an Eides statt, dass ich diese Arbeit selbständig verfasst, andere als die angegebenen Quellen und Hilfsmittel nicht benutzt, und mich auch sonst keiner unerlaubten Hilfsmittel bedient habe.

Ich erkläre, dass ich die Richtlinien des Senats der Montanuniversität Leoben zu "Gute wissenschaftliche Praxis" gelesen, verstanden und befolgt habe.

Weiters erkläre ich, dass die elektronische und gedruckte Version der eingereichten wissenschaftlichen Abschlussarbeit formal und inhaltlich identisch sind.

Datum 14.09.2020

---

Unterschrift Verfasser/in  
Philipp Jörg, Hammer

# Acknowledgements

First and foremost I would like to thank my supervisor, Univ.-Prof. Dipl.-Ing. Dr. mont. Thomas Antretter, for his contributions and his advice. Whenever problems arose, he managed to help me out with his immense knowledge on the subject of simulation and he spared no effort, even on vacation, to answer my questions as well as he could.

I would also like to thank my colleague Melanie Tomasch for her insights into the press-hardening model she developed and general help she provided, as this thesis is closely related to her work.

Furthermore all my colleagues from the Institute for Mechanics at the Montanuniversity Leoben deserve some acknowledgement. Alike Thomas and Melanie, Manuel Schemmel steadily provided a reliable source of answers for my questions regarding ABAQUS. But also all my other co-workers made my time at the Institute for Mechanics a very pleasing and remembering one on all the coffees, lunches, ski trips and hiking tours.

My special thanks are of course to my family. My parents always supported me in my studies, my sisters gave great company and insights into other academical fields and my grandparents always lend an ear to my problems.

Of course, my girlfriend Eva-Maria Leitner deserves special thanks as she had to endure my mood when the simulations didn't work, cheered me up on bad days and always kept me going.

Lastly, I want to especially dedicate this work to my two grandparents Gerhart and Ingeborg Bayer. Gerhart worked in a foundry and inspired me to study metallurgy before he died earlier to my inscription. Ingeborg accompanied him on many exhibitions and I had long talks on the phone with her, sharing her wisdom and experiences with me before she passed away just a month earlier. I probably owe more to you than you would have ever known and I miss you sincerely.

# Kurzfassung

Die Entwicklung von neuen Stählen und Verarbeitungsverfahren für die Automobilindustrie ist getrieben von der heutigen Leichtbaumentalität. Leichte Stahlbauteile mit dennoch hervorragender Zähigkeit erfordern eine stetige Erhöhung der Festigkeit. Klassische Kaltumformverfahren und die dabei verwendeten Stähle erreichen eine natürliche Grenze, die von großen Umformkräften und hoher Rückfederung bestimmt wird. Das direkte Presshärten kombiniert die Umformung im heißen Zustand mit einer gleichzeitigen Härtung im Umformgesenk und reduziert damit die Umformkräfte und Rückfederung, während die Festigkeit gesteigert werden kann. Aus Gründen des Korrosionsschutzes sind die eingesetzten Bleche aber meist schon vor der Umformung verzinkt und besitzen somit eine erhöhte Rissneigung.

Das Ziel dieser Arbeit ist daher die Entwicklung eines numerischen Modells, welches zur Studie des Rissfortschrittes im Presshärteprozess herangezogen werden kann. Einer Einführung in die Herstellung verzinkter, pressgehärteter Bleche folgt eine Beschreibung der verwendeten Legierung sowie der Zinkschicht. Eine Zusammenfassung der Modellierungsmöglichkeiten von Rissen im Finite Elemente Programm ABAQUS beschließt den Theorieteil. Durch die Implementierung verschiedener Rissmodellierungstechniken in ein Dreipunktbiegemodell wird der bestmögliche Ansatz ermittelt. Dieser findet schlussendlich Verwendung in einem Submodell, welches zur Beschreibung des Rissfortschrittes in einer bereits existierenden Simulation eines Presshärteprozesses eingesetzt wird. Zuletzt werden verschiedene Positionen des Presshärtemodells auf ihr Rissverhalten untersucht und die Erkenntnisse des Modellerstellungsprozesses evaluiert.

# Abstract

In the automotive industry, the development of advanced steels and production techniques is driven by the desire to produce ever lighter parts while still maintaining good crashworthiness. In order to produce lightweight steel parts, their strength has to be enhanced. For the common steels used in cold forming processes, large forming forces and springback set an upper limit. The direct press-hardening process combines the forming in hot condition with a subsequent hardening step, therefore lowering forming forces and springback while still enhancing the material strength. However, for reasons of corrosion prevention, the formed blanks are usually already zinc-coated and entail the risk of cracking during deformation.

Hence, this thesis aims to develop a numerical model for the investigation of crack propagation during press-hardening. A theoretical description on the production process of press-hardened car parts is followed by a specification on the used alloy and zinc-layer modifications. The theoretical chapter is closed by a summary of crack modelling techniques within the finite element program ABAQUS. Through implementation of different crack growth modelling techniques into a three point bending test model, the best approach is determined and later used to describe crack growth in a pre-existing press-hardening simulation by using the submodel technique. Finally, different positions in the press-hardening model are addressed and compared regarding their cracking behaviour, and the findings of the model development process are evaluated.

# Table of Contents

|  |              |
|--|--------------|
| <b>Acknowledgements</b> .....                                    | <b>III</b>   |
| <b>Kurzfassung</b> .....   | <b>IV</b>    |
| <b>Abstract</b> .....  | <b>V</b>     |
| <b>Table of Contents</b> .....                                   | <b>VI</b>    |
| <b>List of Figures</b> .....                                     | <b>VIII</b>  |
| <b>List of Tables</b> .....                                      | <b>XII</b>   |
| <b>Used symbols</b> .....  | <b>XIII</b>  |
| <b>Acronyms</b> .....  | <b>XVIII</b> |
| <b>1 Introduction</b> .....                                      | <b>1</b>     |
| <b>2 Theoretical background</b> .....                            | <b>2</b>     |
| 2.1 Production process for press hardened car parts.....         | 2            |
| 2.1.1 Alloy composition of press hardening steels .....          | 3            |
| 2.1.2 Hot and cold rolling .....                                 | 4            |
| 2.1.3 Galvanizing and Galvannealing.....                         | 6            |
| 2.1.3.1 Iron-Zinc intermetallic phases.....                      | 7            |
| 2.1.3.2 Mechanical properties of intermetallic Fe-Zn-phases..... | 9            |
| 2.1.4 Press hardening.....                                       | 11           |
| 2.1.4.1 Indirect press hardening .....                           | 11           |
| 2.1.4.2 Direct press hardening.....                              | 12           |
| 2.1.4.3 Liquid metal embrittlement .....                         | 14           |
| 2.2 Finite element method .....                                  | 17           |
| 2.2.1 Submodelling .....   | 18           |
| 2.2.2 Cracks in ABAQUS.....                                      | 19           |
| 2.2.2.1 Static cracks .....                                      | 19           |
| 2.2.2.2 Surface-based crack propagation analysis .....           | 20           |
| 2.2.2.3 Extended finite element method .....                     | 24           |
| 2.2.2.4 Cohesive model .....                                     | 26           |
| 2.2.3 Multipoint constraint.....                                 | 36           |
| <b>3 Crack growth simulation</b> .....                           | <b>37</b>    |
| 3.1 Preliminary Work .....                                       | 37           |

|          |  |           |
|----------|--|-----------|
| 3.2      | Three point bending test models .....                    | 38        |
| 3.2.1    | Model dimensions and boundary conditions .....           | 39        |
| 3.2.2    | Meshing .....  | 40        |
| 3.2.3    | Model differences .....                                  | 41        |
| 3.2.4    | Material properties .....                                | 43        |
| 3.2.5    | Traction-separation laws .....                           | 45        |
| 3.3      | Press-hardening model.....                               | 47        |
| <b>4</b> | <b>Results and discussion.....</b>                       | <b>50</b> |
| 4.1      | Analysis of the three point bending test simulation..... | 50        |
| 4.1.1    | 510 °C three point bending test.....                     | 51        |
| 4.1.2    | 660 °C three point bending test.....                     | 53        |
| 4.1.3    | Summary of the three point bending test simulation ..... | 56        |
| 4.2      | Press-hardening crack growth simulation .....            | 57        |
| 4.2.1    | Submodel boundary condition vs. tool interaction.....    | 58        |
| 4.2.2    | Comparison of crack positions for 510 °C.....            | 62        |
| <b>5</b> | <b>Conclusion .....</b>                                  | <b>64</b> |
| <b>6</b> | <b>Literature .....</b>                                  | <b>66</b> |

# List of Figures

|  |    |
|--|----|
| Figure 2-1: Overview of mechanical properties for different steel grades. [8] .....  | 2  |
| Figure 2-2: Hot-rolled strip production layout depending on casting technology. [11] .....   | 5  |
| Figure 2-3: Cold rolling mill with heat treatment furnace. [12].....   | 5  |
| Figure 2-4: Layout of a continuous hot-dip galvanizing line. [11].....   | 6  |
| Figure 2-5: Iron-Zinc phase diagram with 850 °C isotherm. [17] .....   | 7  |
| Figure 2-6: (a) Schematic cross-section of a galvanized strip. (b) Zn-rich side of the Fe-Zn phase diagram. [18].....  | 8  |
| Figure 2-7: (a) Microhardness in [HV] [13] and (b) fracture toughness in [MPa m <sup>0.5</sup> ] [22] of the intermetallic phases present in the Zn-layer. [13]..... | 9  |
| Figure 2-8: Flow curve for various intermetallic phases and DP980 steel. [23].....   | 10 |
| Figure 2-9: Indirect press-hardening process with forming, heating and quenching. [5] ....   | 12 |
| Figure 2-10: Direct press-hardening process with heating and combined forming and quenching. [5].....  | 12 |
| Figure 2-11: Schematic illustration of tensile strength and corresponding elongation of the respective microstructures in different press hardening steps. [1].....  | 13 |
| Figure 2-12: Schematic illustration of LME during press hardening including phase transformation at the grain boundaries. [28] .....                                 | 15 |
| Figure 2-13: Combination of factors leading to LME and possible remedies within press hardening. [3] .....   | 16 |
| Figure 2-14: Press-hardening process windows for Zn and AlSi coatings. [3] .....   | 16 |
| Figure 2-15: Geometrical and seam cracks in ABAQUS. [33] .....   | 19 |
| Figure 2-16: Crack tip, crack front and contour integral. [33].....  | 20 |
| Figure 2-17: Important distances for the critical stress criterion. [33].....  | 21 |
| Figure 2-18: Critical crack tip opening displacement criterion. [33].....  | 22 |
| Figure 2-19: Crack length versus time criterion. [33].....   | 23 |
| Figure 2-20: Mode I fracture in VCCT. [33] .....   | 24 |



|   |    |
|---|----|
| Figure 2-21: The phantom node method with real domain $\Omega_0$ and phantom domain $\Omega_p$ for both crack surfaces. [33] .....  | 26 |
| Figure 2-22: Fracture process description by the cohesive zone model showing a) the idealization of fracture by cohesive elements, b) their implementation as interface elements with the respective fracture modes and c) cohesive laws for brittle and ductile fracture. [39] | 27 |
| Figure 2-23: 2D and 3D cohesive elements with nodes and integration points. [39].....   | 28 |
| Figure 2-24: General bilinear traction-separation law with damage description and unloading behaviour. [36] .....   | 30 |
| Figure 2-25: Exponential damage evolution law. [33].....  | 32 |
| Figure 2-26: Mixed-mode fracture response based on the quadratic nominal stress and BK criteria. [33] .....   | 33 |
| Figure 2-27: Trapezoidal TSL for cohesive behaviour. [52].....  | 34 |
| Figure 2-28: Determination of maximum traction $T_0$ and cohesive energy $\Gamma_0$ parameters for normal and slant fracture. [39] .....  | 35 |
| Figure 2-29: Multipoint constraint SLIDER forcing the nodes $p^i$ to remain on a straight line between node a and b. [33] .....   | 36 |
| Figure 3-1: Original model consisting of a blank clamped between die and holder, a punch and a connector. [69].....   | 38 |
| Figure 3-2: Three point bending test model with dimensions. ....  | 39 |
| Figure 3-3: Blank mesh with increasing magnification starting from a) original thickness with coarsest elements and interactions to c) showing the smallest elements, intermetallic layer and symmetry point. ....  | 40 |
| Figure 3-4: Implementation of a crack using a) slave contact relative to the master surface in the surface interaction approach and b) a geometrically modelled crack with cohesive seam in the element based approach.....   | 42 |
| Figure 3-5: Recreation of intermetallic Zn-phase plastic properties at room temperature according to He et al. [23].....  | 43 |
| Figure 3-6: Temperature dependence of gamma-phase flow curve. The graph at 20 °C is according to He et al. [23].....  | 44 |
| Figure 3-7: Trapezoidal traction-separation law with temperature dependent parameters.  | 46 |

Figure 3-8: Triangular traction-separation law with the same temperature dependent parameters as the trapezoidal TSL.....47

Figure 3-9: Simulation of the press-hardening process by means of analytical rigid tools and submodel technique. The distance  $x$  marks the position of the crack, located in the middle of the submodel. Variations of  $x$  address different positions of the original blank. ....48

Figure 3-10: Magnification of the crack area a) showing the through cracked layer and region of SLIDER MPC in the whole submodel b) with regions of cohesive interaction and tie constraint. The left and right boundary of the submodel in b) exhibit a displacement-based submodel boundary condition, whereas the top and bottom surfaces are constraint by either force-based submodel BC or interactions with the tools for the respective models. ....49

Figure 4-1: Comparison of undeformed and deformed state of the 510 °C three point bending test, showing the von-Mises stress in GPa.....50

Figure 4-2: Crack area of the 510 °C three point bending test a) for both the triangular and trapezoidal TSL cohesive contact and b) for trapezoidal TSL cohesive elements. In both pictures the von-Mises stress is plotted in GPa. ....51

Figure 4-3: Force-displacement relation for different TSL forms and implementations of the cohesive law in the 510 °C three point bending test. The whole curve indicating a stiffness difference is shown in a), whereas b) gives a close-up view on the top of the curve, thus better displaying the stepping of the curve for the cohesive element seam.....52

Figure 4-4: Three point bending model using the triangular TSL and cohesive contact at 660 °C. For the point of job abortion at 211 ms, a stress plot in GPa of a) the bending zone and b) a close-up image of the crack are displayed.....53

Figure 4-5: Three point bending test at 660 °C using the cohesive contact formulation with trapezoidal TSL. A von-Mises stress plot in GPa at 209 ms is shown in a) the bending zone and b) a magnification image of the crack area. ....54

Figure 4-6: Cohesive element seam three point bending test model at 660 °C using a trapezoidal TSL. The plots show the stresses in GPa of a) the bending area and b) the crack area at a time of 172 ms, when the simulation is aborted. ....55

Figure 4-7: Force-displacement relation for different TSL forms and implementations of the cohesive law in the 660 °C three point bending test. The point of rapid crack growth and also the one where the crack for Contact Trapezoidal runs into the tie constraint are clearly visibly. ....56

Figure 4-8: Von-Mises stress plot in GPa showing the boundary influence of a too small model and the “hooking” of the deformable tools mesh with the free crack surface. ....57

Figure 4-9: Cohesive contact submodel at  $x=102,5$  mm during the press-hardening process with tool contact. The plot shows the von-Mises stress in GPa of a) the whole submodel with tools and b) the crack area at the point of job abortion at 656 ms. ....58

Figure 4-10: Press-hardening submodel at  $x=102,5$  mm without tool contact. The model exhibiting cohesive contact is shown in the final position at 805 ms. Both a) the whole submodel and b) the crack area show the von-Mises stress plot in GPa. ....59

Figure 4-11: The press-hardening process with tool interaction for a submodel at  $x=102,5$  mm with cohesive contact. The von-Mises stress in GPa of a) the whole submodel with tools and b) the magnification of the crack area is plotted for the point of job abortion at 651 ms. 59

Figure 4-12: Submodel with force-based submodel boundary condition on the upper and lower surface for press-hardening simulation. From initial position  $x=102,5$  mm a) the potential cracking area and b) the full submodel are displayed. The von-Mises stress plot in GPa is taken at 611 ms, the point in time when calculation is abandoned. ....60

Figure 4-13: Slave surface damage variable CSDMG for tool interaction and submodel boundary condition approach at different temperatures. Damage is plotted against the true distance from the submodel top surface alongside the predefined crack path. ....61

Figure 4-14: For the simulation without tool contact at  $510\text{ }^{\circ}\text{C}$  a) the matching end positions of the crack for different  $x$ -values in the original framework and b) the corresponding damage variable plot alongside the crack path are displayed.....62

Figure 4-15: Magnifications of the crack region for different  $x$ -values. The von-Mises plot in GPa for position a) is shown at the state of job abortion at 708 ms, whereas b) and c) both display the crack at the final time of 805 ms. ....63

# List of Tables

Table 1: Alloy composition of 22MnB5 in wt.-% based on Taylor & Clough [1]..... 3

Table 2: Yield Strength and Young's Modulus reported for Fe-Zn intermetallic phases.....10

# Used symbols

|  |  |
|--|--|
| $20\text{MnB8}_{\text{onset}}(20\text{ }^{\circ}\text{C})$ | stress for plasticity onset of 20MnB8 at 20 °C                                 |
| $20\text{MnB8}_{\text{onset}}(T)$                          | stress for plasticity onset of 20MnB8 at temperature T                         |
| $20\text{MnB8}(\varphi, T)$                                | evolution of stress for 20MnB8 with increasing true strain at temperature T    |
| $a$  | crack length   |
| $a$  | node a   |
| $\mathbf{a}_i$   | nodal enriched degree of freedom vector for the jump function                  |
| $b$  | width of an element  |
| $b$  | node b   |
| $\mathbf{b}_i^{\alpha}$                                    | nodal enriched degree of freedom vector for the asymptotic crack tip functions |
| $D$  | damage variable  |
| $d$  | length of an element   |
| $E$  | Young's modulus  |
| $E(T)$   | Young's modulus at temperature T   |
| $E_3$  | transverse Young's modulus   |
| $F_{\alpha}(x)$  | asymptotic crack tip functions   |
| $F_{v,2,5}$  | vertical force between nodes 2 and 5   |
| $f$  | fracture criterion   |
| $G(T)$   | shear modulus at temperature T   |
| $G^c$  | fracture energy  |
| $G_I$  | mode I energy release rate   |
| $G_{IC}$   | critical mode I energy release rate  |
| $G_{\text{equiv}}$   | equivalent energy release rate   |

|                     |   |
|---------------------|---|
| $G_{\text{equivC}}$ | critical equivalent energy release rate                     |
| $G_n$               | fracture energy in normal direction                         |
| $G_n^C$             | critical fracture energy in normal direction                |
| $G_s$               | $G_s+G_t$   |
| $G_s$               | fracture energy in 1 <sup>st</sup> shear direction          |
| $G_s^C$             | critical fracture energy in 1 <sup>st</sup> shear direction |
| $G_T$               | $G_n+G_s+G_t$   |
| $G_t$               | fracture energy in 2 <sup>nd</sup> shear direction          |
| $G_t^C$             | critical fracture energy in 2 <sup>nd</sup> shear direction |
| $H(x)$              | jump function   |
| $h$                 | distance between top and bottom layer                       |
| $K$                 | interface stiffness matrix                                  |
| $K_{nn}$            | mode I penalty stiffness                                    |
| $K_{ss}$            | mode II penalty stiffness                                   |
| $K_{tt}$            | mode III penalty stiffness                                  |
| $L$                 | liquid zinc   |
| $l$                 | length from crack length vs. time diagram                   |
| $l_1$               | initial crack length  |
| $l_3$               | distance from crack tip node 3 to the reference point       |
| $N$                 | number of nodes in an element                               |
| $N_i(x)$            | nodal shape functions                                       |
| $\mathbf{n}$        | normal vector to the crack plane                            |
| $p$                 | number of mesh transitions                                  |
| $p^i$               | nodes to remain on a straight line                          |
| $\mathbf{q}$        | virtual crack extension direction vector                    |
| $\mathbf{T}$        | vector of cohesive stresses                                 |
| $T(\delta)$         | cohesive traction   |
| $T_n^0$             | maximum normal traction                                     |

|   |  |
|---|--|
| $t$   | thickness of adjacent sub-laminate   |
| $\mathbf{t}$                                      | tangent vector to the crack front  |
| $\overline{t_{\text{eff}}}$                       | effective traction   |
| $t_n$   | normal traction  |
| $t_n^0$   | maximum normal traction  |
| $t_n^0$   | maximum normal stress  |
| $t_s$   | traction in 1 <sup>st</sup> shear direction  |
| $t_s^0$   | maximum nominal stress in 1 <sup>st</sup> shear direction                            |
| $t_t$   | traction in 2 <sup>nd</sup> shear direction  |
| $t_t^0$   | maximum nominal stress in 2 <sup>nd</sup> shear direction                            |
| $\mathbf{u}$                                      | displacement vector  |
| $\mathbf{u}_i$                                    | nodal displacement vectors   |
| $v_{1,6}$   | vertical displacement of nodes 1 and 6   |
| $x$   | element edge length  |
| $\alpha$  | pre-factor for penalty stiffness   |
| $\alpha$  | parameter for power law  |
| $\alpha(\text{Fe})$                               | ferrite  |
| $\Gamma$  | $\Gamma$ -zinc phase   |
| $\Gamma_0$  | cohesive energy  |
| $\Gamma_1$  | $\Gamma_1$ -zinc   |
| $\Gamma_{\text{onset}}(20\text{ }^\circ\text{C})$ | stress for plasticity onset of $\Gamma$ -phase at 20 °C                              |
| $\Gamma_{\text{onset}}(T)$                        | stress for plasticity onset of $\Gamma$ -phase at temperature T                      |
| $\Gamma(\varphi, T)$                              | evolution of stress for $\Gamma$ -phase with increasing true strain at temperature T |
| $\gamma_{\text{sl}}$                              | surface energy   |
| $\Delta l$  | nodal distance on the slave surface  |
| $\Delta l_{23}$                                   | nodal distance on the slave surface from node 2 to node 3                            |

|                        |   |
|------------------------|---|
| $\delta$               | $\delta$ -zinc phase                                      |
| $\delta$               | crack opening displacement                                |
| $\delta$               | (current) separation                                      |
| $\delta$               | displacement vector                                       |
| $\delta_0$             | separation at damage onset                                |
| $\delta_{1k}$          | compact $\delta$ -zinc                                    |
| $\delta_{1p}$          | palisade $\delta$ -zinc                                   |
| $\delta^f$             | critical separation                                       |
| $\delta_c$             | critical crack opening displacement                       |
| $\delta_f$             | separation at failure                                     |
| $\delta_{f1}$          | separation at decline of traction                         |
| $\delta_m$             | effective displacement                                    |
| $\delta_m^0$           | effective displacement at damage onset                    |
| $\delta_m^f$           | effective displacement at failure                         |
| $\delta_m^{\max}$      | maximum effective displacement                            |
| $\delta_n$             | normal separation   |
| $\delta_n^f$           | critical normal separation                                |
| $\delta_s$             | separation in 1 <sup>st</sup> shear direction             |
| $\delta_t$             | separation in 2 <sup>nd</sup> shear direction             |
| $\varepsilon_{\max}$   | principal strain  |
| $\varepsilon_{\max}^0$ | maximum principal strain                                  |
| $\varepsilon_n$        | nominal normal strain                                     |
| $\varepsilon_n^0$      | maximum nominal normal strain                             |
| $\varepsilon_s$        | nominal strain in 1 <sup>st</sup> shear direction         |
| $\varepsilon_s^0$      | maximum nominal strain in 1 <sup>st</sup> shear direction |
| $\varepsilon_t$        | nominal strain in 2 <sup>nd</sup> shear direction         |
| $\varepsilon_t^0$      | maximum nominal strain in 2 <sup>nd</sup> shear direction |



|                   |   |
|-------------------|---|
| $\zeta$           | $\zeta$ -zinc phase   |
| $\eta$            | $\eta$ -zinc phase  |
| $\eta$            | parameter for BK law  |
| $\nu(T)$          | Poisson's ratio at temperature T  |
| $\sigma^f$        | normal failure stress   |
| $\sigma_c$        | critical cleavage stress  |
| $\sigma_{\max}$   | principal stress  |
| $\sigma_{\max}^0$ | maximum principal stress  |
| $\hat{\sigma}_n$  | current normal stress at requested distance                             |
| $\sigma_y$        | yield stress  |
| $\tau_1$          | current stress in 1 <sup>st</sup> shear direction at requested distance |
| $\tau_2$          | current stress in 2 <sup>nd</sup> shear direction at requested distance |
| $\tau_1^f$        | failure stress in 1 <sup>st</sup> shear direction                       |
| $\tau_2^f$        | failure stress in 2 <sup>nd</sup> shear direction                       |

# Acronyms

|                |   |
|----------------|---|
| A <sub>3</sub> | austenite to ferrite transformation temperature |
| BC             | boundary condition                              |
| bcc            | body centered cubic                             |
| BiW            | Body in White                                   |
| BK             | Benzeggagh-Kenane                               |
| COH2D4         | four-noded 2D cohesive element                  |
| CP             | complex phase                                   |
| CPE4           | four-noded quadratic plain strain element       |
| CSDMG          | damage variable                                 |
| CT             | compact-tension                                 |
| CZM            | cohesive zone model                             |
| dof            | degree of freedom                               |
| DP             | dual phase                                      |
| fcc            | face centered cubi                              |
| FEM            | finite element method                           |
| GA             | galvannealed                                    |
| GI             | galvanized                                      |
| hcp            | hexagonal closest packed                        |
| HETVAL         | internal heat generation subroutine             |
| HSLA           | high-strength low-alloy                         |
| HV             | vickers hardness                                |
| L              | liquid  |
| LEFM           | linear elastic fracture mechanic                |
| LM(I)E         | liquid metal (induced) embrittlement            |
| MAXE           | Maximum nominal strain criterion                |

|                  |   |
|------------------|---|
| MAXPE            | Maximum principal strain criterion                          |
| MAXPS            | Maximum principal stress criterion                          |
| MAXS             | Maximum nominal stress criterion                            |
| $M_f$            | martensite finish temperature                               |
| MPC              | multipoint constraint                                       |
| $M_s$            | martensite start temperature                                |
| P                | perlite   |
| PH               | press hardening   |
| PHS              | press-hardened steels                                       |
| ppm              | parts per million   |
| QUADE            | Quadratic nominal strain criterion                          |
| QUADS            | Quadratic nominal stress criterion                          |
| SDVINI           | initial solution-dependent state variable fields subroutine |
| TSL              | reaction-separation law, traction-separation law            |
| UEXPAN           | thermal expansion subroutine                                |
| USDFLD           | user defined field subroutine                               |
| VCCT             | Virtual Crack Closure Techniqu                              |
| XFEM             | extended finite element method                              |
| $\alpha'$        | martensite  |
| $\alpha$ -Fe(Zn) | zinc-saturated ferrite                                      |
| $\Gamma$         | Fe <sub>3</sub> Zn <sub>10</sub>                            |
| $\Gamma_1$       | Fe <sub>11</sub> Zn <sub>40</sub>                           |
| $\delta_{1k}$    | FeZn <sub>7</sub>   |
| $\delta_{1p}$    | Fe <sub>13</sub> Zn <sub>126</sub>                          |
| $\zeta$          | FeZn <sub>13</sub>  |
| $\Omega_0$       | real domain   |
| $\Omega_p$       | phantom domain  |

# 1 Introduction

Although materials such as aluminum and magnesium are rising in popularity, the car body is still mostly made up of steel parts. Advanced steel grades and production technologies allow for growing strength and are therefore viable for light-weight constructions while still maintaining good crashworthiness. The classical production process for most car parts uses strip material made of high-strength low-alloy (HSLA) or dual phase (DP) steel for the subsequent cold stamping. However, the strength in cold stamped components is limited due to rising deformation forces and springback. [1–4]

Boron alloyed steels manufactured by press hardening (PH) can achieve significantly higher strength while preserving good formability. Further details will be given in a later section, but in summary press hardening is achieved by forming in the hot condition and subsequently quenching in the same tool. The latest inventions aim to use already galvanized steel strips for the press hardening process to reduce equipment cost and production time. A problem in the use of zinc-coated strips for direct press hardening is that the zinc layer, which will be dealt with in detail later, is prone to cracking and liquid metal embrittlement. [1; 3; 5]

The aim of this master thesis is therefore to study and implement feasible crack initiation and propagation models on top of an already existing 2D finite element simulation of a press hardening process and subsequently compare different areas of the given part regarding their cracking potential. This is done by using the submodelling technique of the finite element software ABAQUS 2017, which will later allow to position the submodel in any area of interest and using it even to study other parts made of the same material.

# 2 Theoretical background

This section aims to introduce all the theoretical information which is necessary for the understanding of this work. Following the production route for structural parts in the automotive industry, the steel grade, the rolling and galvanizing process and the final stamping are covered. Later on, more detail is given regarding the techniques within the finite element framework used to model the crack initiation and propagation.

## 2.1 Production process for press hardened car parts

In the Body in White (BiW) of modern cars a variety of steel grades is used. Generally, they can be divided into cold-stamped steels, such as high-strength low-alloy (HSLA), dual phase (DP) and complex phase (CP) and hot-stamped or press-hardened steels (PHS). [6] Since they have been patented in 1974 by the Swedish company Norrbottens Järnverk AB for the use in agricultural products, PHS also appeared in the automotive industry in the 1980s. [1; 3] Nowadays, up to 60 % of the BiW are made of press hardening steels due to higher strengths of about 1500 MPa compared to other steels. As this tensile strength comes from a hardening step after the forming process, also the springback during forming is reduced, which is usually a limiting factor in cold-stamped steels. Figure 2-1 illustrates this by showing the common mechanical properties for different steel grades with the typical PHS 22MnB5 in both the delivery and hardened condition. [1; 3; 4; 7; 8]

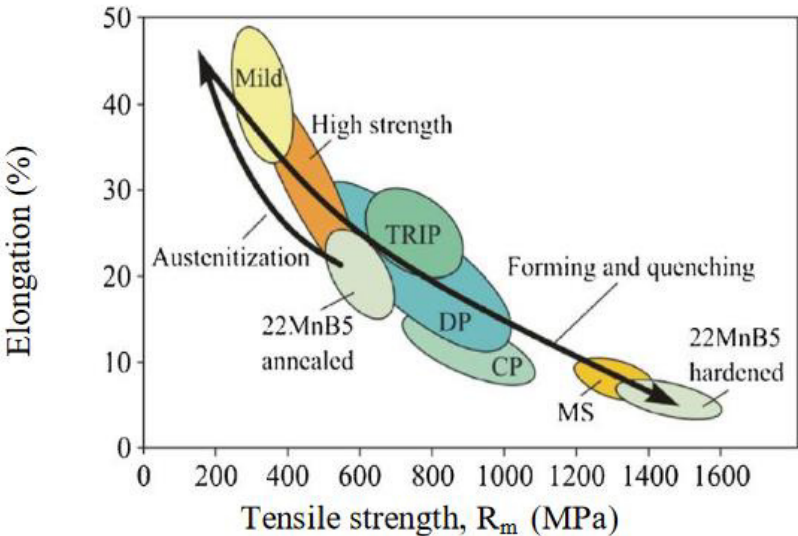


Figure 2-1: Overview of mechanical properties for different steel grades. [8]

### 2.1.1 Alloy composition of press hardening steels

One of the most commonly used PHS alloys is 22MnB5. [1; 3; 8; 9] Variations in the content of the most important alloying elements carbon, manganese and boron can be used together with a limited amount of other elements to adjust the processing and final product properties on a certain scale. Steel grades like 8MnCrB3, 20MnB5, 27MnCrB5, 37MnB4 [8; 9] and 20MnB8 [5] are some other examples mentioned in literature. Based on a table made by Taylor & Clough [1] who summed up the composition of 22MnB5 given by different steel manufacturers, Table 1 shows the largest range in content of the major elements in weight-percent.

Table 1: Alloy composition of 22MnB5 in wt.-% based on Taylor & Clough [1].

| Alloy  | C         | Mn        | Si        | Cr        | Ti    | B           |
|--------|-----------|-----------|-----------|-----------|-------|-------------|
| 22MnB5 | 0,20-0,28 | 0,90-1,40 | 0,15-0,40 | 0,10-0,50 | <0,05 | 0,001-0,005 |

Carbon as an element is necessary for the desired martensitic transformation. It is therefore responsible for hardenability and determines solely the tensile strength of the final part. Additionally, carbon has a solid solution strengthening effect. [1; 3; 9]

Manganese and chromium both enhance the strength through solid solution and lower the critical cooling rate, thus leading to a better hardenability. However, manganese is not as detrimental to ductility as carbon and chromium. Therefore the latter may not be necessary in the usually thin strips used in the automotive industry. [1; 3; 9]

Whereas silicon provides solid solution strengthening and hardenability, its main purpose is as a deoxidizing agent during steelmaking. In fact, silicon should be even limited to values as low as possible because it promotes detrimental silicon oxide formation on the surface. [1; 3]

Although the boron content is only in the range of ten to fifty parts per million (ppm), it is a crucial element for PHS. As solute boron segregates to the austenite grain boundaries it increases the grain boundary energy and thus delays ferrite nucleation on austenite grain boundaries. This, in turn, lowers the critical cooling rate and promotes martensite formation. However, as boron segregates heavily, too large amounts of boron will lead to the supersaturation of the austenite grain boundaries and subsequent formation of  $M_{23}(C,B)_6$  borocarbide, thereby reducing the hardenability. [1; 3; 10]

In order to keep boron in solid solution and prevent the reaction of boron with residual nitrogen, small amounts of titanium are added. As titanium has a higher affinity to nitrogen than boron, titanium nitride will form rather than boron nitride. Due to its rather coarse nature, this titanium nitride will, unlike to other steel grades, not provide any recrystallization retardation, grain refinement or precipitation strengthening whatsoever. However, excess titanium leads to the precipitation of fine titanium carbides, which cause, in contrast to titanium nitride, recrystallization retardation, grain size refinement and precipitation strengthening. Titanium carbide is therefore detrimental, as it increases the tensile strength of the annealed product, reduces the process window for hot rolling and continuous annealing and depletes the matrix of carbon, thus leading to a lower strength in the final product. [1]

### **2.1.2 Hot and cold rolling**

The molten steel is mostly cast into slabs of up to 250 mm thickness via the continuous casting process. [11] It is therefore inevitable to reduce the thickness in order to produce strip metal for automotive applications. As a first step, hot rolling is performed with temperatures generally above  $A_3$  and thus in the austenitic phase. The most general process layout consists of a reheating furnace, a roughing stand, a finishing stand and a coiler. Depending on the casting technology, as it can be seen in Figure 2-2, one or more of these components may be unnecessary. [11; 12]

In setups using a furnace, it is either responsible for reheating the material from room temperature or keeping it hot after the casting for the direct input to the rolling process. Thick slabs will firstly need a roughing mill to reduce the slab thickness to about 60 mm. Before entering the finishing mill, a shear cuts off the head and tail ends to give them both a clean edge. Depending on the material thickness, the slab will pass up to seven horizontal tandem mills, where its thickness gets gradually reduced to 1,2 mm at lowest. In this process, the material is greatly elongated and at the end forms a strip which may pass an additional runout or cooling table before entering the coiling facility. High-pressure water nozzles are used on various locations in between the rolling mills to remove scale and prevent it from being pressed into the surface. [11; 12]

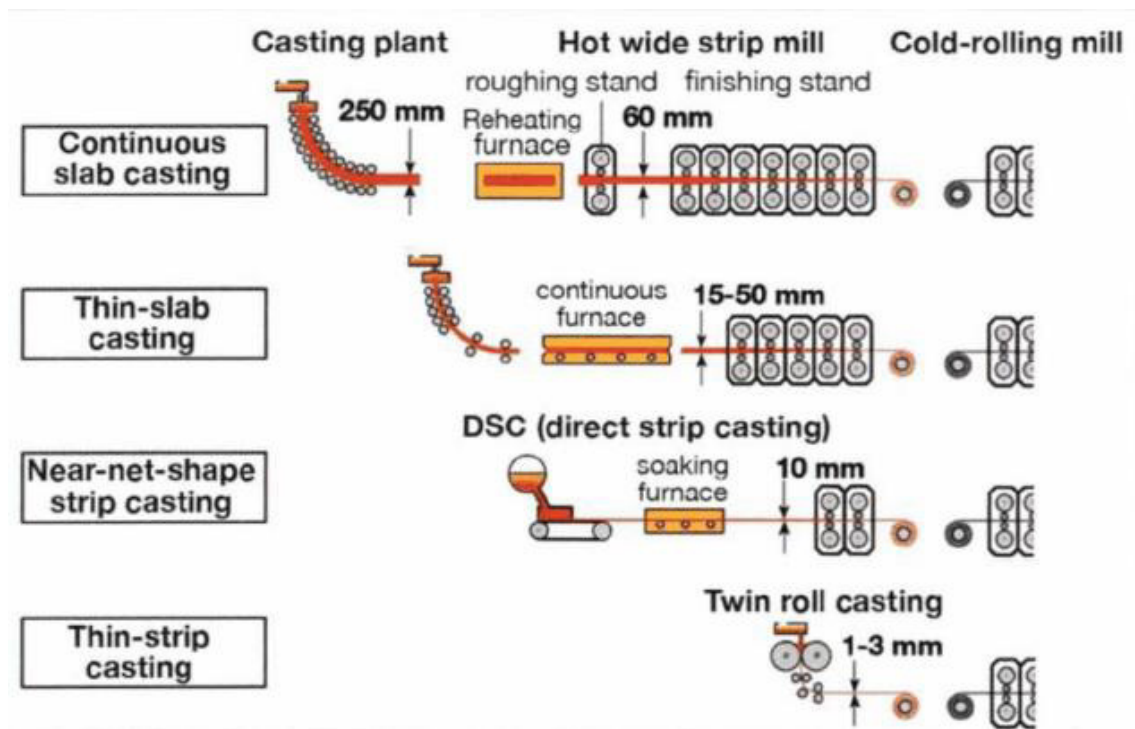


Figure 2-2: Hot-rolled strip production layout depending on casting technology. [11]

After the hot rolling process the coil is transported to the cold rolling mill. In order to achieve a high surface quality, the decoiled strip firstly enters a pickling facility where scale from the hot rolling process is removed with the aid of sulphuric or hydrochloric acid. As the final gauge cannot be reached within one reduction step, multiple passes of the cold rolling mill are traversed until the desired thickness between 0,4 and 1,8 mm is reached. [12] To reduce the heavy cold deformation and retrieve the steel's formability, the strip passes through an annealing furnace. Also a range of different heat treatments could be conducted in this step. Levelling, straightening and skin-pass rolling are conducted at the end and the strip is cut to its final length after coiling. [11; 12]

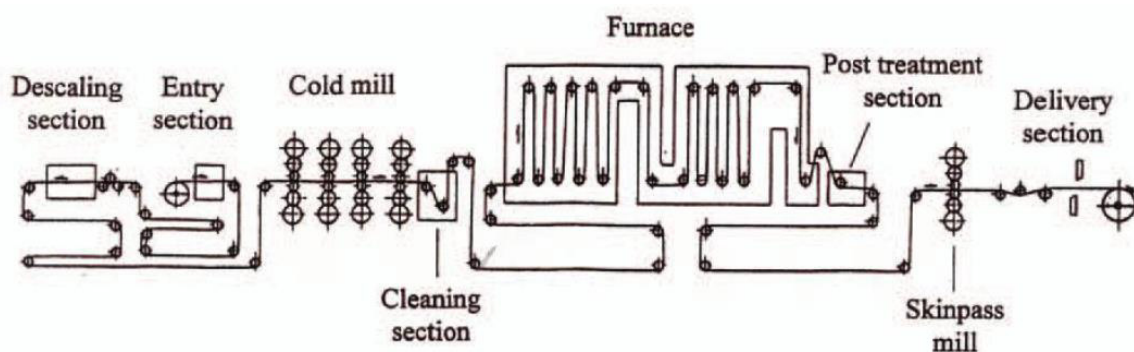


Figure 2-3: Cold rolling mill with heat treatment furnace. [12]



### 2.1.3 Galvanizing and Galvannealing

Demands in the automotive industry regarding corrosion protection require an additional galvanizing process (GI). In the fully continuous galvanizing line, the cold rolled coil is firstly decoiled and welded together with the preceding strip. For the coating itself, either electrolytic or hot-dip galvanizing is possible. Since the latter process is more common, only hot-dip galvanizing is discussed more thoroughly, with the process layout displayed in Figure 2-4. [13] In the hot-dip galvanizing process the strip firstly passes a preheating furnace where the surface is cleaned from oxides using a  $N_2/H_2$  atmosphere and temperatures from 500 to 760 °C. Depending on the steel alloy, the strip is also annealed above the recrystallization temperature, which is typically around 700 °C. Before entering the zinc bath with temperatures around 450 °C, the strip is cooled down after the furnace in order to not affect the zinc bath temperature. Upon leaving the zinc, the surface layer thickness is controlled via air pressure nozzles. A cooling section, followed by levelling, stretching and chromating succeeds the galvanizing process. The last part is again the coiling and cutting of the now galvanized strip. [1; 11; 12; 14]

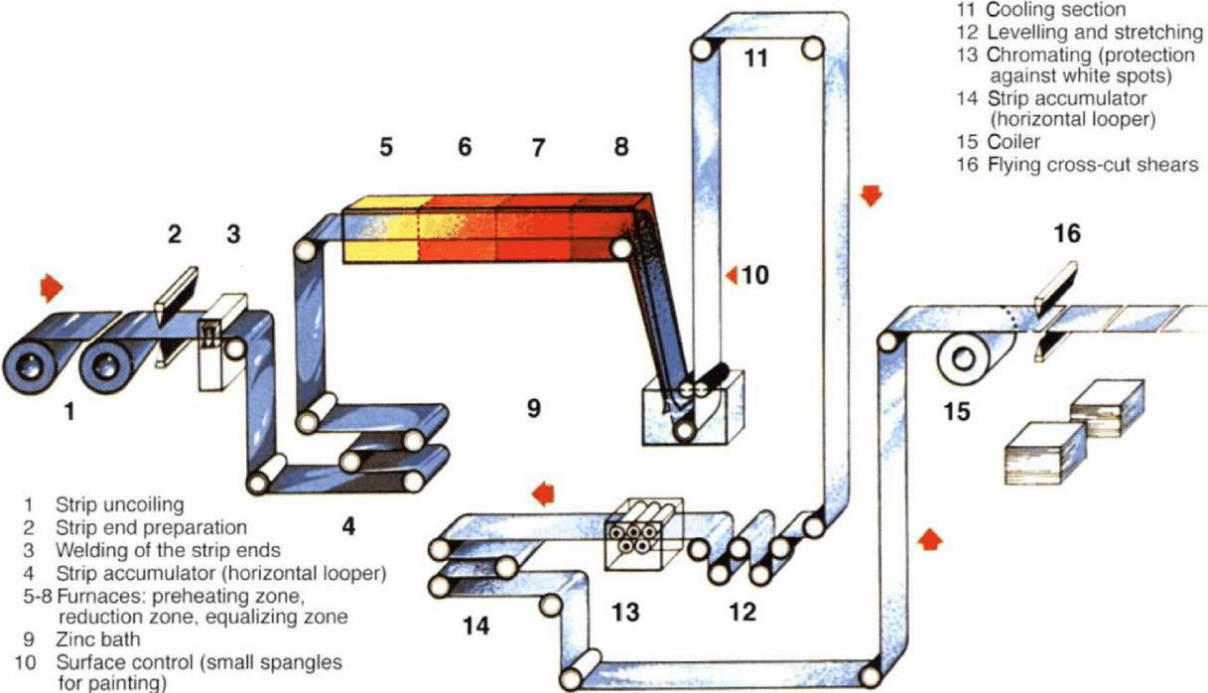


Figure 2-4: Layout of a continuous hot-dip galvanizing line. [11]

As zinc melts at 419,45 °C and boils at 906 °C, it is sought to further stabilize the coating. [5; 15] In a process called galvannealing (GA), the coated strip is annealed at temperatures above the melting point of zinc, usually between 450 and 470 °C. [11; 16] Thereby the zinc layer is consumed and forms several intermetallic phases within the iron-zinc system through diffusion. Figure 2-5 shows the whole iron-zinc phase diagram with an isothermal line at 850 °C, which is a typical lower boundary for temperatures in the press hardening process. [1; 14; 17]

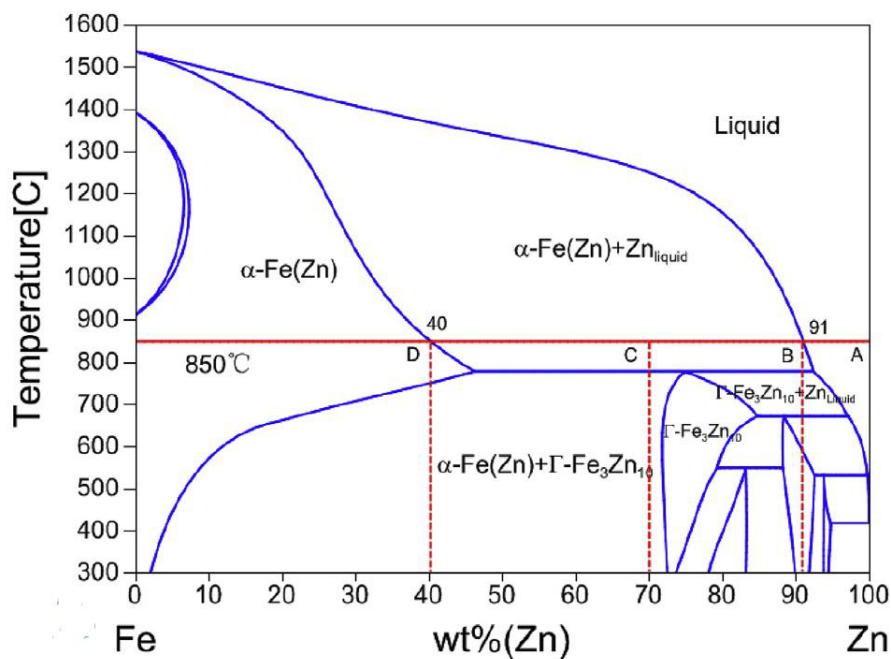


Figure 2-5: Iron-Zinc phase diagram with 850 °C isotherm. [17]

### 2.1.3.1 Iron-Zinc intermetallic phases

The five intermetallic phases present in the coating layer of GA steels are  $\Gamma$  (Fe<sub>3</sub>Zn<sub>10</sub>),  $\Gamma_1$  (Fe<sub>11</sub>Zn<sub>40</sub>),  $\delta_{1k}$  (FeZn<sub>7</sub>),  $\delta_{1p}$  (Fe<sub>13</sub>Zn<sub>126</sub>) and  $\zeta$  (FeZn<sub>13</sub>), in ascending order regarding their zinc content. [13; 15; 16; 18] A schematic cross-section of this layer is displayed in Figure 2-6 (a), showing the aforementioned phases and their respective stability area in the Zn-rich side of the iron-zinc diagram in Figure 2-6 (b). [18] It should be noted that the exact stability areas and stoichiometrical formulas are somewhat different in literature, as Inui et al. [13] have shown by collecting data from other references [15; 18; 19] and displaying it together with their own findings.

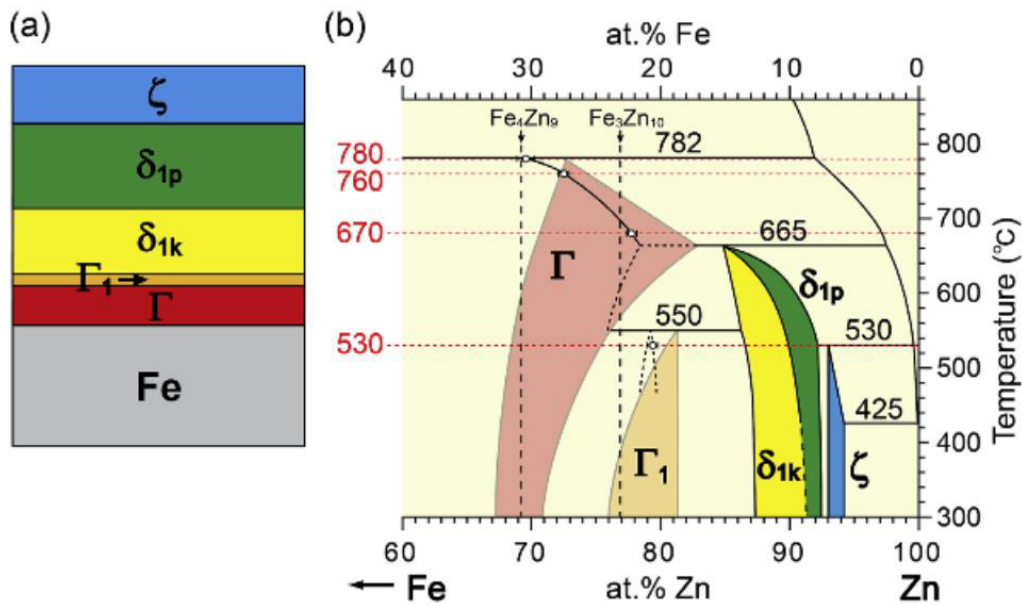


Figure 2-6: (a) Schematic cross-section of a galvanized strip. (b) Zn-rich side of the Fe-Zn phase diagram. [18]

On top of the  $\zeta$ -phase shown in Figure 2-6 (a) might be a remainder of almost pure Zn called  $\eta$ -phase, which has not been consumed during the diffusion process. In fact, it is a substitutional solid solution crystal with about 0,03 weight-% iron in the hexagonal (hcp) solidified zinc. [14; 16]

The formation of the  $\zeta$ -phase ( $\zeta$ ) is due to the peritectic reaction (1) between the  $\delta$ -phase ( $\delta$ ) and liquid zinc (L) at a temperature of 530 °C. Alternatively, the  $\zeta$ -phase could also form between the solid  $\eta$ -zinc ( $\eta$ ) and  $\delta$ , as described in formula (2). Regardless of the reaction,  $\zeta$ -FeZn<sub>13</sub> contains 5 – 6,2 weight-% Fe in a base centered monoclinic crystal. [13; 14; 16]



For the  $\delta$ -phase, sometimes two slightly different structures,  $\delta_{1p}$  (palisade morphology) and  $\delta_{1k}$  (compact morphology) are reported, with iron contents from 7 to 11,5 wt.-%. Their respective structures are referred to as FeZn<sub>7</sub> for  $\delta_{1k}$  on the Fe-rich side and Fe<sub>13</sub>Zn<sub>126</sub>, sometimes also FeZn<sub>10</sub>, for  $\delta_{1p}$  on the Zn-rich side. However, both phases exhibit the same hexagonal crystal structure and are formed by the same peritectic reaction (3) between the  $\Gamma$ -phase ( $\Gamma$ ) and liquid zinc (L) at 665 °C. Although studies have proven the existence of two different phases, as the only difference is the palisade like structure of  $\delta_{1p}$  in contrast to the more compact one from  $\delta_{1k}$ , it is under debate whether or not to distinguish two different  $\delta$ -types. [13; 14; 16]



In contrast to the aforementioned phases, the  $\Gamma_1$ -phase is the product of the peritectoid reaction (4) at 550 °C between  $\Gamma$  and  $\delta$ , which themselves are intermetallic phases. As the iron content in the face centered cubic (fcc) crystal varies between 17 and 19,5 wt.-%, so do the chemical formulas describing the phase. Whereas the stoichiometrical expression for the  $\Gamma_1$ -phase is referred to as  $\text{Fe}_5\text{Zn}_{21}$  [14] or  $\text{FeZn}_4$  [20] by some authors, the most recent studies used  $\text{Fe}_{11}\text{Zn}_{40}$  [18; 21] and  $\text{Fe}_{21,2}\text{Zn}_{80,8}$  [13] as chemical formulas. Following these formulations, the crystal structure is more precisely described as  $\gamma'$ -brass structure, a substructure of the common fcc, with the details still under debate. [13; 13; 14; 16; 18]



At last, the  $\Gamma$ -phase possesses the highest iron contents with 23,5 – 28 wt.-%. It crystallizes at a temperature of 782 °C in the  $\gamma$ -brass structure, a substructure of the body centered cubic (bcc) system, due to the peritectic reaction of  $\alpha$ -iron ( $\alpha(\text{Fe})$ ) and liquid zinc (5). Stoichiometrical expression vary between  $\text{Fe}_3\text{Zn}_{10}$  [14],  $\text{Fe}_4\text{Zn}_9$  [13] and  $\text{FeZn}_3$ . [16]



### 2.1.3.2 Mechanical properties of intermetallic Fe-Zn-phases

Some studies have been conducted to determine the mechanical properties of the intermetallic compounds found in the Zn-layer. The ultimate goal of these studies is to determine the best coating composition for a good formability in subsequent steps. Although the values vary a bit depending on literature,  $\Gamma_1$  has reportedly the highest microhardness [13; 14] and  $\delta_{1p}$  the highest fracture toughness [13; 22] of all. This is also displayed in Figure 2-7, with (a) on the left showing the hardness in HV and (b) on the right expressing the fracture toughness in  $\text{MPa}\cdot\text{m}^{0,5}$  for the different phases. [13]

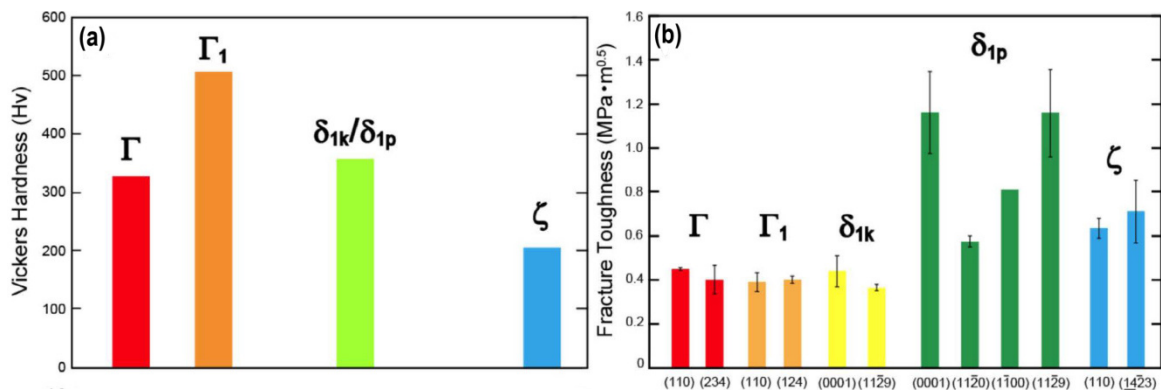


Figure 2-7: (a) Microhardness in [HV] [13] and (b) fracture toughness in [ $\text{MPa}\cdot\text{m}^{0,5}$ ] [22] of the intermetallic phases present in the Zn-layer. [13]

In contrast to that, Okamoto et al. [21] found that both  $\Gamma$  and  $\zeta$  exhibit a small amount of plastic deformation before fracture and are therefore more ductile than  $\Gamma_1$ ,  $\delta_{1k}$  and  $\delta_{1p}$ , which show no plastic deformation at all. As values vary also in this case, Table 2 below gives the reported magnitudes of yield strength and Young's modulus for all intermetallic compounds according to their respective authors. [22; 23]

Table 2: Yield Strength and Young's Modulus reported for Fe-Zn intermetallic phases.

| Phase                 | $\eta$ | $\zeta$ | $\delta$      |               | $\Gamma$   |          | Author |
|-----------------------|--------|---------|---------------|---------------|------------|----------|--------|
|                       |        |         | $\delta_{1p}$ | $\delta_{1k}$ | $\Gamma_1$ | $\Gamma$ |        |
| Yield Strength [MPa]  | -      | 120     | 1090          | 1280          | 1270       | 540      | [22]   |
| Young's Modulus [GPa] | -      | 82,4    | 110           | -             | 118        | 151      | [22]   |
|                       | 83     | 128     | 141           |               | 210        |          | [23]   |

Also, flow curves at room temperature have been determined by He et al. [23] for Eta ( $\eta$ ), Zeta ( $\zeta$ ), Delta ( $\delta$ ), Gamma ( $\Gamma$ ) and a substrate of DP980 steel. Just as in Table 2 above, also for the flow curves in Figure 2-8 no further distinctions were made between the two  $\delta$ - and  $\Gamma$ -phases from this author.

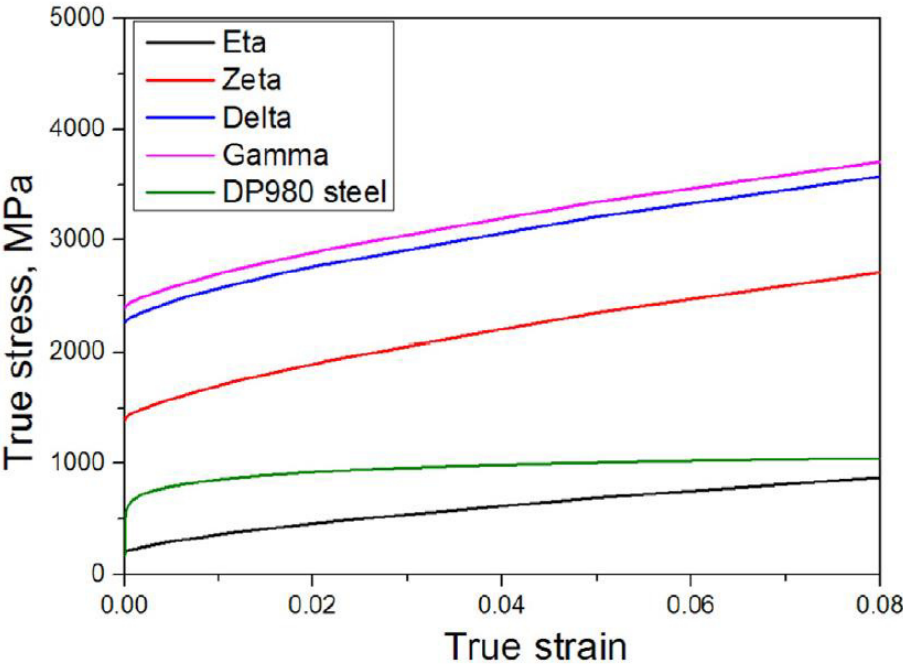


Figure 2-8: Flow curve for various intermetallic phases and DP980 steel. [23]

## 2.1.4 Press hardening

Even though the press hardening process itself can be further sub-divided into indirect and direct press hardening, both have the quenching of the austenitised material in a water cooled forming tool in common. Together with a suitable material, as described in section 2.1.1, a hard martensitic microstructure can be achieved. Depending on the heating and quenching facilities, the microstructure and thus the properties can be tailored to different sections of the same part. [1; 3; 5; 9; 17; 24]

### 2.1.4.1 Indirect press hardening

The indirect process, pictured in Figure 2-9, is basically a traditional cold forming process with an additional hardening step. Firstly, the strip with ferritic-perlitic microstructure is cut into blanks of the desired dimensions and is then deformed in the cold stage. This brings also the usual drawbacks of cold forming, like issues with springback, unwanted work-hardening, larger forming forces and generally lower formability. For the stamping process, the blank is put in between a punch and a die, both together resembling the final parts geometry. As a ram presses the punch on the die, the blank is deformed in less than two seconds to match its desired geometry to more than 95 %, depending on the adjustment later done in the hot-stamping. [1; 4; 9]

The pre-formed part is then heated in a roller hearth furnace to about 900 – 950 °C, which is well above the typical  $A_3$  temperature of 22MnB5, lying between 800 and 830 °C. Usually inert gases like nitrogen, hydrogen or argon are used as furnace atmosphere in order to prevent the oxidation and decarburization of the steel, especially if it is uncoated. After soaking for three to eight minutes, which assures homogeneous austenitisation and can also be used to promote the alloying process between the coating and the steel substrate, the pre-formed part is transferred to the hot-stamping press in less than ten seconds. This is especially crucial as to prevent the premature ferrite formation, as well as oxidation and decarburization. During the transfer, the part may lose 100 – 200 °C in temperature, contingent upon parameters like initial temperature, surface area and thickness. [1; 3; 9; 17; 25]

With about 800 – 850 °C, depending on furnace temperature and cooling during transfer, the pre-formed part is put into the hot-stamping or press hardening tool, also consisting of ram, punch and die like the cold press. As the press closes and adjusts the part geometry to the final form, the material cools down to approximately 600 – 650 °C due to contact with the cold forming tool, while still maintaining a metastable austenitic microstructure. When the

press is fully closed, the actual quenching takes place and the steel is cooled down at an average rate of 30 °C/s to below 200 °C via heat conduction to the internally water cooled punch and die. With the pressure maintained for eight to twelve seconds, this step assures rapidly passing the area between martensite start ( $M_s$ ) and martensite finish ( $M_f$ ), which is typically between 410 °C ( $M_s$ ) and 230 °C ( $M_f$ ) for 22MnB5, and exceeding the critical cooling rate of 25 °C/s. The now usually fully martensitic part is ejected from the press and air cooled to ambient temperature. It exhibits a yield strength of 1000 to 1250 MPa and a tensile strength of 1400 – 1700 MPa with a corresponding total elongation of 4 – 8 % (see Figure 2-11, step 3). [1; 3; 5; 7–9]

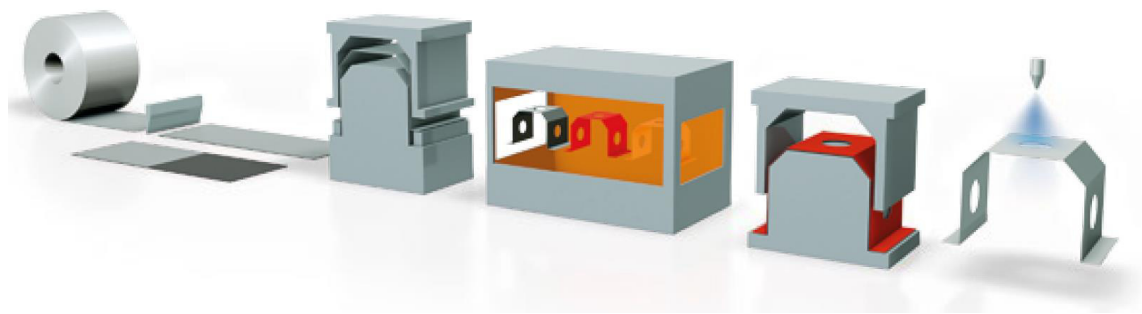


Figure 2-9: Indirect press-hardening process with forming, heating and quenching. [5]

#### 2.1.4.2 Direct press hardening

In contrast to the indirect process, the steel blanks are heated before the first forming in the direct press hardening process (see Figure 2-10). As a consequence, smaller furnaces can be used for heating. Other than that the heating and transfer procedure follows the same steps and parameters as in the indirect process. However, the major difference is the forming in the austenitised condition. The hot and austenitic material has a much lower strength, resulting in lower forming forces, and a greatly enlarged total elongation compared to the ferritic-perlitic as delivered condition, as it can also be seen in Figure 2-11. Combining these effects, a much larger formability of the material is given as compared to the cold state, which in turn allows for more design freedom and parts of higher complexity. [1; 4; 8]

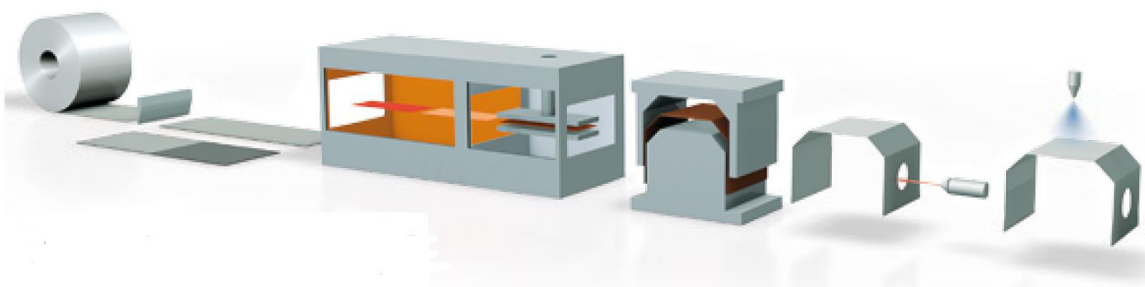


Figure 2-10: Direct press-hardening process with heating and combined forming and quenching. [5]



The schematic representation of strength and elongation of the ferritic-perlitic, austenitic and martensitic microstructures in Figure 2-11 is valid for both the indirect and the direct press hardening, the only difference being the forming step taking place after austenitisation in the direct process. As mentioned earlier, the final microstructure can be altered from ferritic-perlitic over bainitic to fully martensitic and intermediate types in between, depending on heating and quenching parameters. [1; 3; 5; 24]

A possibility to enhance the total elongation of the final part is the so called quenching and partitioning process, in which the initial quenching is conducted to a temperature between  $M_s$  and  $M_f$ . In a subsequent step, the carbon diffuses by holding at lower temperatures from the martensite to the retained austenite in order to stabilize it. The resulting martensitic-austenitic duplex microstructure has better elongation and fracture properties than the fully martensitic one. [7; 26]

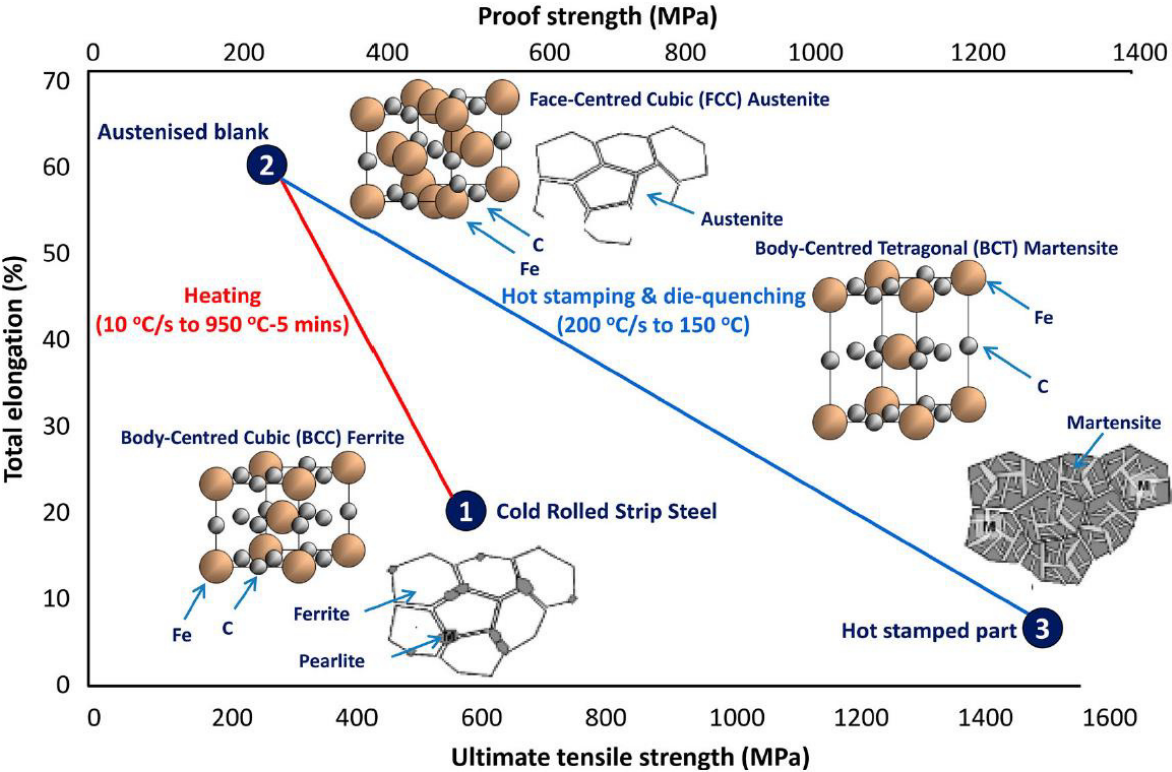


Figure 2-11: Schematic illustration of tensile strength and corresponding elongation of the respective microstructures in different press hardening steps. [1]



### 2.1.4.3 Liquid metal embrittlement

Despite the obvious advantages of the direct press hardening process in investment costs, process time and formability, it suffers from one major drawback, namely liquid metal (induced) embrittlement (LM(I)E) as a result of the low melting point of galvanized and galvanized type surface coatings. This phenomenon is avoided by the indirect press hardening as the forming is conducted on the cold material with no occurrence of liquid metal. [1; 3; 25]

LME generally occurs whenever liquid metal penetrates into an otherwise ductile material subjected to stresses and thus a sudden loss of ductility and therefore brittle cracking occurs. Penetration of liquid metal may either occur into pre-existing cracks or alongside grain boundaries and other weak interfaces by adsorption, diffusion and dissolution. [1; 3; 17; 27–29]

Several theories and mechanisms can be differentiated regarding LME. Commonly it is believed that liquid metal is adsorbed on the grain boundaries if the reduction of surface energy through adsorption is high enough. Then the liquid metal causes a reduction of the surface energy ( $\gamma_{SL}$ ) in Griffith's brittle fracture theory (6) [29] and thereby reduces also the cohesive energy required to separate two surfaces. As this theory links the surface energy with the critical cleavage stress ( $\sigma_c$ ) of a crack with length "a" in an elastically loaded material with Young's Modulus "E", a reduction of surface energy also results in a drop in the critical debonding stress. [29]

$$\sigma_c = \sqrt{\frac{2 \cdot E \cdot \gamma_{SL}}{\pi \cdot a}} \quad (6)$$

However, this theory assumes that the embrittlement results solely from adsorption of liquid metal on the grain boundary surface. [29] For the press hardening process a different mechanism is suggested, whereby it is believed that liquid zinc (L), present through the partial melting of  $\delta$ -,  $\Gamma$ - and  $\Gamma_1$ -phases during austenitisation, penetrates pre-existing cracks in the galvanized (GA) layer and reaches the steel (Figure 2-12, I and II). As the diffusion is much larger at grain boundaries, Zn diffuses in between the austenite ( $\gamma$ ) grains. A phase transformation from austenite to  $\alpha$ -Fe(Zn) zinc-saturated ferrite ( $\alpha$ ) occurs on the Zn-enriched parts of the grain boundaries due to Zn being a ferrite stabilizer (Figure 2-12, III). With applied tensile stresses, a crack may propagate more easily at the weaker layer of  $\alpha$  on the grain boundaries (Figure 2-12, IV). As liquid zinc flows into the crack by means of the capillary effect, the process is repeated until either no stress is present or the temperature has dropped enough for the zinc to be fully solid. During quenching the iron-saturated liquid

zinc in the crack transforms into  $\Gamma$ -phase. The other phases represented in Figure 2-12 are pearlite (P) and martensite ( $\alpha'$ ). [17; 27; 28]

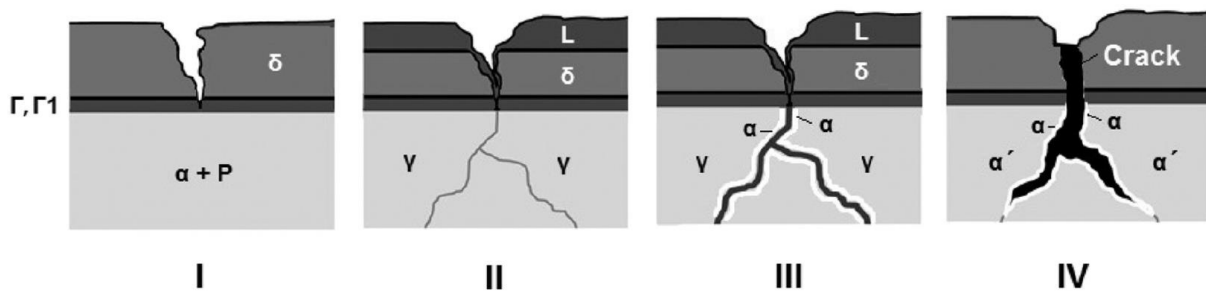


Figure 2-12: Schematic illustration of LME during press hardening including phase transformation at the grain boundaries. [28]

As mentioned above, liquid metal embrittlement occurs when a combination of high stresses, liquid metal and a susceptible base material come together. If one of these is taken away, LME could be avoided. Figure 2-13 illustrates the conditions necessary for LME as well as possible remedies within the press hardening process to influence the respective conditions. [3]

First of all, a huge amount of parameters regarding the base material influence its susceptibility to LME. Some of the most important ones are chemical composition, carbon equivalence, yield strength, hardness and residual stresses. Additionally, more complex properties like grain boundary energy are to be accounted for. Also forming within the so called “ductility trough”, located usually between 700 and 950 °C, promotes cracking and thereby additional embrittlement through liquid metal penetration. However, it is not practically possible to consider and alter all these properties in order to avoid a material prone to LME. [3; 28]

Concerning the stresses, influences of magnitude, triaxiality and strain rate have been reported. A possibility to avoid LME is to separate the stresses induced through forming from the liquid metal that occurs during austenitisation. This is done via the indirect press hardening, although it comes with the limitations and disadvantages mentioned earlier. Other methods to reduce the stress level include carefully designed die forms and a well lubricated forming. [3; 28]

Lastly, a reduction of liquid metal can also help to prevent LME. For galvanized (GI) steels this can only be achieved by limiting the coating weight and thereby its thickness. The better option, however, would be the use of galvanized (GA) coatings, as not only the melting point of zinc (419,58 °C) [15], but also the evaporation temperature (906 °C) [5; 15] could be

significantly raised by the diffusion alloying with iron. Additional influences of the liquid metal temperature and chemical composition on LME were also found. [3; 5; 28]

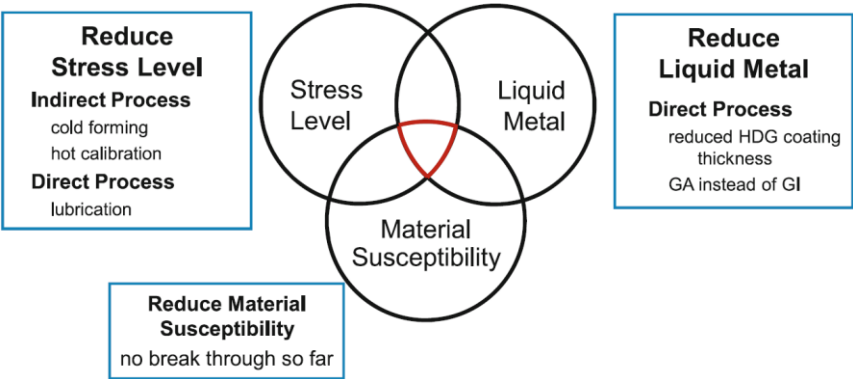


Figure 2-13: Combination of factors leading to LME and possible remedies within press hardening. [3]

Recently a new technology has been developed to mitigate or even prohibit LME during direct press hardening. This process involves a contactless pre-cooling of the steel blank with the aid of air nozzles. Since it has been found that crack formation is more likely if forming is conducted above 782 °C, the blank is cooled down to temperatures below this value but above  $M_s$ , usually between 550 and 580 °C. Thereby all zinc is solid whilst the forming still takes place with austenitic microstructure, although with a little higher forces and slightly lower formability due to the decreased temperature. The final martensitic transformation is achieved through quenching in the die. However, the PH process for Zn-coated blanks has generally a rather narrow process window regarding time and temperature. Austenitisation temperature (880 – 900 °C) [3; 5] and boiling point of zinc (906 °C) [3; 5] are the temperature boundaries while the time is limited by too little or too much diffusion, as illustrated by the blue area in Figure 2-14. [1; 3; 5]

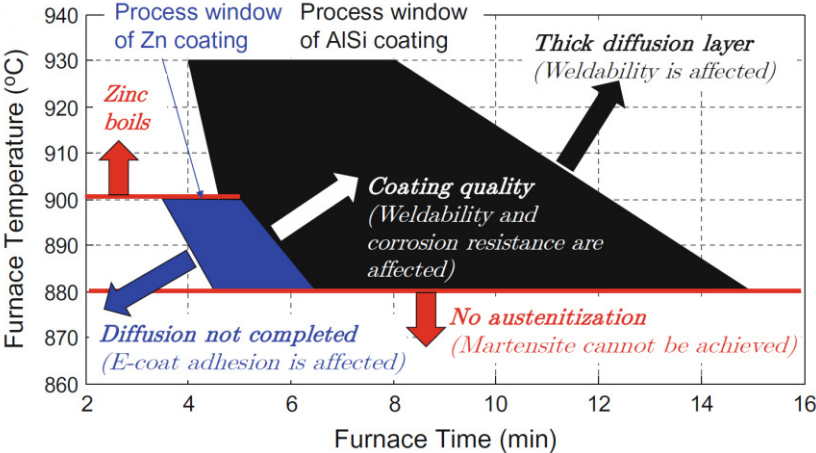


Figure 2-14: Press-hardening process windows for Zn and AlSi coatings. [3]

Also the classical 22MnB5 can only be held for approximately two seconds in the pre-cooling temperature range of 550 – 580 °C before bainite formations starts. In order to stabilize the process and widen the process window, a 20MnB8 steel with GA coating has been developed, which can be held for over 20 s at 550 °C before bainitic transformation. This steel, together with the pre-cooling technology allows for direct hot stamping while mitigating the risk of LME. [1; 3; 5]

## 2.2 Finite element method

Originating in the 1950s, the finite element method (FEM) has ever since grown more popular for the investigation of structures and micromechanical problems. Rising capacities in computer hardware allow for the investigation of problems with continuously higher complexity. [30]

Generally speaking, this method interpolates the complex differential equations of continuum mechanics, stemming from the conservation of a physical quantity, with polynomial interpolation functions valid within an element portion of the whole structure. These so called finite elements thereby result from the proper meshing of the investigated structure. An advantage of FEM compared to other numerical methods is that the meshing can be done with a great variety of different element shapes and is not bound to orthogonal and structured meshes, which allows to model intricate geometries very accurately. From the contributions of each individual element, a global stiffness matrix is generated and a system of linear equations in matrix form of the same type as in equation (7) [31] is solved by computer aided numerical algorithms. These algorithms provide an approximate solution of the initial problem, calculating forces, displacements and stresses very closely to the real ones depending on the mesh size. [30–32]

$$[Stiffness] \cdot [Displacements] = [Forces] \quad (7)$$

However, as a lot of literature on the fundamentals and mathematics behind FEM is available (for example Klein [31], Koutromanos [30] and Zienkiewicz et al. [32], only to mention a few), the following sections in this work will only focus on more in-depth techniques within the FEM-framework, which are necessary for the development of a crack propagation model.

### 2.2.1 Submodelling

The submodelling technique implemented in the ABAQUS software allows studying certain sections of a model in greater detail without huge computational costs. As the original model, called the global model for this method, can be analysed by using a rather coarse mesh, computing time can be saved. Later on, the area of interest is cut out from the global model and forms the so called submodel. Results obtained from the global model are then used to serve as boundary conditions in a subsequent, separate analysis for the submodel, which can have a more refined mesh and even a different material response. However, the global model must represent the conditions at the submodel boundary with adequate accuracy as a prerequisite for this technique. Furthermore, the different modelling of the submodel should not change the solution at its boundary significantly. [33]

As the global model and the submodel generally differ in their meshing, elements of the global model in the vicinity of the submodel boundary are used to interpolate the requested degrees of freedom (dof) to act as submodel boundary condition. These global model elements are taken from the relative position of the submodel assembly compared to the global model assembly. Defining a global model element set as source prevents elements from other nearby model parts to influence the interpolation. A tolerance specifies the distance for extrapolating global element results if a driven submodel node happens to lie outside the global model. For the global model analysis, also the result output frequency as well as the nodal output precision have to be considered. [33]

In ABAQUS, two variants of the submodelling technique are implemented, namely the node-based and the surface-based submodelling. More common is the node-based submodelling, which uses the requested dofs from the global models displacement field as boundary conditions. In contrast to that, the surface-based submodelling applies the stresses from the global model as surface tractions on the submodel. Whilst node-based submodelling has advantages if the model is exposed to large deformations or rotations, the surface-based method may provide more accurate results if the stiffness of the global model and the submodel differ significantly. If desired, both techniques can be combined and used to drive the same submodel. However, the ABAQUS user manual advises to use the node-based technique. [33]

Although not classified as a submodelling technique, the predefined fields option in ABAQUS is oftentimes used for submodels. Allowing to apply constant as well as analytical fields or reading field variables from a global model analysis, this tool can be used to transfer stress or temperature distributions obtained in the global model onto the submodel. [33]

## 2.2.2 Cracks in ABAQUS

There are many ways to study cracks with the aid of ABAQUS finite element software. In the following, a brief introduction is given on the possibilities of crack modelling and investigation with a focus on cohesive behaviour and the associated traction-separation law (TSL). Corresponding to the later simulation, the two-dimensional relations are emphasized for the sake of simplicity. However, the same principles and possibilities apply to three dimensions.

### 2.2.2.1 Static cracks

If a pre-existing crack is present within a model in ABAQUS, it is possible to study the onset of crack propagation. Originating in fracture mechanics theory, either the stress intensity factor  $K$ , J-integral or  $C_T$ -integral are used as indicators for linear-elastic, plastic and creep fracture study, respectively. For contour integral analysis, a crack must contain edges (in 2D) or faces (in 3D), that are free to separate. Either existing regions with fully modelled edges or seam cracks can be used, as indicated in Figure 2-15. A seam can be assigned to an edge (in 2D) stemming from the partitioning of a face within the Interaction module of the ABAQUS user interface. During mesh generation, overlapping node duplicates are generated in the seam, allowing the opening of the initially closed crack under tensile loading. [33]

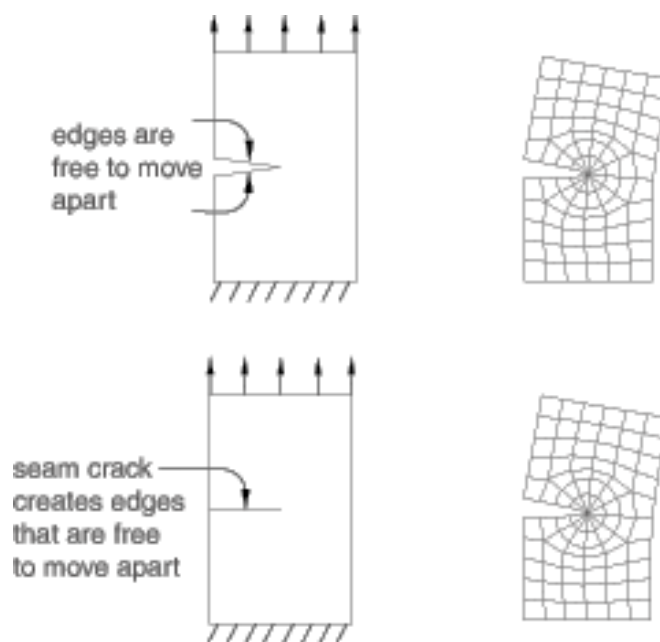


Figure 2-15: Geometrical and seam cracks in ABAQUS. [33]

In order to configure a contour integral output, the crack front, crack tip and crack extension direction have to be specified. As it is the forward part of the crack, all elements within the crack front and the first element layer around it are used for the computation of the first contour integral, as referred to in Figure 2-16. Further contour integrals add an increasing number of layers outside the crack front. Originating in the crack tip, the virtual extension direction of the crack has to be defined either by the normal to the crack plane ( $\mathbf{n}$ ) or a directly specified vector ( $\mathbf{q}$ ). In the first case, ABAQUS assumes the direction ( $\mathbf{q}$ ), according to equation (8), as orthogonal to the tangent of the crack front ( $\mathbf{t}$ ) and the normal ( $\mathbf{n}$ ). [33]

$$\mathbf{q} = \mathbf{t} \times \mathbf{n} \quad (8)$$

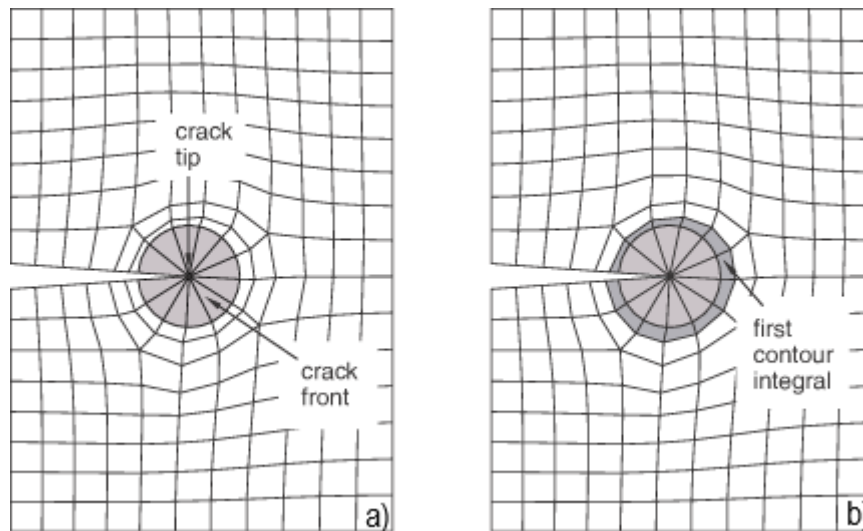


Figure 2-16: Crack tip, crack front and contour integral. [33]

Depending on the material behaviour, one of the aforementioned types of contour integrals could be requested as history output in the Step module of ABAQUS. They are furthermore computed in such a way that their value is positive if the virtual extension direction ( $\mathbf{q}$ ) is towards the material. As these cracks can only open but do not propagate, the accuracy could be improved by a meshing which properly describes the crack tip singularity. However, contour integrals could also be requested for propagating cracks with special respect to their definitions. [33]

### 2.2.2.2 Surface-based crack propagation analysis

All of the next mentioned crack analysis techniques have in common that they require partially bonded surfaces in order to locate the crack tip. Therefore a surface contact

interaction is to be set up, using any contact formulation except the finite-sliding, surface-to-surface contact. With the aid of master and slave contact formulations, possible crack surfaces are defined, thus making the crack path non-arbitrary. A node set containing slave surface nodes specifies the initially bonded parts of the surface, which will be assigned the initial conditions, whereas the unbonded part will behave as a regular contact surface. One of the following six fracture criteria can be used for crack propagation, which are critical stress at a certain distance ahead of the crack tip, critical crack opening displacement, crack length versus time, Virtual Crack Closure Technique (VCCT), enhanced VCCT and a low-cycle fatigue criterion based on the Paris-law. Except for VCCT, the use of these fracture criteria is not supported in the ABAQUS user interface and has to be manually written into the input-file with the \*FRACTURE CRITERION keyword, directly following the \*DEBOND option. Besides the Paris-law, which describes fatigue crack growth, these methods shall be shortly introduced in the following. [33]

### Critical stress criterion

When debonding is active, the critical stress criterion requires the definition of a normal failure stress ( $\sigma^f$ ) and, depending on the dimensionality of the problem, one or two shear failure stresses ( $\tau_1^f, \tau_2^f$ ). If the fracture criterion  $f$  calculated by equation (9) reaches a value of 1 at a specified distance ahead of the crack tip, the current crack tip node will debond. This distance is measured alongside the slave surface as visualized in Figure 2-17. [33]

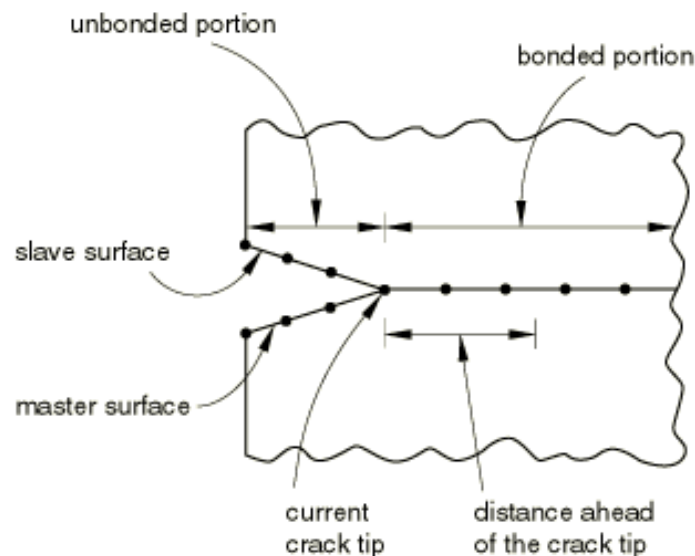


Figure 2-17: Important distances for the critical stress criterion. [33]

It is possible for the critical stresses to be dependent on temperature and other field variables. The variables  $\hat{\sigma}_n$ ,  $\tau_1$  and  $\tau_2$  represent the current stress values at the requested distance. As the crack should not propagate under pressure, only positive values for  $\hat{\sigma}_n$  are



regarded, else it is set to zero. Additionally, if the critical shear stresses are either zero or not specified at all, they are set to high numbers so that only normal stresses are taken into account. Typically this fracture criterion is most useful in describing brittle cracking materials. [33]

$$f = \sqrt{\left(\frac{\hat{\sigma}_n}{\sigma_f}\right)^2 + \left(\frac{\tau_1}{\tau_1^f}\right)^2 + \left(\frac{\tau_2}{\tau_2^f}\right)^2} \quad (9)$$

### Critical crack tip opening displacement criterion

For the critical crack tip opening displacement criterion, the current value of the crack opening displacement  $\delta$  is checked against the specified critical value  $\delta_c$  at a certain distance  $n$  behind the current crack tip. Figure 2-18 shows the crack tip opening displacement as well as the mentioned distance  $n$ . When  $\delta_c$  is reached, the fracture criterion  $f$  in equation (10) has a value of 1 and the crack propagates by debonding the current crack tip node. [33]

$$f = \frac{\delta}{\delta_c} \quad (10)$$

Regarding the data input, the crack opening displacement has to be provided as a function of the cumulative crack length, which is the difference between the initial and current crack tips, measured alongside the slave surface. As this method requires a certain crack tip deformation before debonding, it is mostly used to model crack propagation in ductile materials. Aside from that, this technique also allows crack surfaces to lie on symmetry planes. [33]

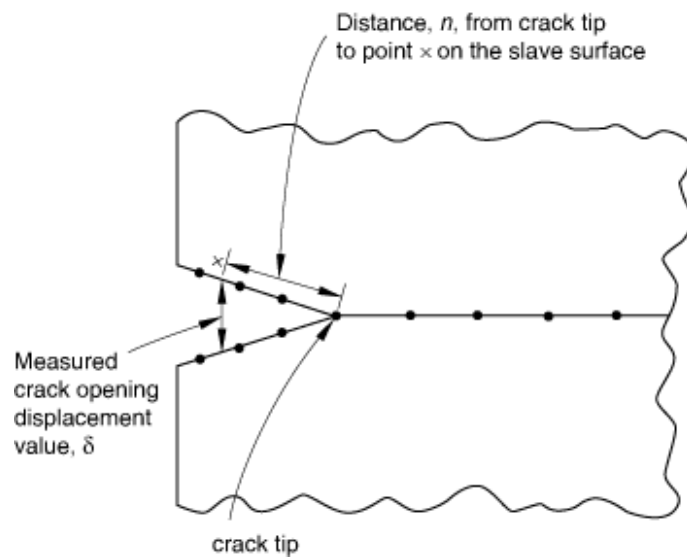


Figure 2-18: Critical crack tip opening displacement criterion. [33]

### Crack length versus time criterion

In this method, the crack length, measured from a reference point, is directly defined as a function of total time. The reference point itself is calculated from the positions of a reference node set. Concerning the fracture criterion  $f$ , equation (11) is related to Figure 2-19, as the distance of the current crack tip node to the reference point  $l_3$  is the sum of the contributions from the initial crack length  $l_1$  and the subsequent nodal distances  $\Delta l$  on the slave surface up to the current crack tip. The crack tip node will debond when the length  $l$  taken from the predefined crack length versus time diagram, as seen on the right in Figure 2-19, grows to such a value that the fracture criterion  $f$  reaches unity. [33]

$$f = \frac{l - (l_3 - \Delta l_{23})}{\Delta l_{23}} \quad (11)$$

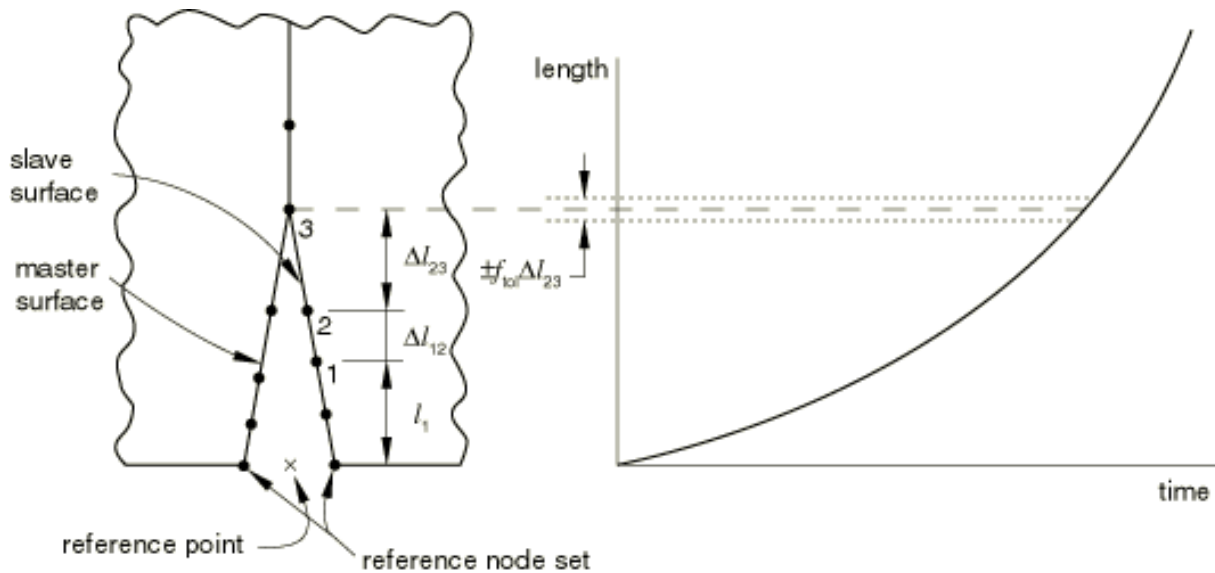


Figure 2-19: Crack length versus time criterion. [33]

### VCCT

As stated above, this fracture criterion is also supported in the ABAQUS user interface. It is based on linear elastic fracture mechanics (LEFM) theory, thus being best suited for the description of brittle crack growth. Originating in LEFM, the theory states that for brittle materials, the strain energy released by a particular crack extension is the same as the energy required to close the crack by an equal quantity. Generally, the fracture criterion in equation (12) is governed by the relation between the equivalent energy release rate  $G_{\text{equiv}}$  and the corresponding equivalent critical value  $G_{\text{equivC}}$ . The latter is calculated based on the critical energy release rates from each individual fracture mode and one of the three provided mode-mix models, which are Benzeggagh-Kenane (BK) law, power law and Reeder law. [33]

$$f = \frac{G_{equiv}}{G_{equivc}} \quad (12)$$

For the sake of simplicity, Figure 2-20 illustrates the VCCT criterion for pure Mode I loading. In this case, equation (12) can be written as follows in equation (13), whereby  $G_I$  and  $G_{IC}$  are Mode I energy release rate and the respective critical value,  $b$  describes the width and  $d$  the length of an element,  $F_{v,2,5}$  is the vertical force between nodes 2 and 5 and  $v_{1,6}$  indicates the vertical displacement of the indicated nodes. Both equation (13) and Figure 2-20 show that the energy release rate is related to the area under the load-displacement curve. [33]

$$f = \frac{G_I}{G_{IC}} = \frac{1}{2} \left( \frac{v_{1,6} F_{v,2,5}}{bd} \right) \frac{1}{G_{IC}} \quad (13)$$

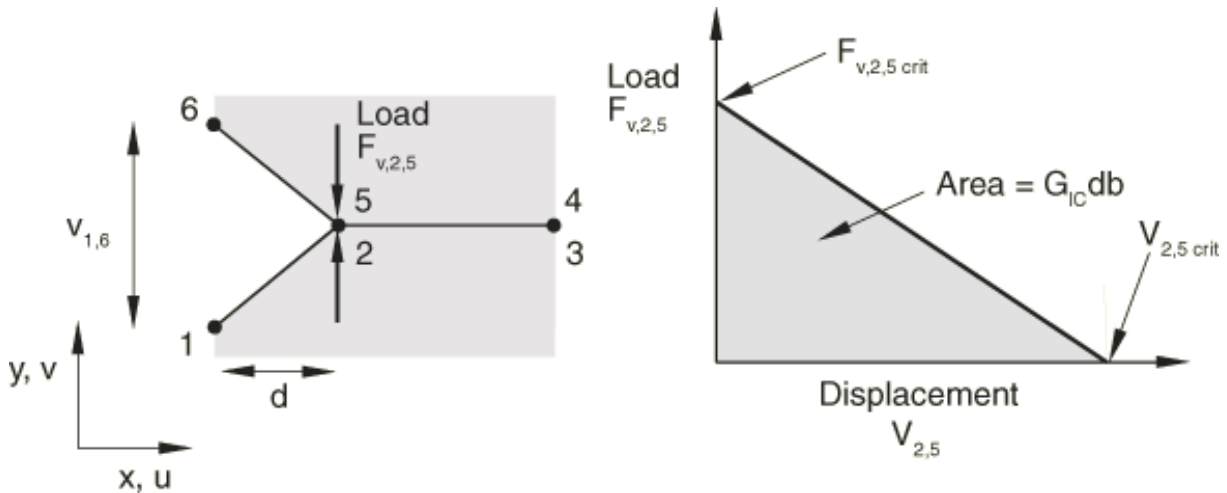


Figure 2-20: Mode I fracture in VCCT. [33]

Unlike the described VCCT criterion, the enhanced VCCT method uses two separate critical fracture energy release rates for the onset of cracking and the crack propagation. Other than that, the fundamental fracture criterion stays the same and is also described by equation (12). [33]

### 2.2.2.3 Extended finite element method

In the classical FEM-method, quantities inside elements, such as displacement, are interpolated with the aid of polynomial interpolation functions, as pointed out at the very beginning of this chapter 2.2. While this approach proves very useful for a vast amount of problems, it requires these functions to be continuous throughout the element. Thus discontinuities such as crack faces are forced to lie on the boundaries of the elements and

are therefore limited to predetermined paths. Alternatively, a constant remeshing of the model would have to be performed. First introduced in 1999 by Belytschko and Black [34], the extended finite element method (XFEM) aims to remediate this shortcoming by the introduction of special displacement functions. These displacement functions enrich the degrees of freedom in the respective element and thereby allow the presence of discontinuities. The original equation for the displacement vector  $\mathbf{u}$  in an element with  $N$  nodes only includes the nodal shape functions  $N_I(x)$  and the nodal displacement vectors  $\mathbf{u}_I$ , as the first term in equation (14) shows. For the enrichment in the XFEM method an additional jump function  $H(x)$  as well as asymptotic crack-tip functions  $F_\alpha(x)$  are introduced, both multiplied to their respective nodal enriched degree of freedom vector  $\mathbf{a}_I$  and  $\mathbf{b}_I^\alpha$ , thus forming the new displacement function (14) in an enriched element. [33–36]

$$\mathbf{u} = \sum_{I=1}^N N_I(x) \left[ \mathbf{u}_I + H(x)\mathbf{a}_I + \sum_{\alpha=1}^4 F_\alpha(x)\mathbf{b}_I^\alpha \right] \quad (14)$$

As stated before, the first part of equation (14) is valid for the classical FEM-concept and therefore for the whole model. However, the second part applies only to nodes which are cut by the crack interior, whereas the last part governs all nodes whose respective shape functions are intersected by the crack tip. With the aid of equation (14), the modelling of stationary cracks with an arbitrary crack path is possible. [33–36]

Another distinct advantage of XFEM is that it is capable of modelling not only stationary cracks, but also the processes of crack initiation and propagation. Contrary to the aforementioned surface-based methods, an initial crack might, but does not necessarily have to be present. Both the initiation and propagation behaviour of a crack can be implemented by combining the XFEM-concept with the (enhanced) VCCT method, described before in section 2.2.2.2, or the cohesive approach, which will be dealt with in the following section 2.2.2.4. While (enhanced) VCCT is best suited for brittle cracking, the cohesive approach could be also used for ductile fracture. In ABAQUS a set of elements must be defined for which it is allowed to use the enriched functions. If no pre-existing crack within this domain is assigned, then a crack initiates once a specified damage criterion according to the modelling approach is met. These damage initiation criteria will be introduced later on in section 2.2.2.4, but are related to the maximum principal stress or strain, the maximum nominal stress or strain or the quadratic nominal stress or strain. Additionally, for both VCCT and cohesive approach, a user defined damage initiation criterion can be assigned, with the difference that cohesive properties are quantified within the bulk material definition, whereas VCCT parameters are specified as interaction property. [33; 35; 36]

Concerning the crack propagation, either the direction normal to the maximum tangential stress or orthogonal to the element local 1- or 2-direction defines further crack extension. Once the direction has been determined, the crack propagation starts. This is done by dividing each element intersected by the crack into original and phantom nodes for both crack faces. In an undamaged element, the phantom nodes are tied to their respective original nodes. As soon as damage initiates, the phantom nodes can separate from their corresponding real nodes, whereas the magnitude of movement is determined by either VCCT or the cohesive law. The phantom nodes are then used for the interpolation of the displacement in the real domain  $\Omega_0$  by using the degrees of freedom provided from the original nodes and the phantom nodes in the phantom domain  $\Omega_p$ . For the correct interpolation of the resulting displacement jump, the integration is only done on the real side of each crack face up to the crack, as Figure 2-21 indicates. [33; 35; 36]

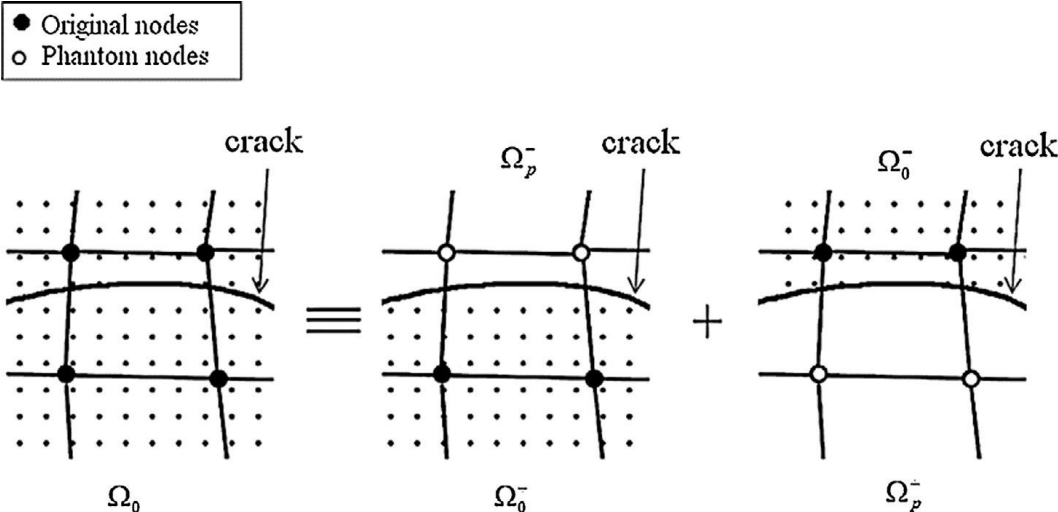


Figure 2-21: The phantom node method with real domain  $\Omega_0$  and phantom domain  $\Omega_p$  for both crack surfaces. [33]

XFEM offers some rather unique advantages like the possibility of crack initiation, arbitrary crack growth and mostly mesh independence. Brittle or ductile cracking can be modelled by the means of VCCT or a cohesive law, contour integral evaluation can be requested and XFEM can be implemented into a submodel approach. However, it is currently not able to be used alongside elastic-plastic material behaviour. [33; 35]

**2.2.2.4 Cohesive model**

Firstly introduced by Dugdale [37] and Barenblatt [38] in the early 1960s, the cohesive zone model (CZM) is a phenomenological approach to avoid the crack-tip stress singularity, which is considered unrealistic for this model. As ductile crack growth is often associated

with the nucleation and coalescence of microvoids ahead of the crack tip, as seen on top of Figure 2-22 a), other models account for the stiffness reduction due to these voids by a damaging law for the bulk material. In contrast to that, the CZM assumes the crack to have cohesive tractions  $T(\delta)$  on its ends, with the magnitude depending on the separation  $\delta$  of the crack surfaces, indicated by the idealization in Figure 2-22 a). This concept is used to separate the constitutive behaviour of the bulk elements from the damaging process by inserting cohesive interface elements between bulk elements. The damaging of the interface elements seen in Figure 2-22 b) is then governed by a cohesive law, often times also called traction-separation law (TSL). Since it is a phenomenological model, many different shapes of the TSL are in use, with Figure 2-22 c) showing two of the most common for modelling brittle and ductile fracture. However, the TSL will be dealt with in greater detail later on in this chapter. [39; 40]

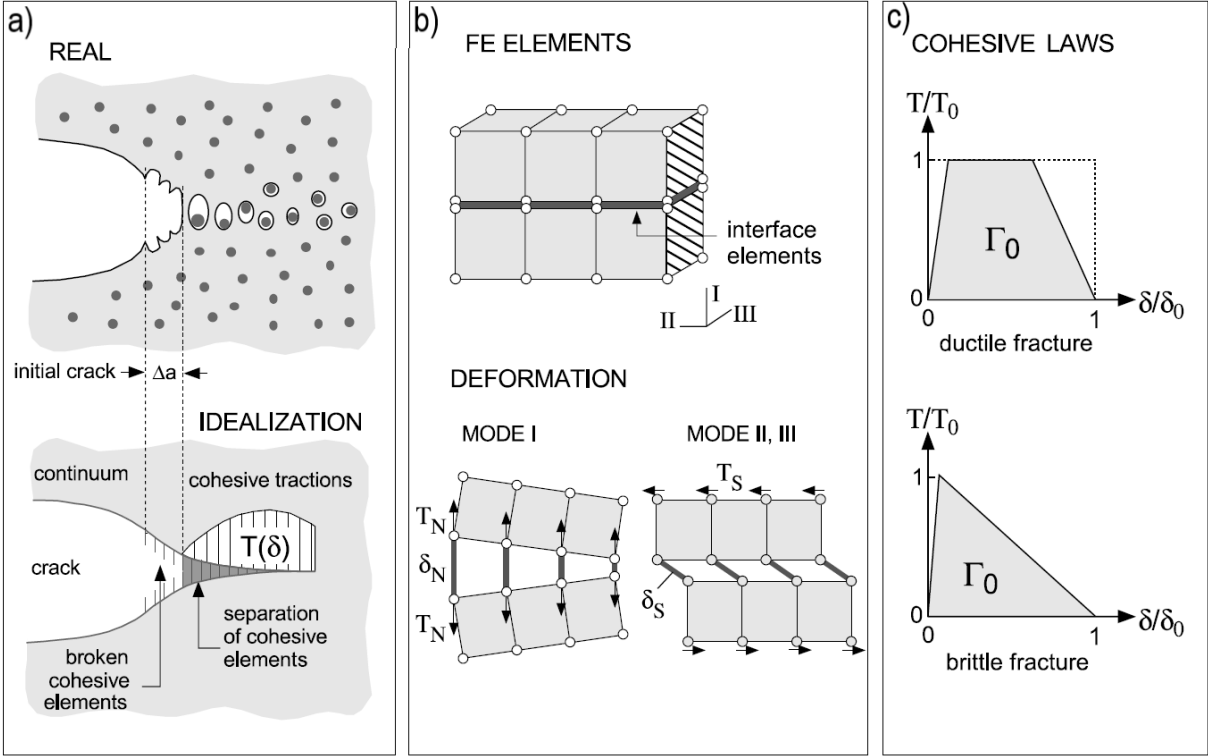


Figure 2-22: Fracture process description by the cohesive zone model showing a) the idealization of fracture by cohesive elements, b) their implementation as interface elements with the respective fracture modes and c) cohesive laws for brittle and ductile fracture. [39]

**Implementation in ABAQUS**

There are two main ways how the cohesive model can be used in ABAQUS, which are based on either cohesive elements or cohesive surface interactions. The latter is very similar in its layout to the methods described based on surface interactions in chapter 2.2.2.2,

despite the fact that cohesive interactions can be directly specified in the ABAQUS user interface. However, cohesive elements can be generated in several ways, including the creation of a separate part, element offset from an orphan mesh or insertion alongside a predefined seam. In order to properly connect the cohesive elements to the bulk material mesh, they must either share nodes or be connected via a tie constraint. Additional contact interactions can be also applied, although they are mostly not required as cohesive elements retain their compressive stiffness even if fully degraded in other directions. It is also to mention that cohesive elements are mostly modelled with a very thin, but often times finite width, which has to be considered in certain cases. Contrary to that, cohesive surfaces never account for thickness effects. Another difference is that stresses and separations are calculated on the surface nodes, which are equal to the bulk element nodes at the boundary, for cohesive surface interactions, whereas particular integration points are used in cohesive elements instead. Figure 2-24 shows cohesive elements with their nodes (numbers) and integration points (letters) for the use in 2D and 3D solid simulations, whereas the dimension of the element is always one less than the dimension of the adjacent elements. [33; 39; 41]

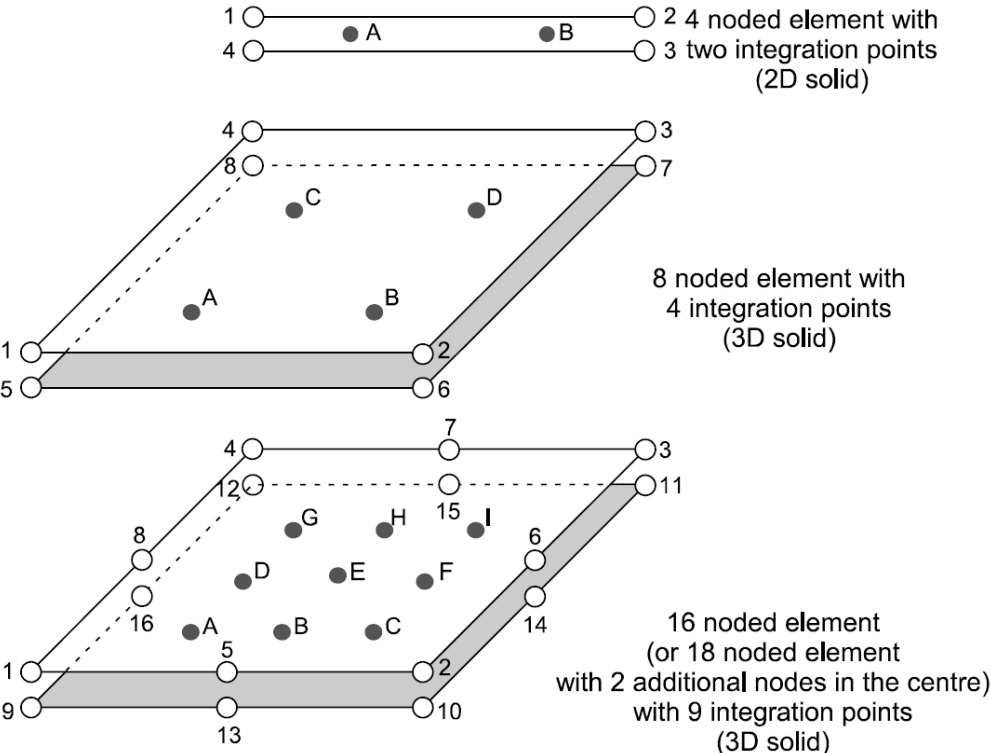


Figure 2-23: 2D and 3D cohesive elements with nodes and integration points. [39]

### Traction-separation law

For the traction-separation response, firstly a linear elastic behaviour is considered until damage initiates. Without a full coupling, for which the off-diagonal entries would be non-zero, the elastic behaviour could be described with equation (15). [33; 36; 42] In this equation, n, s and t denote the normal, shear and tear direction, respectively. The vector of the cohesive stresses  $\mathbf{T}$  contains the tractions  $t$  in the respective directions, which is also true for the displacement vector  $\delta$  and the individual separations  $\delta$ . They are connected by the interface stiffness matrix  $K$ , whose entries are to be interpreted as penalty stiffnesses. [33; 36; 42–44]

$$\mathbf{T} = \begin{Bmatrix} t_n \\ t_s \\ t_t \end{Bmatrix} = \begin{bmatrix} K_{nn} & 0 & 0 \\ 0 & K_{ss} & 0 \\ 0 & 0 & K_{tt} \end{bmatrix} \begin{Bmatrix} \delta_n \\ \delta_s \\ \delta_t \end{Bmatrix} = K \delta \quad (15)$$

To ensure that the compliance of the bulk material is much larger than that of the cohesive interface, Turon, et al. [45] suggested a mode I penalty stiffness  $K_{nn}$  according to equation (16). This equation refers to  $E_3$  as the transverse Young's modulus of the material,  $t$  as the thickness of an adjacent sub-laminate and  $\alpha$  describes a number larger than one, most commonly 50. [43; 45; 46]

$$K_{nn} \geq \alpha \frac{E_3}{t} \quad (16)$$

In order to set up a cohesive model, at least three parameters have to be provided to ABAQUS. For the simplest case of a bilinear TSL shown in Figure 2-24, these parameters are the penalty stiffness  $K_{nn}$ , the maximum traction  $t_n^0$  (also often  $T_n^0$ ) and the critical separation  $\delta_n^f$ . It is noteworthy that not only the maximum traction, but also all other variables may be different depending on literature, but these notations have been chosen to correspond to Figure 2-24. Also the cohesive energy  $\Gamma_0$ , which is equal to the J-integral, could be used as a third parameter. Since the energy dissipated by the cohesive elements is equal to the area under the TSL, the parameters traction, separation and energy are interchangeable according to equation (17). [39; 40; 47; 48]

$$\Gamma_0 = \int_0^{\delta^f} T(\delta) d\delta \quad (17)$$

Upon reaching damage initiation, the element stiffness as well as the traction is linearly reduced to zero with increasing separation. This behaviour is governed by the multiplication of the effective traction  $\bar{t}_{\text{eff}}$ , resembling the undamaged material response with stiffness  $K_{nn}$ ,



with a factor depending on a damage variable  $D$  increasing monotonically from 0 to 1. The limitation for tension only made in equation (18) is only to be regarded for mode I traction, whereas other loading cases are similar to the above statement. [33; 36; 41; 44; 46; 49]

$$t_n = \begin{cases} (1 - D)\bar{t}_{eff}, & \bar{t}_{eff} \geq 0 \\ \bar{t}_{eff}, & \text{otherwise} \end{cases} \quad (18)$$

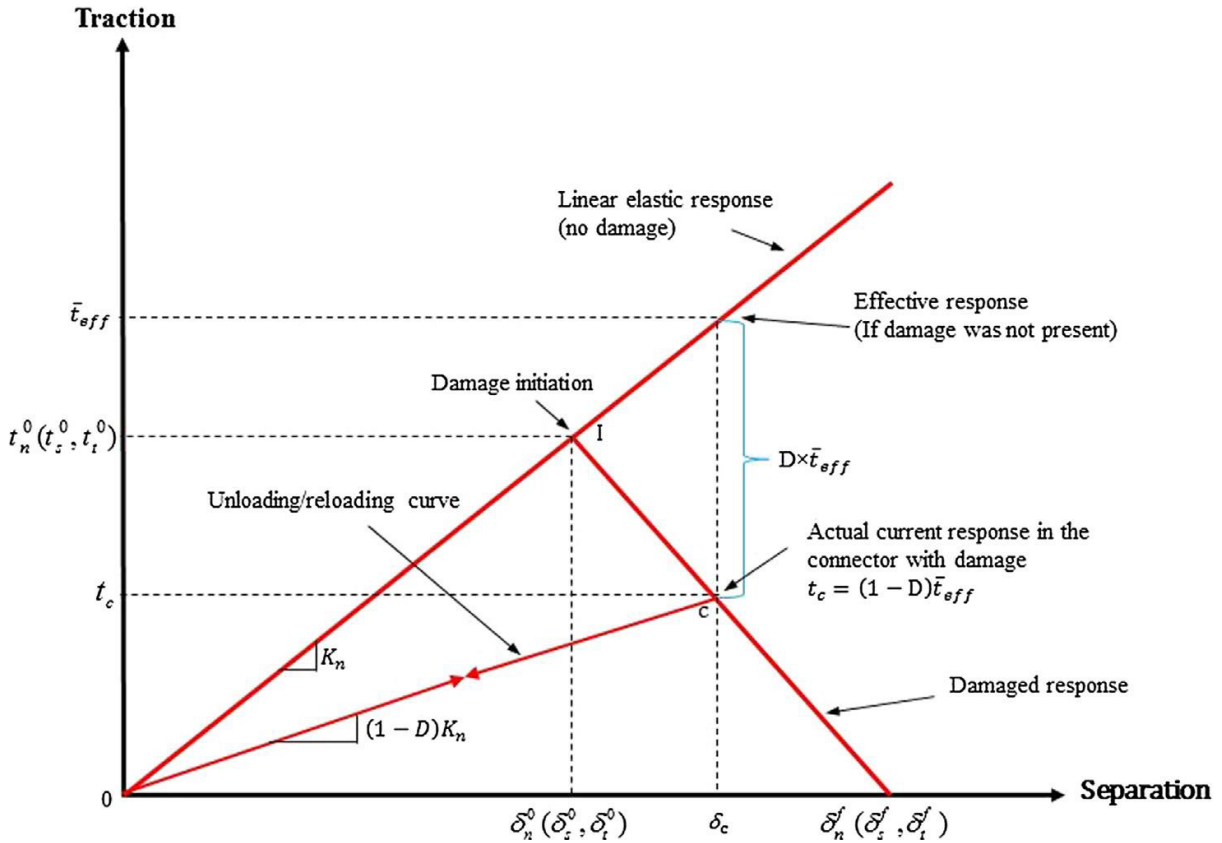


Figure 2-24: General bilinear traction-separation law with damage description and unloading behaviour. [36]

### Damage initiation

As already mentioned in section 2.2.2.3, there are six damage initiation criteria available in ABAQUS. In analogy to the damage criteria for the surface based methods described in chapter 2.2.2.2, damage initiates when the used criterion  $f$  reaches unity. In the following equations (19) to (24),  $\sigma_{max}$  and  $\varepsilon_{max}$  denote the principal stress and strain,  $t_n$ ,  $t_s$ , and  $t_t$  the nominal stress in normal, first shear and second shear direction and  $\varepsilon_n$ ,  $\varepsilon_s$  as well as  $\varepsilon_t$  the respective nominal strains in these directions. A zero in the superscript signifies the corresponding maximum allowable values and  $\diamond$  is the Macaulay bracket, indicating that compressive loading does not contribute to damage initiation. [33; 36; 41; 42; 46]

1. Maximum principal stress criterion (MAXPS)

$$f = \left\{ \frac{\sigma_{max}}{\sigma_{max}^0} \right\} \quad (19)$$

2. Maximum principal strain criterion (MAXPE)

$$f = \left\{ \frac{\varepsilon_{max}}{\varepsilon_{max}^0} \right\} \quad (20)$$

3. Maximum nominal stress criterion (MAXS)

$$f = \max \left\{ \frac{\langle t_n \rangle}{t_n^0}, \frac{t_s}{t_s^0}, \frac{t_t}{t_t^0} \right\} \quad (21)$$

4. Maximum nominal strain criterion (MAXE)

$$f = \max \left\{ \frac{\langle \varepsilon_n \rangle}{\varepsilon_n^0}, \frac{\varepsilon_s}{\varepsilon_s^0}, \frac{\varepsilon_t}{\varepsilon_t^0} \right\} \quad (22)$$

5. Quadratic nominal stress criterion (QUADS)

$$f = \left\{ \frac{\langle t_n \rangle}{t_n^0} \right\}^2 + \left\{ \frac{t_s}{t_s^0} \right\}^2 + \left\{ \frac{t_t}{t_t^0} \right\}^2 \quad (23)$$

6. Quadratic nominal strain criterion (QUADE)

$$f = \left\{ \frac{\langle \varepsilon_n \rangle}{\varepsilon_n^0} \right\}^2 + \left\{ \frac{\varepsilon_s}{\varepsilon_s^0} \right\}^2 + \left\{ \frac{\varepsilon_t}{\varepsilon_t^0} \right\}^2 \quad (24)$$

### Damage evolution

Once damage has initiated, the response for damage evolution has to be specified. ABAQUS provides two types of damage evolution laws, namely the linear damage evolution (see Figure 2-22 and Figure 2-24) and the exponential damage evolution, as seen in Figure 2-25. In both cases, either the maximum allowable separation at failure  $\delta^f$  or the fracture energy  $G^C$  may define the degradation curve. Although these values are interchangeable according to equation (17), it has to be mentioned that the fracture energy  $G^C$  as used by ABAQUS is equivalent to the area under the TSL after damage has initiated, whereas the cohesive energy  $\Gamma_0$  covers the whole area. [33]

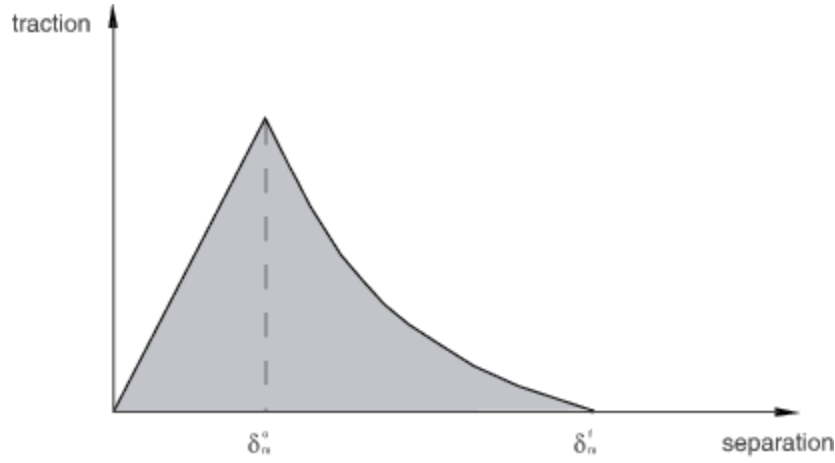


Figure 2-25: Exponential damage evolution law. [33]

Under mixed mode conditions, the damage is often defined in terms of effective displacement  $\delta_m$ , calculated according to equation (25). [33; 42; 44]

$$\delta_m = \sqrt{(\delta_n)^2 + \delta_s^2 + \delta_t^2} \quad (25)$$

The damage evolution in case of linear softening is governed by equation (26) for evolution based on displacement as well as evolution based on energy, although the effective separation at failure  $\delta_m^f$  has to be firstly calculated from the mixed mode fracture energy  $G^C$  in the latter case. In equation (26), the variable  $\delta_m^{max}$  refers to the maximum obtained effective displacement based on equation (25). [33; 42; 50]

$$D = \frac{\delta_m^f (\delta_m^{max} - \delta_m^0)}{\delta_m^{max} (\delta_m^f - \delta_m^0)} \quad (26)$$

For the evolution based on fracture energy, the mixed mode fracture energy  $G^C$  may be obtained through the power-law equation (27) or the Benzeggagh-Kenane (BK) equation (28), where the indices n, s and t designate the fracture energy in the normal, first shear and second shear direction, the superscript C indicates the respective critical values and  $\alpha$  and  $\eta$  are parameters. For the sake of a simpler writing,  $G_S = G_s + G_t$  and  $G_T = G_n + G_s + G_t$  in the following. [33; 41; 46; 50; 51]

#### 1. Power law

$$G^C = 1 / \left( \left( \frac{G_n}{G_n^C} \right)^\alpha + \left( \frac{G_s}{G_s^C} \right)^\alpha + \left( \frac{G_t}{G_t^C} \right)^\alpha \right)^{1/\alpha} \quad (27)$$

## 2. BK law

$$G^c = G_n^c + (G_s^c - G_n^c) \left\{ \frac{G_s}{G_T} \right\}^\eta \quad (28)$$

Shown below, Figure 2-26 illustrates the mixed-mode response of a bilinear TSL based on the quadratic nominal stress criterion for initiation and the BK law for the evolution of damage. The damage variable  $D$  for the exponential softening will not be shown here, as it is beyond the scope of this work. However, besides the provided softening functions, ABAQUS allows to give the damage in tabular form if a displacement based approach is used. In this case, the damage variable  $D$  has to be specified ranging from 0 to 1 as a function of  $\delta_m - \delta_m^0$ . If necessary, also dependencies on the mode mix, temperature and field variables have to be accounted for. [33]

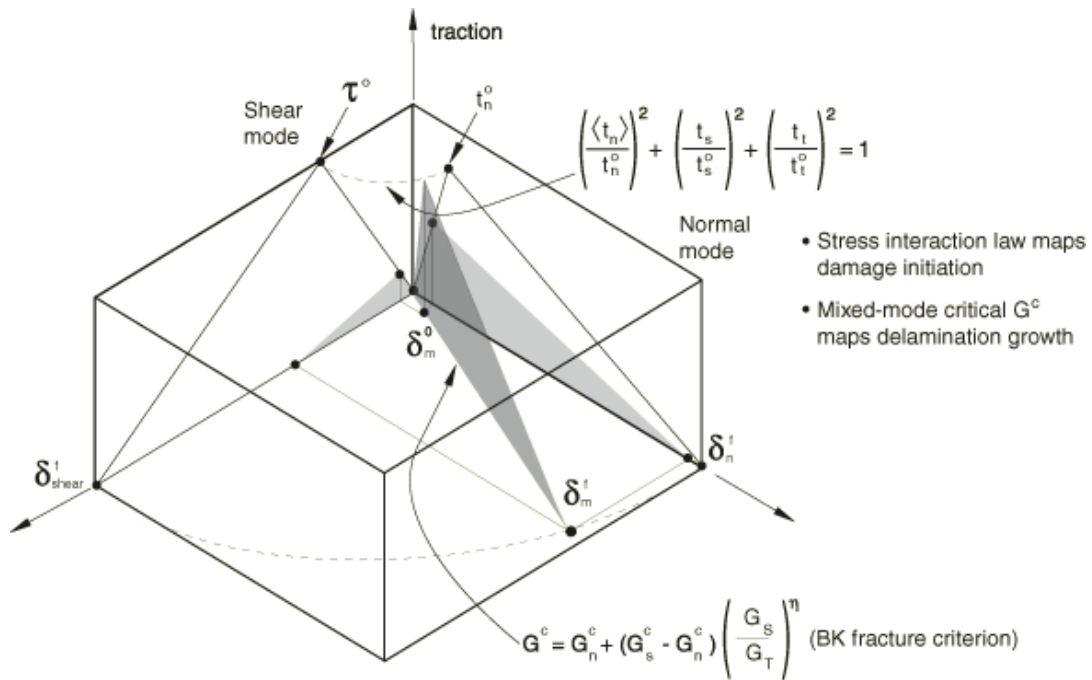


Figure 2-26: Mixed-mode fracture response based on the quadratic nominal stress and BK criteria.

[33]

Before damage initiation, unloading of the structure will follow purely the linear elastic response described in equation (15) and displayed in Figure 2-24. However, should unloading occur once the material has been damaged, the unloading path will be along a line connecting the current traction in the damaged state and the origin of the TSL. Reloading will then follow the same path until the damage curve is reached again and the traction declines upon further loading. This behaviour is implemented in ABAQUS for all shapes of cohesive laws and is equivalent to a decrease in elastic stiffness for the damaged part. Unloading and

reloading after damage can be observed in Figure 2-24. However, Scheider [40] gives a more detailed description of the unloading process and refers to this particular type as cleavage unloading, in contrast to the ductile unloading, where the stiffness is not damaged and a separation is retained. [33; 36; 40; 41; 43; 48]

### Brittle and ductile fracture

As indicated in Figure 2-22 c), the bilinear traction-separation law is mostly regarded for the simulation of brittle fracture, whereas many authors use a trapezoidal or similar, more rounded form to describe ductile crack propagation. In contrast to the triangular shape, the trapezoidal form has an additional parameter  $\delta_{f1}$ , which marks the beginning of decline after the area of constant traction. Relating to Figure 2-27 from Heidari-Rarani and Ghasemi [52], the following equation (29) describes the evolution of the damage variable  $D$  for the trapezoidal TSL. [39; 40; 43; 47; 48; 52–60]

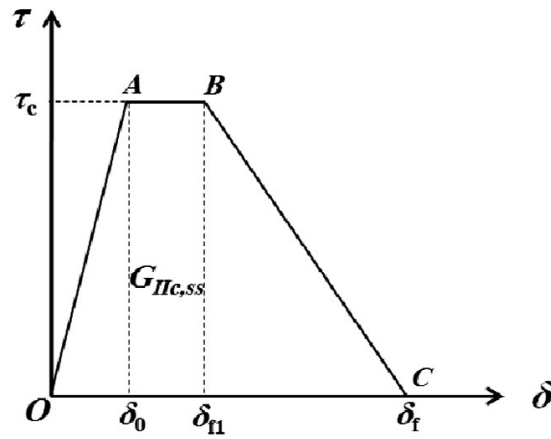


Figure 2-27: Trapezoidal TSL for cohesive behaviour. [52]

$$D = \begin{cases} 0, & 0 < \delta < \delta_0 \\ 1 - \frac{\delta_0}{\delta}, & \delta_0 < \delta < \delta_{f1} \\ 1 - \left[ \frac{\delta_0}{\delta} \left( \frac{\delta_f - \delta}{\delta_f - \delta_{f1}} \right) \right], & \delta_{f1} < \delta < \delta_f \end{cases} \quad (29)$$

### Determination of parameters

Due to the fact that the cohesive model is a phenomenological approach, most parameters are not related specifically to the material and have to be experimentally determined. Only the cohesive energy at failure  $\Gamma_0$  is equal to the J-integral at crack initiation and thus is corresponding to the fracture energy in LEFM. However, this statement is only valid if the assumptions made for the J-integral are fulfilled. Since no unloading is permitted for the

determination of  $J$ , its correlation with  $\Gamma_0$  is applicable only under certain preconditions for propagating cracks, as the new crack surfaces are completely unloaded. [39; 40; 61; 62]

Several studies have been conducted on how to determine the shape and appropriate parameters for the TSL. Throughout these studies, one of the most popular techniques to obtain the maximum traction is to simulate a notched tensile specimen and determine the centre stress at fracture onset from the simulation, as Figure 2-28 suggests. [39; 47; 63; 64] Also shown in Figure 2-28, the cohesive energy is oftentimes evaluated by the use of compact-tension (CT) specimens and interpreted as the J-integral at the onset of cracking. [39; 47; 64] A wide variety of authors also uses the CT-experiment ([43; 55; 64]) or a three point bending test ([42; 62; 65; 66]) to calibrate all parameters of the TSL in an iterative process of simulation and comparison. Additionally, there is a growing database of literature values and a further possibility to obtain TSL parameters with the aid of micromechanical simulation in representative volume elements with damage based on void nucleation models, like the Gurson model. [43; 47; 48; 51; 56; 57; 65; 67] However, these methods require either a lot of tests or the knowledge of parameters for other damage models. For this reason Wang and Ru [68] aimed to establish a method to acquire the maximum traction and the cohesive energy  $\Gamma_0$  based on just the uniaxial stress-strain curve. Throughout all these methods, special care has to be taken as the obtained parameters are dependent on the mode-mix ratio. [43; 51; 62; 65]

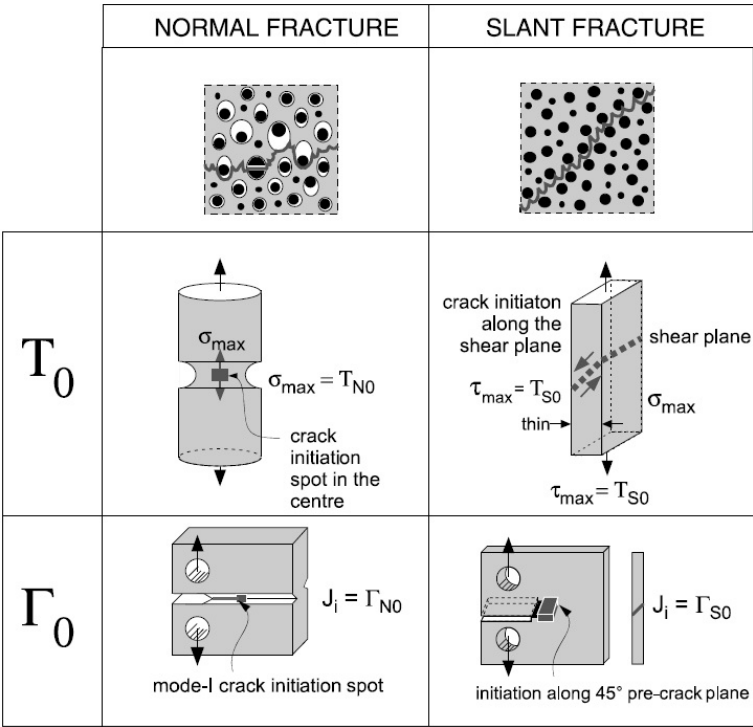


Figure 2-28: Determination of maximum traction  $T_0$  and cohesive energy  $\Gamma_0$  parameters for normal and slant fracture. [39]

## Comparison with other techniques

The cohesive model is probably the most general and versatile of all the described methods. It is not bonded to pre-existing cracks as most other surface-based methods, but is also capable of describing crack initiation. Unlike VCCT, brittle as well as ductile crack propagation is covered by this technique. Compared to XFEM, where the cohesive model is incorporated, this technique cannot model arbitrary crack paths, but is in exchange applicable to elastic-plastic material behaviour. With user-defined elements and materials it is further possible to incorporate own traction-separation laws and combine them, for instance, with a diffusion or phase transformation model. [33; 36; 40; 43; 54–56; 59; 63]

### 2.2.3 Multipoint constraint

Multipoint constraints (MPC) in ABAQUS can be rather general and allow constraining different degrees of freedom of a model. However, this section aims to shortly introduce the SLIDER MPC, as it proved useful in the later simulation. [33]

The SLIDER multipoint constraint restricts a given node or node set  $p$  to remain on a straight line defined by two other nodes  $a$  and  $b$ , as shown in Figure 2-29. However, the restricted nodes are allowed to move along the line and the line itself can change in length. Therefore the thinning behaviour is retained while the nodes are not able to separate in the orthogonal direction. This MPC is not supported in the ABAQUS user interface and must be manually written into the input file following the \*MPC keyword and providing the constrained nodes  $p$ , succeeded by the nodes  $a$  and  $b$  defining the line. [33]

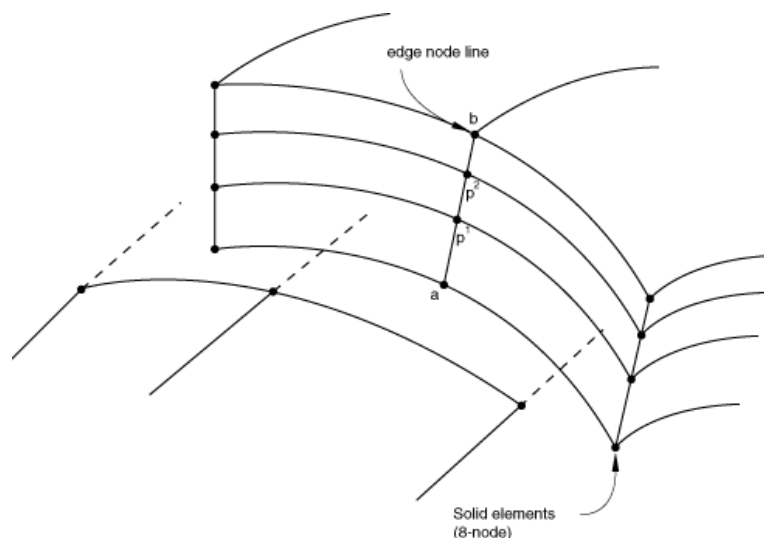


Figure 2-29: Multipoint constraint SLIDER forcing the nodes  $p^i$  to remain on a straight line between node  $a$  and  $b$ . [33]

## 3 Crack growth simulation

As now the theoretical information regarding the production process, material and simulation techniques has been provided, this chapter shall deal with the actual simulation and the application of material concepts and parameters. The ultimate goal is to implement a method suitable for studies on crack growth into a pre-existing simulation. Starting with an explanation on the preliminary work, test models for crack growth simulation are introduced in the following. Lastly, the implementation of the model into the pre-existing simulation is covered. Since ABAQUS is a dimensionless program, all data has to be provided in consistent units, which will be the system of mm-kg-ms throughout this work.

### 3.1 Preliminary Work

Tomasch et al. [69; 70] have conducted several simulations for the direct press hardening of 20MnB8. Consisting of four coupled temperature-displacement steps including forming, press-hardening, withdrawal and springback, the developed model can predict stresses, temperature distribution and martensite phase fraction based on the initial temperature of the steel sheet. This temperature is in the range of 510 to 660 °C and accounts for the pre-cooling technology described in the last two paragraphs of section 2.1.4.3. Predefined fields are used to set the initial temperature, which is 25 °C for all tools. However, as only the forming step is of interest for this work, the other steps will be only mentioned shortly. [69; 70]

The model shown in Figure 3-1 has a symmetry boundary condition along all surfaces on the left side, as it shows the right half of the real arrangement. All tools are constrained in their rotational movement and the punch is furthermore fixed in y-direction. A special functionality is implied on the uppermost point, which is connected to the die and governs the die movement and acts as a connector point. Clamping of the blank between die and holder is ensured by the connector force with time dependent amplitude, acting between the uppermost point related to the die and a point on the holder. General contact with friction and a clearance dependent thermal conduction governs the interaction between the blank and the tools. Additionally, the upper and lower surface of the blank exhibits heat loss by a temperature dependent convection coefficient. [69; 70]



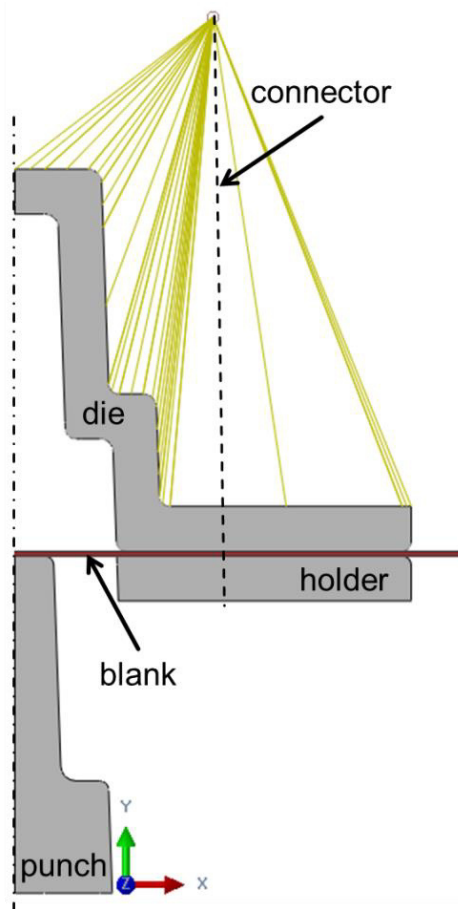


Figure 3-1: Original model consisting of a blank clamped between die and holder, a punch and a connector. [69]

While the tool material is elastic with uniform density, heat conductivity and specific heat, the 20MnB8 blank is more complicated. All properties except the density are temperature dependent, which includes Young's modulus, Poisson's ratio, expansion coefficient and plastic parameters as well as thermal conductivity and specific heat. Although plasticity is additionally dependent on strain rate, this dependency relatively minor compared to the temperature dependence. Also heat generated by inelastic deformation is accounted for. Martensitic transformation is calculated with the aid of USDFLD subroutine and field variables, while SDVINI, UEXPAN and HETVAL subroutines are also in use. [69; 70]

### 3.2 Three point bending test models

As described in section 2.2.2, there are several ways to study cracks in ABAQUS. However, the cohesive model is the most appropriate considering that crack growth should be implemented into the model from Tomasch et al. [69]. Related to their name, static

models do not allow the study of growing cracks, whereas the other methods described are either not sophisticated enough or are inapplicable due to the plastic material and cracking behaviour. Based on the work of Sung et al. [59] and Vanapalli et al. [62], a three point bending test is chosen to investigate and compare the surface-based and the element-based cohesive zone model.

### 3.2.1 Model dimensions and boundary conditions

Two models sharing all properties except the different cohesive approach are developed. These models are also closely related to the original model shown in Figure 3-1, so to assess the cohesive behaviour under similar circumstances as in the pre-existing simulation. Figure 3-2 below illustrates the three point bending test model where punch and bearings are modelled as analytical rigids with 3 mm radius, according to the smallest radius in the original tool. The original blank thickness of 1,51 mm is retained and the length is chosen equally to the distance from the symmetry plane to the blank end in Figure 3-1, which is 150 mm. As the implementation of analytical rigids with the ABAQUS user interface imposed some problems, punch and bearings are manually programmed into the input file. Although the chosen distance of 24 mm between the bearings would not require the whole 150 mm blank to be modelled, it is nonetheless desired to do so as the mesh could later on more easily be transferred.

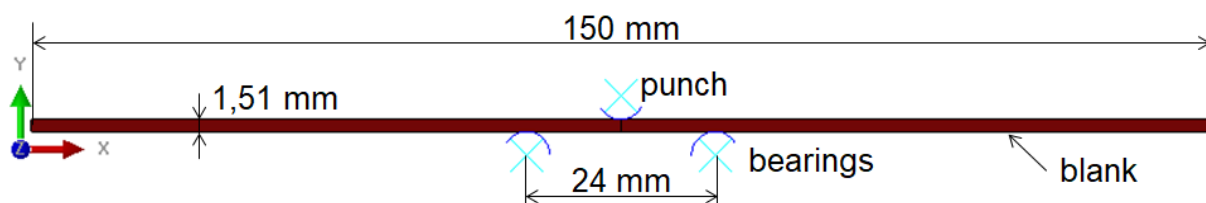


Figure 3-2: Three point bending test model with dimensions.

For the boundary conditions, both bearings were denied any translational or rotational movement, whereas only rotation and displacement in x-direction is restrained for the punch. By the means of frictionless contact interactions between punch and blank as well as bearings and blank, the blank is sufficiently constrained in y-direction. However, the uppermost middle point, as marked in Figure 3-3 c), is chosen as symmetry point and fixed in its horizontal position. Loading is provided by moving the reference point of the punch 15 mm downwards. With the aid of a predefined field, different temperatures can be applied to the blank, whose 20MnB8 material possesses the same temperature dependent elastic and plastic properties as the original model, but without capability of martensitic transformation.

Additionally, a 10  $\mu\text{m}$  [17; 23] thick layer is implemented on each side of the blank, as Figure 3-3 shows, thus simulating the galvannealing (GA) process. This layer is initially assigned with material properties of intermetallic  $\Gamma$ -phase, as it is assumed to consist only of  $\Gamma$  at the present temperatures (see Figure 2-6 b)). However, if necessary it could also be given the characteristics of other phases, which altogether will be described in section 3.2.4. Although not considered in this work, the layer could be further sub-divided to match the structure of Figure 2-6 a) in section 2.1.3.1.

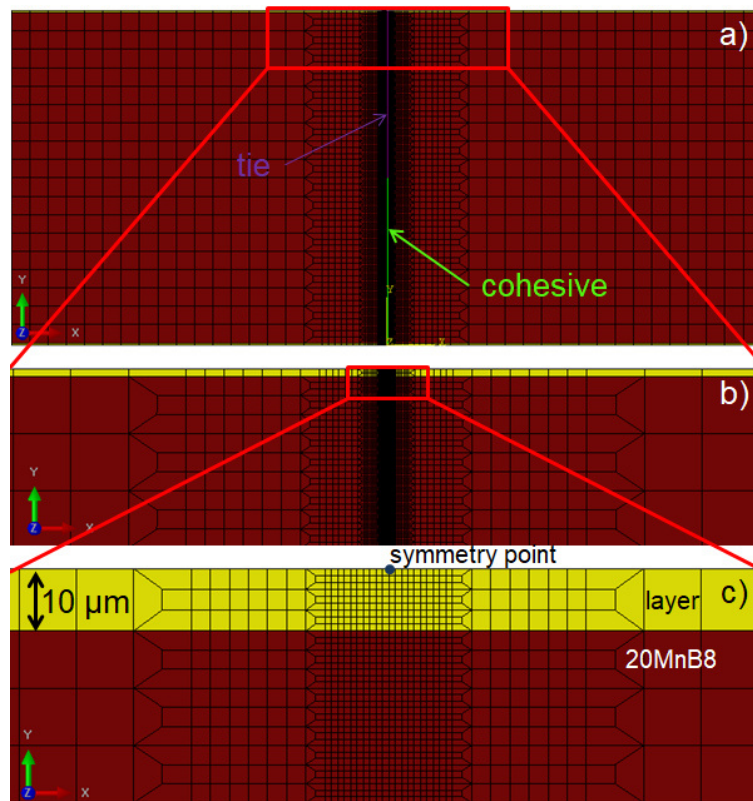


Figure 3-3: Blank mesh with increasing magnification starting from a) original thickness with coarsest elements and interactions to c) showing the smallest elements, intermetallic layer and symmetry point.

### 3.2.2 Meshing

As mentioned in section 2.2.2.4, the cohesive model is sensitive to the mesh size on the parting interface. Therefore a fine mesh in the direct vicinity of the interface is chosen in order to accurately capture the cracking process, whereas a transition to a coarser mesh on the outside is made to save computing time. Quadratic plane strain CPE4 elements are used, for which the edge length  $x$  is related to the distance  $h$  between the top and bottom layer and the number of mesh transitions  $p$ , as equation (30) states. As the element in each

succeeding partition is three times the size of the current element, the base for the exponent  $b$  in equation (30) is 3.

$$x \cdot 3^p = \frac{h}{2} \quad (30)$$

Half the distance between the layers is chosen so to partition only one half of the part and copy the pattern to the other. Rewriting equation (30) gives the element size  $x$  for each partition as equation (31) shows.

$$x = 10^{\left(\log \frac{h}{2} - p \log 3\right)} \quad (31)$$

With Figure 3-2 giving the original blank thickness of 1,51 mm and Figure 3-3 showing the 10  $\mu\text{m}$  thick layer for each side, the layer distance  $h$  is 1490  $\mu\text{m}$ . For a reasonable mesh size, a number of six partitions is chosen, which gives element sizes of 1,022  $\mu\text{m}$ , 3,066  $\mu\text{m}$ , 9,198  $\mu\text{m}$ , 27,593  $\mu\text{m}$  and 82,778  $\mu\text{m}$  in ascending order from the crack interface. It should be noted that the last mesh transition to elements with 248,333  $\mu\text{m}$  edge length is not carried out as it seems to generate too coarse elements. The first partition consists of ten elements counted from the crack interface before the transition element is reached, whereas every succeeding partition has a number of six elements between the transition elements. The reason is to avoid producing a sudden jump in element sizes.

Due to the layer being of arbitrary size, it is not included in equation (31). In order to match the other element sizes, the layer is divided into nine elements, resulting in 1,111  $\mu\text{m}$  as smallest element size. Element sizes in subsequent partitions are also three times larger than in the current one according to the aforementioned partitioning. From the point where one side is equal to the layer thickness, the other side is set to match the underlying elements.

### 3.2.3 Model differences

Using the surface-based approach, two separate parts have to be connected via a surface interaction. In this model only a part of the interface is actually governed by means of a traction versus separation law, as the green section marked as cohesive in Figure 3-3 a) indicates. For the study of rather small-scale crack growth, it is sufficient to investigate only half the blank thickness regarding the cohesive behaviour and connect the left and right parts via a tie constraint on the upper model half to prevent through-cracking, thus achieving a more stable solution process.

The element-based approach offers several methods to implement cohesive elements, some of which have been shortly mentioned in section 2.2.2.4. However, the method of choice for this work is the insertion of a cohesive seam consisting of COH2D4-elements alongside a partitioning line of a part. These elements are similar to the first element from Figure 2-23 in section 2.2.2.4 and can be placed with the edit mesh option in the mesh module of ABAQUS. It must be noted that depending on the version of ABAQUS this option may not be supported, though.

Creating an initial crack is more easily done via surface interactions, as only a node set of the slave surface which is initially in contact with the master surface has to be specified. Figure 3-4 a) shows the slave contact node set (blue) in relation to the master surface (green). Excluding the layer from the initial contact node set is equivalent to a crack, but with the ability to still resist interpenetration even on the crack surface on the layer. Contrasting that, the element-based approach requires geometrically modelling the crack (opening of 2  $\mu\text{m}$  on the outside of the layer) and placing the cohesive seam on a parting line underneath the crack (see Figure 3-4 b)). Altering the crack length is therefore more difficult and time consuming. Additional contact problems regarding the initial crack surfaces as well as on deleted cohesive element surfaces under pressure are also introduced.

In summary, the contact model consists of two parts connected with a cohesive interaction and tie constraint to prevent through-cracking as well as an ideally thin initial crack. Although the cohesive element model shares mesh and material properties with the contact model, it is originally only one part with a geometrically modelled crack and a cohesive seam on a parting line through the whole thickness, which would allow through cracking.

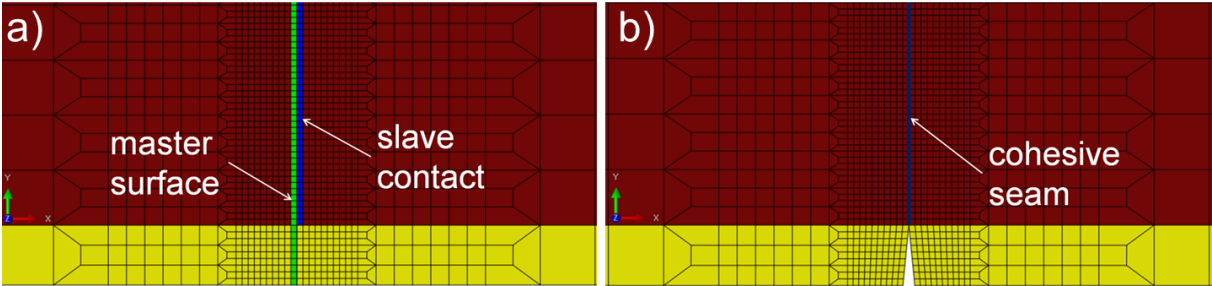


Figure 3-4: Implementation of a crack using a) slave contact relative to the master surface in the surface interaction approach and b) a geometrically modelled crack with cohesive seam in the element based approach.

### 3.2.4 Material properties

Generally, the elastic and plastic properties of 20MnB8 are the same as in the original simulation mentioned in section 3.1 and are provided by Tomasch et al. [69], but they cannot be addressed for confidentiality reasons. Temperature and strain rate dependencies are taken into account. However, heat capacity, thermal conductivity and all subroutines related to martensitic phase transformation are disregarded.

Concerning the intermetallic zinc-layer, no temperature dependence of the relevant material properties has been found. The Young's modulus at room temperature is taken from He et al. [23] (see Table 2 in 2.1.3.2) for all zinc modifications. In order to maintain the stiffness relation between steel and layer, each phase Young's modulus degrades with temperature at the same percentage amount as the one from 20MnB8. For the Poisson's ratio, no data at all is found and a constant value of 0,3 is assumed for all temperatures and modifications.

Also the plastic behaviour at room temperature in form of flow curves for all zinc-modifications is recreated in Figure 3-5 according to He et al. [23], as it is seen before in Figure 2-8 from section 2.1.3.2.

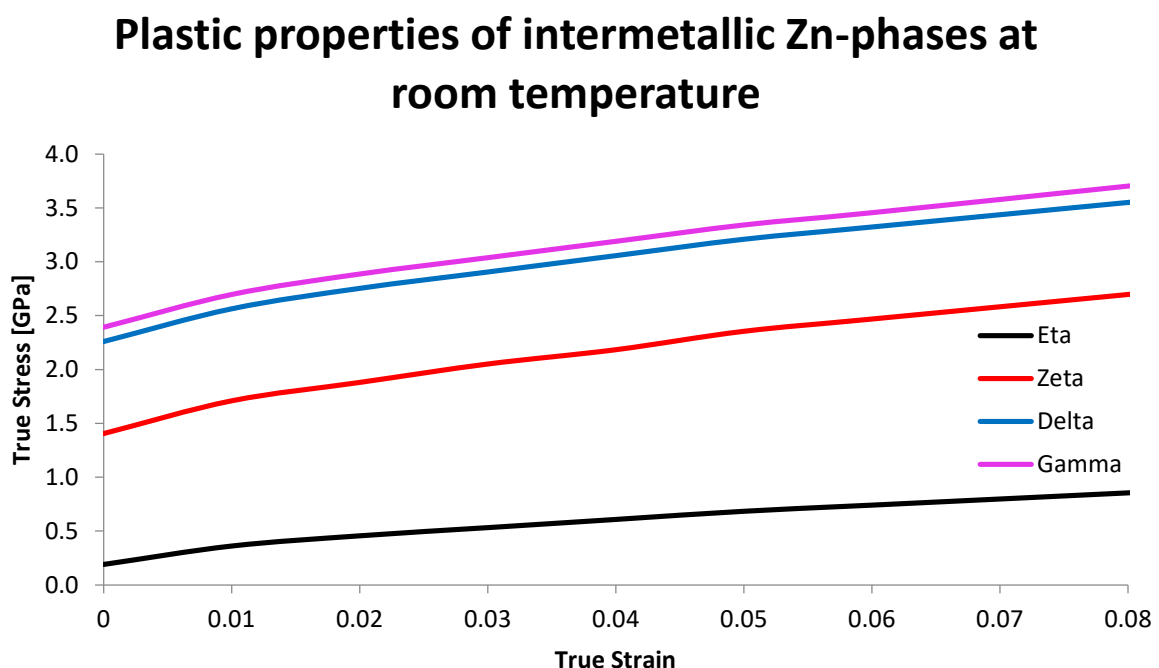


Figure 3-5: Recreation of intermetallic Zn-phase plastic properties at room temperature according to He et al. [23].

For the same reasons as for the elastic properties, also the plastic behaviour of the zinc-layer is made temperature-dependent. As mentioned in 3.2.1, the layer is assumed to consist only of  $\Gamma$ -phase at the temperatures present during deformation. Therefore Figure 3-6 visualizes only the flow curve temperature dependence of  $\Gamma$ , but also the other modifications behave in a similar manner. For the plasticity onset at 0 true strain, the onset stresses  $\Gamma_{onset}(T)$  are related to the room temperature value  $\Gamma_{onset}(20\text{ }^{\circ}\text{C})$  by the same percentage as the stresses for 20MnB8, indicated by equation (32).

$$\Gamma_{onset}(T) = \frac{20MnB8_{onset}(T)}{20MnB8_{onset}(20\text{ }^{\circ}\text{C})} \cdot \Gamma_{onset}(20\text{ }^{\circ}\text{C}) \quad (32)$$

Further development of the stresses  $\Gamma(\varphi, T)$  with increasing true strain  $\varphi$  is governed by equation (33) and follows the identical ratio of the stress values 20MnB8( $\varphi, T$ ) over their corresponding onset stress 20MnB8<sub>onset</sub>( $T$ ).

$$\Gamma(\varphi, T) = \frac{20MnB8(\varphi, T)}{20MnB8_{onset}(T)} \cdot \Gamma_{onset}(T) \quad (33)$$

Although this extrapolation lacks reasoning, especially considering phase stability not only for  $\Gamma$ , but even more for the other modifications, it is believed to be useful to obtain a stable solution process. Equation (33) furthermore ensures a monotonic increase in true stress with growing true strain.

### Temperature dependence of $\Gamma$ -phase plastic properties

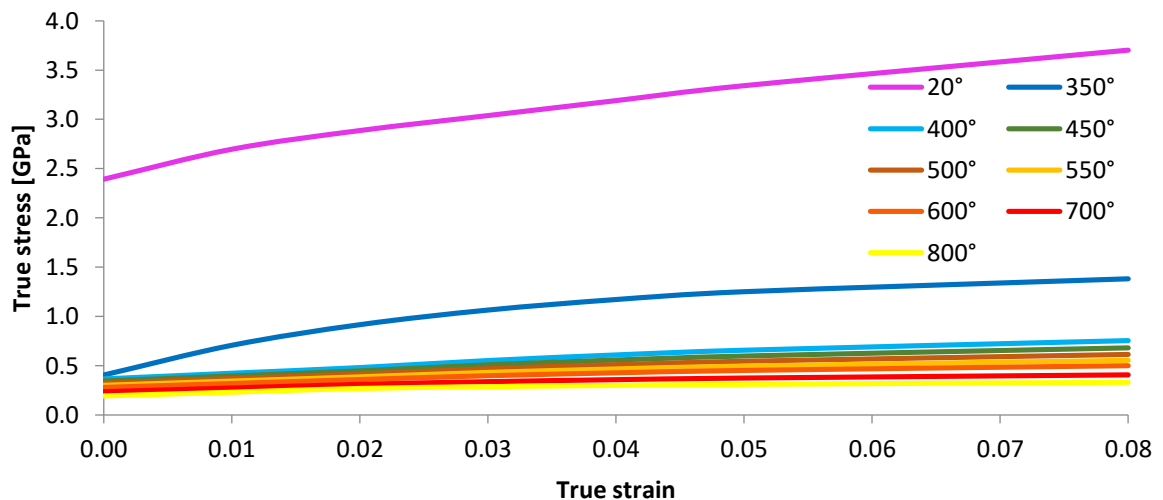


Figure 3-6: Temperature dependence of gamma-phase flow curve. The graph at 20 °C is according to He et al. [23].

### 3.2.5 Traction-separation laws

Presumably the most crucial and also the most delicate part of the crack growth simulation is the traction-separation law for the cohesive behaviour. Not only should it resemble the real material performance, yet it is also critical for numerical stability. Since the zinc-layer is presumably already cracked, only the bulk material parameters are considered for the TSL. However, as little to no experimental data is available, the construction of the TSL is mostly based on different literature.

As already mentioned in section 2.2.2.4, firstly the linear elastic parameters need to be specified. As suggested by Turon et al. [45], a penalty stiffness  $K_{nn}$  that is ten times larger than the bulk material stiffness at the corresponding temperature is chosen. Similarly, the stiffness coefficients  $K_{ss}$  and  $K_{tt}$  are related to the shear modulus  $G \times 10$ , which is calculated according to equation (34) [31] using the Young's modulus  $E$  and Poisson's ratio  $\nu$  from the 20MnB8 bulk material.

$$G(T) = \frac{E(T)}{2(1 + \nu(T))} \quad (34)$$

Although a number of traction-separation laws are used throughout different iterations of the simulation process, all share this common elastic behaviour. Trials with the original material stiffness have been quickly abandoned as a disproportional large part of the cohesive energy would be elastic.

A lot of different parameter sets for the traction-separation law have been developed and continuously adjusted throughout this study, leading to the following and for now final forms. In use for both the simulation of the three point bending test as well as the press hardening process is a trapezoidal TSL, which should be best suited to describe fracture in a plastic material, as discussed in section 2.2.2.4.

The onset of fracture is always governed by the quadratic stress (QUADS) criteria for cohesive elements and the quadratic traction criteria for cohesive contact, respectively. According to the von-Mises hypothesis, the maximum traction  $T_0$  for the first and second shear direction is the one for normal direction divided by the square root of three. Different sources use values in the range of the yield stress  $\sigma_y$  up to 3,7 times  $\sigma_y$  [71] or 4 times  $\sigma_y$  [53] for the maximum traction. As magnitudes from 1000 MPa [56] over 1100 MPa [72] to 1200 MPa [67] are used in the referred literature, a value of roughly 1100 MPa corresponding to the onset of plasticity in the material data provided by Tomasch et al. [69] is chosen as maximum traction for 20 °C. Using this reasoning to determine  $T_0$  at higher



temperatures would lead to extremely low maximum tractions. Therefore the high-temperature values are arbitrarily set to better match the press-hardening simulation with experimental values provided by Tomasch et al. [69]. Figure 3-7 shows the temperature dependent TSL with the aforementioned parameters for stiffness and maximum traction.

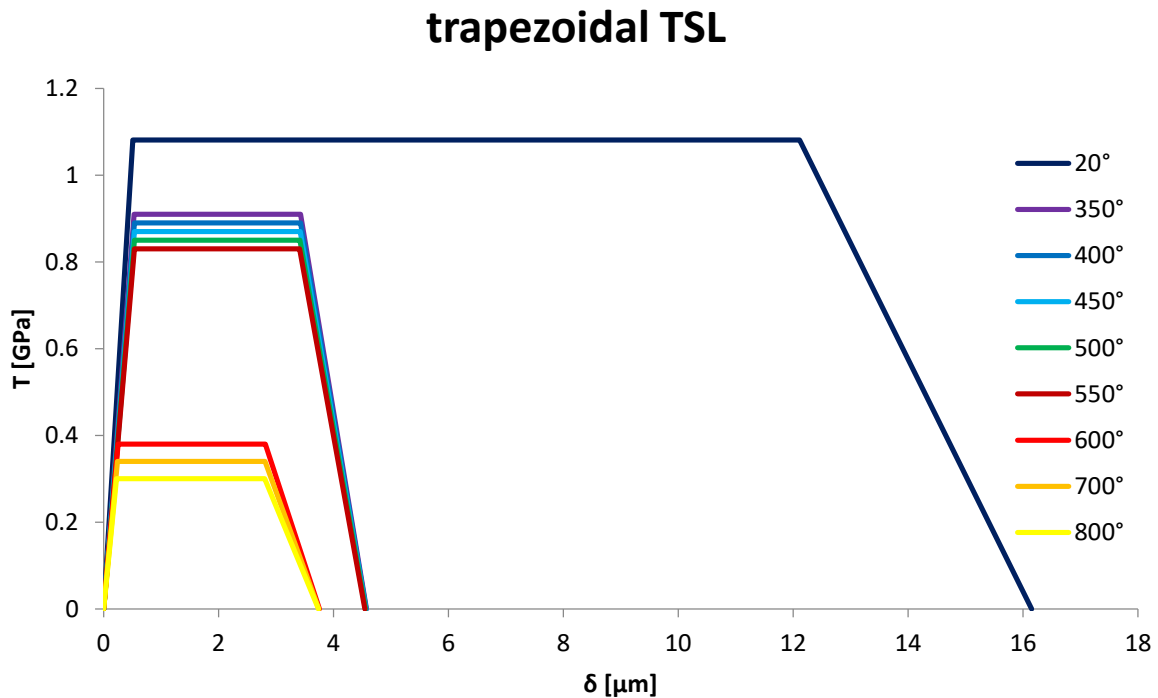


Figure 3-7: Trapezoidal traction-separation law with temperature dependent parameters.

For the implementation of a trapezoidal TSL in ABAQUS the damage variable  $D$  has to be directly specified as a function of the displacement measured from the point of fracture onset  $\delta_0$ . At first, the displacement at fracture  $\delta_f$  is calculated out of the three independent parameters stiffness  $K_{nn}$ , maximum traction  $T_0$ , and cohesive energy  $\Gamma_0$ . The range from  $\delta_0$  to  $\delta_f$  is then discretized into 3000 data points according to Heidari-Rarani and Ghasemi [52], who suggested to use at least 2000 points in order to minimize interpolation errors. The evolution of the damage variable  $D$  is then governed by equation (29) from section 2.2.2.4, but the variable  $\delta_{f1}$  marking the beginning of the decline of traction is set to  $0,75 \cdot \delta_f$  according to Scheider [40]. Therefore the last independent parameter is the cohesive energy  $\Gamma_0$ , which is equal to the area under the whole TSL and should not be confused with the fracture energy  $G^c$  describing only the area from damage initiation  $\delta_0$  on. For 20 °C reported values are mostly in the range of 5 N/mm [64] to 25 N/mm [56] for different steel grades, hence a cohesive energy of 15 N/mm is chosen according to Pandolfi, Guduru et al. [66] to give a reasonable maximum separation for room temperature. In analogy to stiffness and maximum

traction, also the cohesive energy is reduced at higher temperatures. It decreases linearly with the maximum traction, but therefore also exhibits the same jumps which are arbitrarily set for  $T_0$ .

For the sake of comparison, also a triangular traction-separation law is developed. This bilinear TSL, displayed in Figure 3-8, exhibits the same parameters  $K_{nn}(T)$ ,  $T_0(T)$  and  $\Gamma_0(T)$  as the trapezoidal one. Although also a tabular implementation in ABAQUS is possible, the damage evolution of the bilinear TSL is specified by writing the calculated fracture separations  $\delta_f(T)$  into the displacement-based linear softening option for cohesive behaviour.

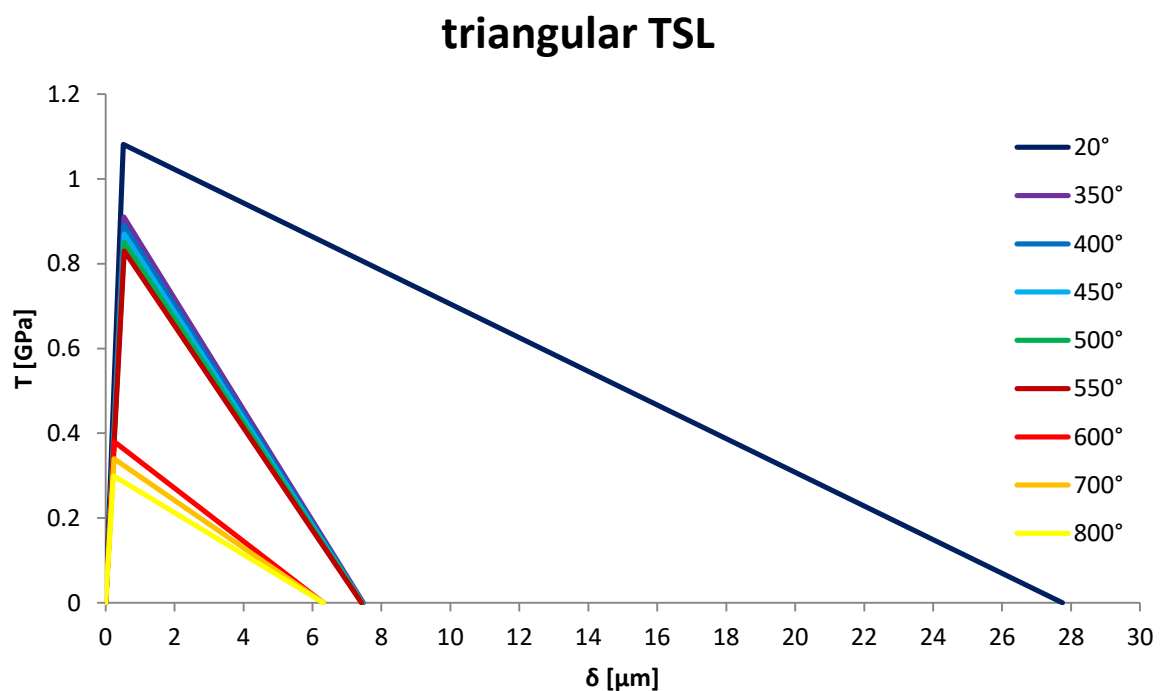


Figure 3-8: Triangular traction-separation law with the same temperature dependent parameters as the trapezoidal TSL.

### 3.3 Press-hardening model

Ultimately, two rather similar models for the simulation of crack propagation during an actual press-hardening operation are developed. Both use one and the same submodel for reasons of comparability and computational efficiency, with the only difference being the boundary conditions. Whereas one model is entirely run by submodel boundary conditions, the other one only partly uses them, instead utilizing contact interactions between the top and bottom surfaces of the model and the three tools punch, die and holder. This approach is

more closely related to the preliminary work from Tomasch et al. [69], but rather uses analytical rigid tools than deformable ones, as no heat transfer is to be calculated during this simulation. Additionally, the contact on the outside part of the upper and lower surface is assumed frictionless for better initial contact, whereas the majority of the middle surfaces are regarded with a friction coefficient of 0,25. All the normal contact behaviour is modelled as hard contact. Figure 3-9 shows the analytical rigid tools together with the position  $x$  of the crack within the submodel. If the value of  $x$  is varied, different positions of the blank can be studied regarding their cracking behaviour. Although the similarity to the original model from Tomasch et al. [69] (Figure 3-1 in section 3.1) is evident, the use of analytical rigid tools together with connector elements can impose some additional constraints and overconstraining has to be carefully avoided.

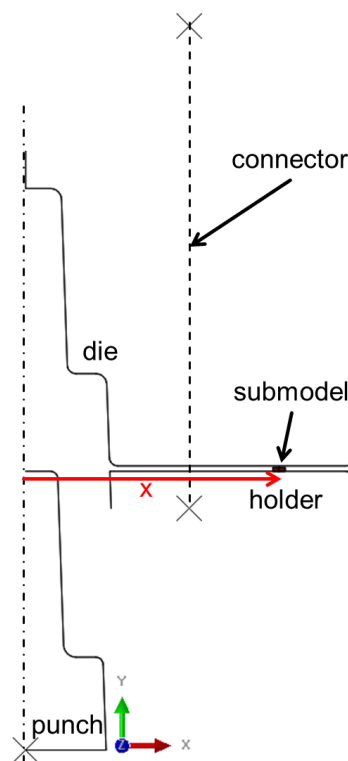


Figure 3-9: Simulation of the press-hardening process by means of analytical rigid tools and submodel technique. The distance  $x$  marks the position of the crack, located in the middle of the submodel. Variations of  $x$  address different positions of the original blank.

To drive the submodels, the forming step in the coupled temperature-displacement model from Tomasch et al. [69] is re-calculated for two different initial blank temperatures, 510 °C and 660 C. For both submodels, the left and right surface areas in Figure 3-10 b) are driven by displacement-based submodel boundary conditions (BCs). These BCs impose the degrees of freedom (dof) 1, 2 and 6, corresponding to displacement in  $x$ - and  $y$ - direction and

rotation around the z-axis, from the global model onto the submodel. In contrast to that, the top and bottom surfaces of the submodel are either constraint by a force-based submodel BC for the model without tools or by contact interactions with the tools for the other modelling approach. Both models use contact based cohesive behaviour with a tie constraint on the lower half, very much like the three point bending test model. To avoid buckling of the crack faces in the model without tools, the SLIDER multipoint constraint (MPC) is used to force the nodes marked in Figure 3-10 to lie on the same line throughout the whole forming process.

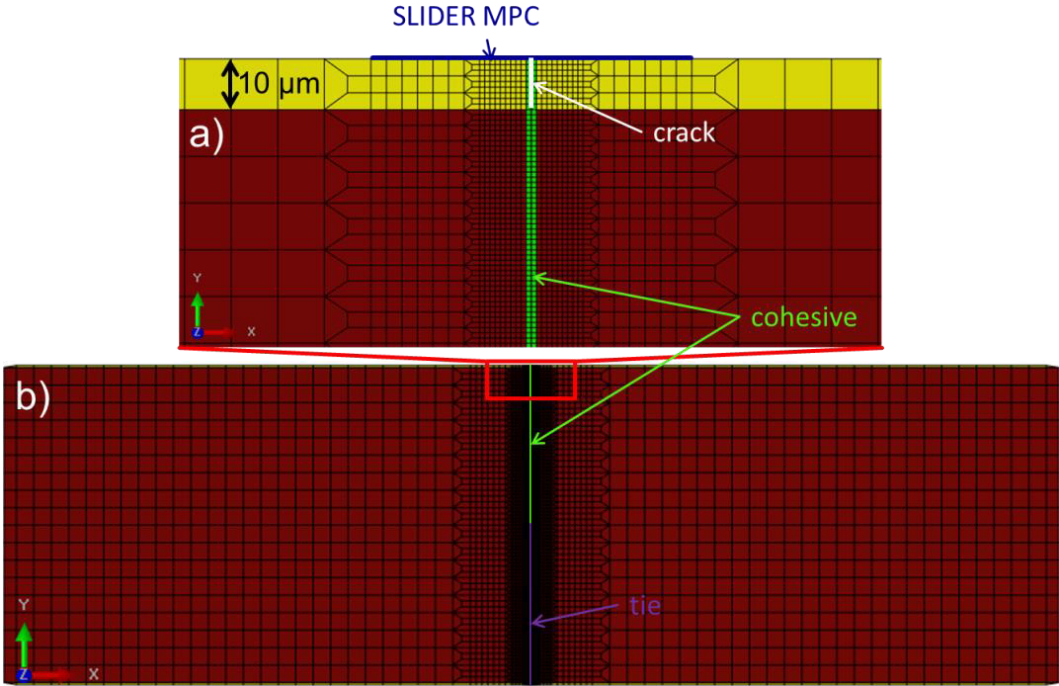


Figure 3-10: Magnification of the crack area a) showing the through cracked layer and region of SLIDER MPC in the whole submodel b) with regions of cohesive interaction and tie constraint. The left and right boundary of the submodel in b) exhibit a displacement-based submodel boundary condition, whereas the top and bottom surfaces are constraint by either force-based submodel BC or interactions with the tools for the respective models.

All other parameters, such as meshing, material models and traction-separation laws are analogous to those defined in the three point bending test model. However, the temperature distribution in the submodel is governed by interpolating the results from the coupled temperature-displacement simulation of the original model onto the submodel. This is done via the PREDEFINED FIELDS option in the load module of ABAQUS. Thereby the keyword DRIVING ELSETS together with the global model element set and the submodel node set assures that only temperatures from the global model and none from the neighbouring tools are taken into account.

# 4 Results and discussion

With all the models and parameters described in the previous chapter, this section aims to summarize, analyse and discuss the results obtained from the simulations. Starting with a comparison of the different simulation approaches with the aid of the three point bending test simulation, an assessment on the most viable simulation method is made. This general crack growth description is then used in two different variations for the crack growth simulation during actual press-hardening, also addressing multiple positions with the most stable variation.

## 4.1 Analysis of the three point bending test simulation

In order to obtain the best approach for further crack growth simulations, firstly the three point bending test simulation is evaluated regarding the form of the TSL and implementation of the cohesive law into the model. Figure 4-1 compares the fully deformed and the undeformed state of the three point bending test model at 510 °C, displaying the von-Mises stress plot in GPa. At the end, the punch exhibits a displacement of 15 mm in negative y-direction within a time of 800 ms.

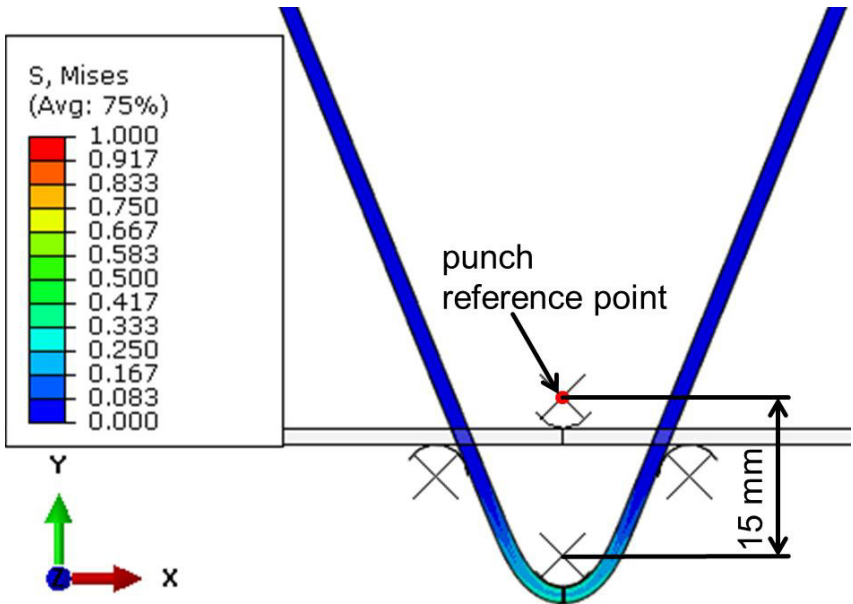


Figure 4-1: Comparison of undeformed and deformed state of the 510 °C three point bending test, showing the von-Mises stress in GPa.

### 4.1.1 510 °C three point bending test

For 510 °C, all the simulations are fully converged and both cohesive contact implementations give exactly the same results, as it can be seen in Figure 4-2 and Figure 4-3. As clarification, the denomination is done by providing the type of implementation followed by the form of the traction-separation law. In this case, “contact” describes the implementation as cohesive contact interaction whereas “seam” indicates a seam of cohesive elements. Figure 4-2 displays the von-Mises stress around the crack in GPa. Both cohesive contact traction-separation laws are shown in a), as they are exactly the same, whereas b) illustrates the cohesive seam approach.

It can be seen through comparison of Figure 4-2 a) and b) that all the different techniques yield the same results for 510 °. Still two things are apparent in this figure. Firstly, for the cohesive element seam in Figure 4-2 b) the damaged, but not yet deleted elements are visible. Although the cohesive contact approach technically exhibits the same damage, no elements are displayed but rather an indication about the damage state on the slave surface can be requested, making it a little bit trickier to determine the crack tip. Secondly, regardless of the used technique, the initial crack surfaces exhibit some form of bulging, which most likely is not a good representation of reality.

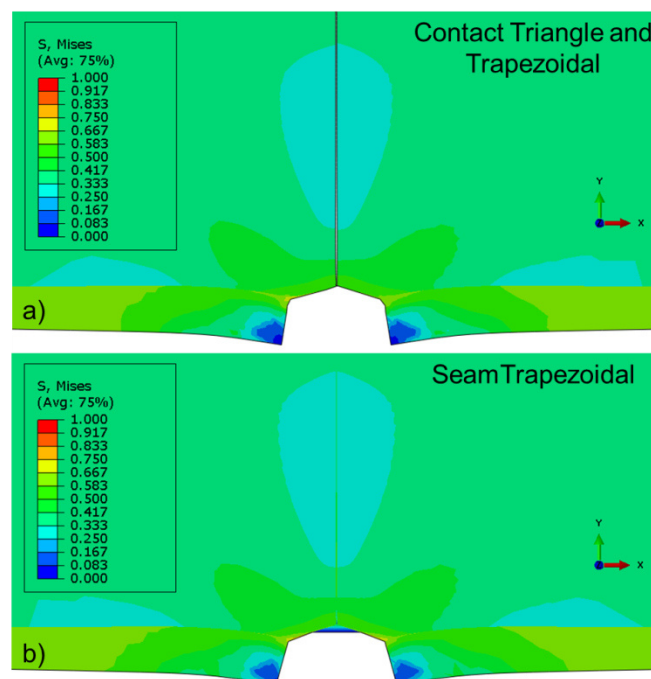


Figure 4-2: Crack area of the 510 °C three point bending test a) for both the triangular and trapezoidal TSL cohesive contact and b) for trapezoidal TSL cohesive elements. In both pictures the von-Mises stress is plotted in GPa.

Additionally to the stress plot in Figure 4-2, the force-displacement curve of the punch reference point is evaluated for all techniques. As the displacement is really in the negative y-direction, all the values are made positive for the construction of the graphs in Figure 4-3. Although the same results are obtained for the stress plot, the entire stress-displacement relation for 510 °C in Figure 4-3 a) reveals a slightly higher elastic stiffness for the element based approach. Zooming into the peak of the plot in Figure 4-3 b) also shows a smoother behaviour of the cohesive contact modelling compared to the seam of cohesive elements, which exhibits some form of stepping.

The difference in stiffness might be a result of thickness effects in the element based approach, which are not regarded for surface contacts. However, this stiffness difference seems only very minor and is believed to affect neither the solution nor the computing process in a significant manner. Contrasting that, the stepping behaviour in the force-displacement relation of the element based model compared to smoother progression for surface contact might be a first hint for poorer convergence behaviour. This assumption is also backed up by a slight increase of computing increments from 436 to 450 for both contact models compared to the element model, respectively.

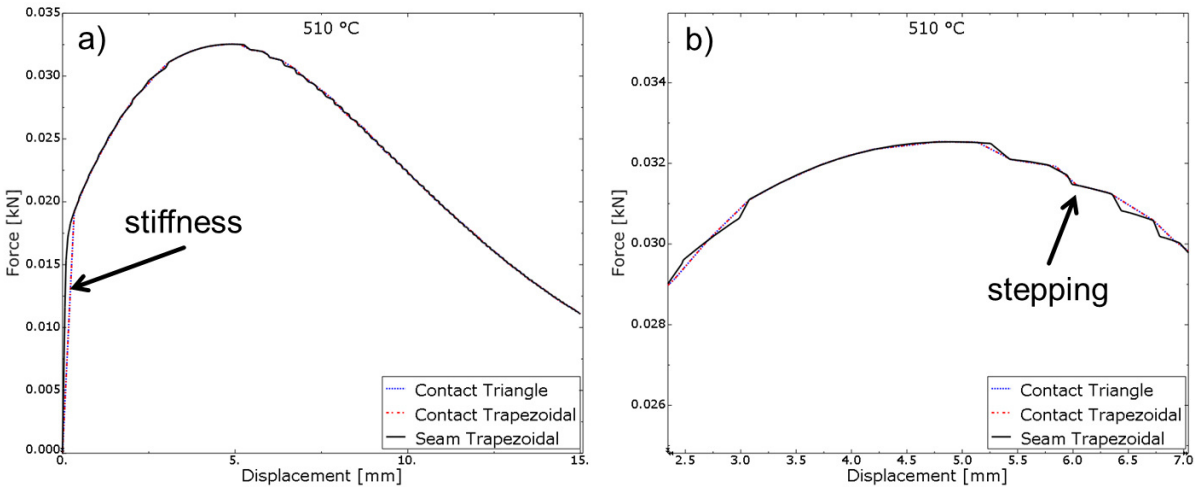


Figure 4-3: Force-displacement relation for different TSL forms and implementations of the cohesive law in the 510 °C three point bending test. The whole curve indicating a stiffness difference is shown in a), whereas b) gives a close-up view on the top of the curve, thus better displaying the stepping of the curve for the cohesive element seam.



#### 4.1.2 660 °C three point bending test

Unlike the simulation at 510 °C, the three point bending test results at 660 °C are not fully converged and job abortions at various times and for different reasons occur. Therefore not only the crack area, but also the overall deformation at the bending zone is displayed in the following figures. Starting with the triangular TSL for cohesive contact, Figure 4-4 a) gives an image of the testing model at the point of job abortion at 211 ms. A magnification of the crack shown in Figure 4-4 b) reveals that the first node of the initial crack tip is not detached properly from the slave surface despite being damaged and therefore forms a spike. This problem occurs on multiple occasions when simulating with cohesive contact exhibiting an initial crack. Either this spike formation leading to unnaturally deformed elements or rapid cracking might be the reason for the premature job abortion. For this technique, the crack penetrates the base material only a few microns deep before the calculation is abandoned after 121 increments.

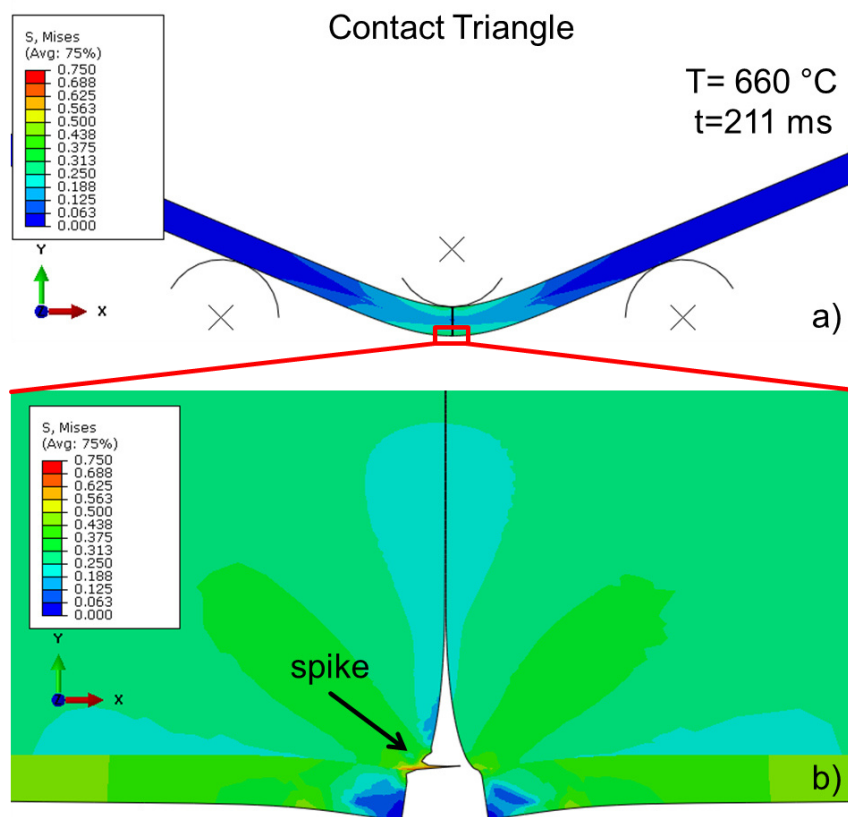


Figure 4-4: Three point bending model using the triangular TSL and cohesive contact at 660 °C. For the point of job abortion at 211 ms, a stress plot in GPa of a) the bending zone and b) a close-up image of the crack are displayed.



Considering the three point bending test at 660 °C, the cohesive contact formulation with trapezoidal traction-separation law appears to be the most stable one. Abortion of the calculation occurs after 2948 increments at 788 ms. However, the reason for this is that the crack runs into the upper model half early in the simulation and, since this half exhibits a tie constraint, excessively deforms the elements at the crack tip until the simulation is abandoned. For the sake of comparability, Figure 4-5 a) displays the cohesive contact model with trapezoidal TSL at roughly the same time (209 ms) at which job abortion takes place with triangular TSL (see Figure 4-4). A zoom on the crack area in Figure 4-5 b) also makes clear that the crack already reached the tied upper model half at this time.

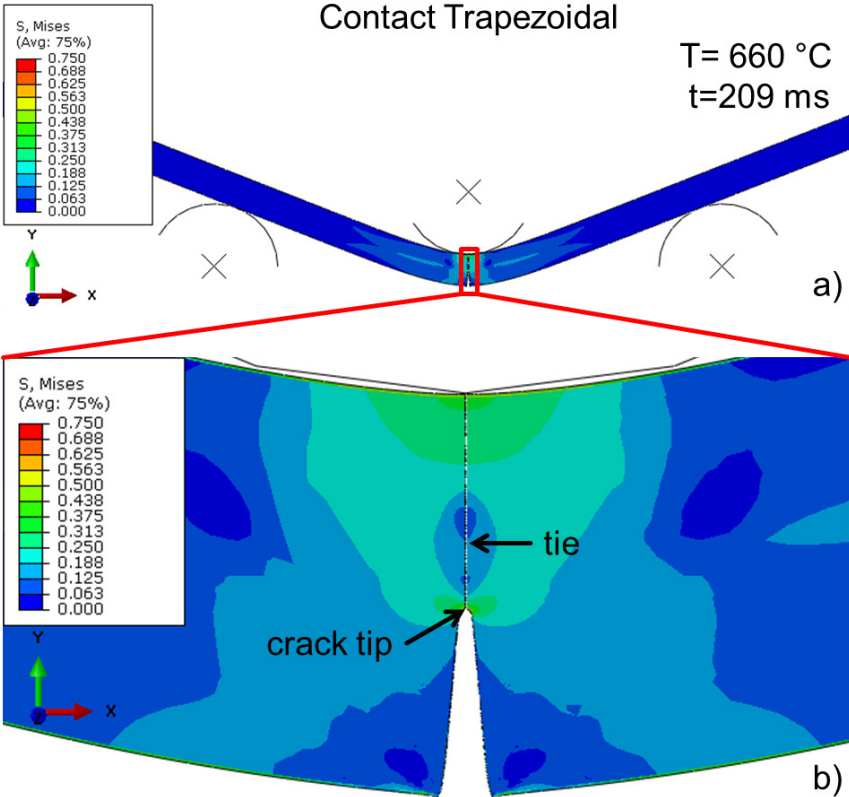


Figure 4-5: Three point bending test at 660 °C using the cohesive contact formulation with trapezoidal TSL. A von-Mises stress plot in GPa at 209 ms is shown in a) the bending zone and b) a magnification image of the crack area.

The model using a seam of cohesive elements with trapezoidal traction-separation law is displayed in Figure 4-6. At 660 °C, it exhibits job abortion after 172 ms, most likely due to rapid crack growth and subsequent rupture of the testing model. In the magnification of the crack area in Figure 4-6 b) it can be observed that the crack growth reaches already half into the model. Since the cohesive element seam runs through the entire model, through cracking is not prohibited. Therefore, the time increment at this stage becomes very small and

ABAQUS cannot handle the rapid crack growth anymore, which would be induced by further deformation.

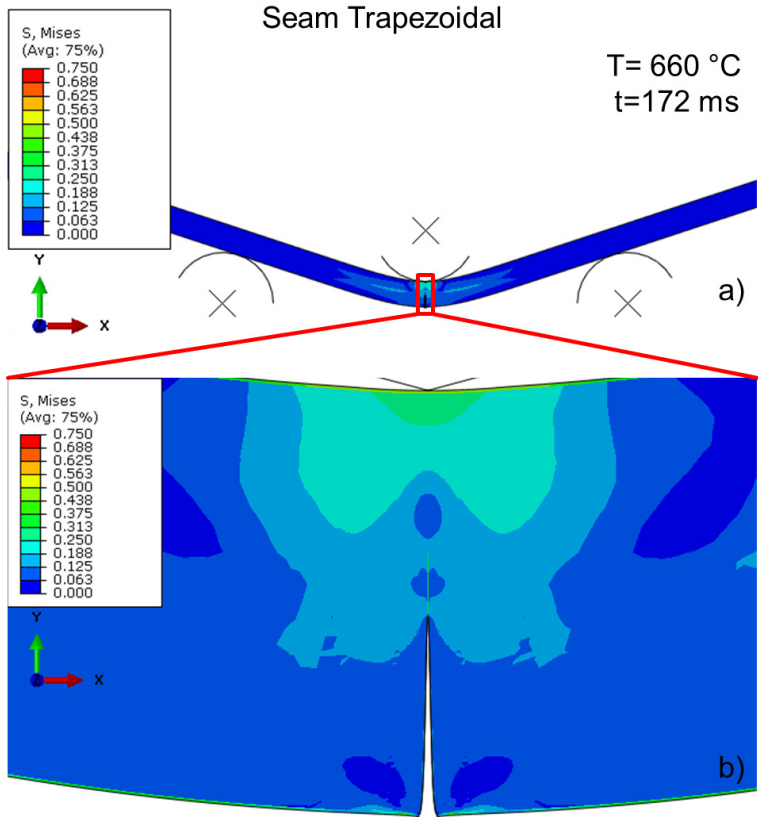


Figure 4-6: Cohesive element seam three point bending test model at 660 °C using a trapezoidal TSL. The plots show the stresses in GPa of a) the bending area and b) the crack area at a time of 172 ms, when the simulation is aborted.

Similar to the simulation at 510 °C, the force-displacement plot of the punch reference point is assessed for the different simulation approaches. Figure 4-7 reveals the same minor difference in stiffness between the surface-based and the element-based techniques. Also the stepping of the cohesive seam model is again observed in the ascending part of the curve. Contrary to the trapezoidal traction-separation laws, the triangular TSL with cohesive contact is aborted before any decline in force. As mentioned previously, this could be the case because of the excessive element distortion during spike formation. Additionally, the plot of the triangular TSL differs significantly from the trapezoidal ones in peak force and peak displacement. Although both trapezoidal cohesive laws predict virtually the same fracture behaviour, the contact formulation seems to lose stiffness at a slightly slower rate than the element based approach. The trapezoidal cohesive contact formulation would probably mirror the element-based model further, had the crack not run into the tied upper half of the model. This point, where further crack growth is prohibited by the tie constraint, is

marked in Figure 4-7, alongside with the point of rapid crack growth. The end of the plotted curves marks the respective abortion of the simulations.

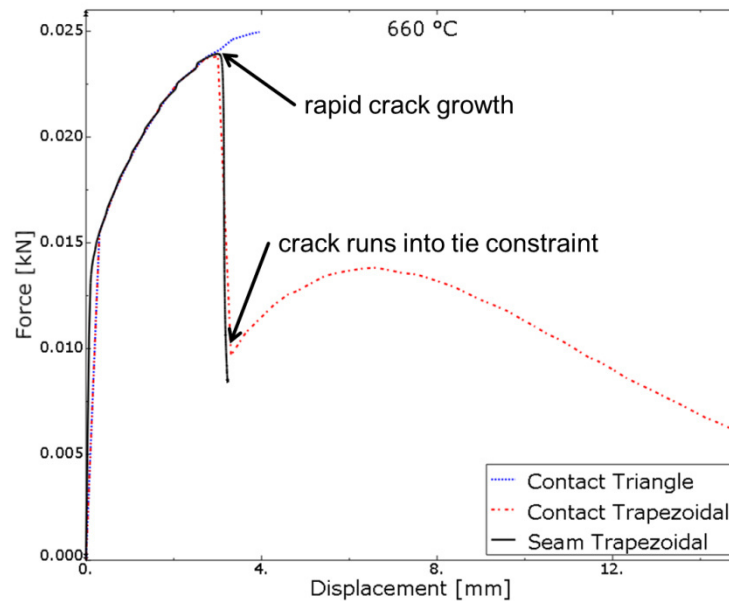


Figure 4-7: Force-displacement relation for different TSL forms and implementations of the cohesive law in the 660 °C three point bending test. The point of rapid crack growth and also the one where the crack for Contact Trapezoidal runs into the tie constraint are clearly visibly.

#### 4.1.3 Summary of the three point bending test simulation

To sum up the investigations made in this chapter, the test at 510 °C showed full convergence for all approaches at little to no crack growth. Whereas triangular and trapezoidal shaped cohesive laws for the contact formulation yielded exactly the same results in this setup, the inserted element seam with trapezoidal TSL already showed a slightly higher stiffness. This increase in stiffness, most likely due to thickness effects, is again repeated in the 660 °C simulation, together with the less smooth stepping behaviour of the element-based simulation. While both test temperatures revealed some kind of bulging of the initial crack surfaces, the simulation at the higher temperature also showed that triangular and trapezoidal cohesive laws do exhibit a difference as soon as it comes to faster crack growth, whereas the form of implementation, i.e. either cohesive seam or cohesive contact, only has a minor influence on this behaviour. Finally, the problem of spike formation is also encountered during the 660 °C simulation with triangular TSL and cohesive contact. It is therefore concluded for all the aforementioned reasons that a cohesive contact formulation with trapezoidal TSL is best suited for further calculations, as it seems to be the most stable option.

## 4.2 Press-hardening crack growth simulation

Already outlined in section 3.3, the submodel technique is utilized for the simulation of crack growth during press-hardening. Before comparing different model positions, it is first determined whether a combined displacement- and force-based submodel approach or an approach partly taking into account the contact with the forming tools is more beneficial. In an attempt to counteract the bulging observed in the three point bending test simulation, the SLIDER multipoint constraint is implemented in the model without tools in order to maintain a flat surface. However, this constraint is not added in the model with tool contact where the contact with the tools is expected to avoid that problem.

Before addressing the results obtained from the used models, it should be mentioned that for the sake of convergence studies a much smaller submodel and deformable tools were tested. As the submodel was so small in width that the cohesive zone was too close to the boundary and therefore had poor stability and cross influence effects, i.e. the boundary condition interfering with the cracking area and vice versa, thus had to be abandoned. Also artificial edges on the curved parts of the tools imposed through the meshing caused the mesh points of the tools to hook into one side of the initial crack and therefore lead to unphysical behaviour and instability of the calculation. Both the described problems are highlighted in Figure 4-8.

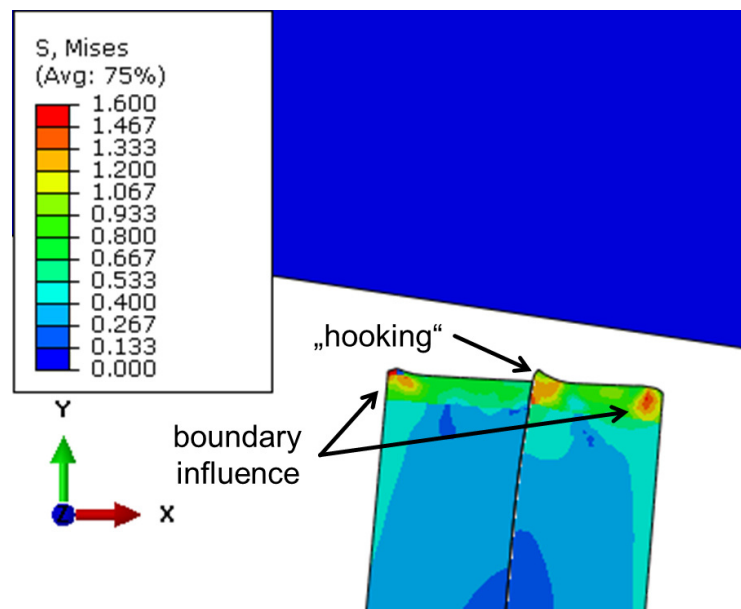


Figure 4-8: Von-Mises stress plot in GPa showing the boundary influence of a too small model and the “hooking” of the deformable tools mesh with the free crack surface.

#### 4.2.1 Submodel boundary condition vs. tool interaction

As a first attempt to overcome the bulging as well as the hooking observed in other models, the submodel with cohesive contact interaction placed at  $x=102,5$  mm is simulated. However, this modelling approach causes abortion of the calculation at 656 ms, most likely due to excessive crack growth, and does not hinder bulging as hoped for. The position of the submodel at the point of job abortion can be seen in Figure 4-9 a), whereas the magnification of the crack in b) clearly shows the aforementioned bulging problem.

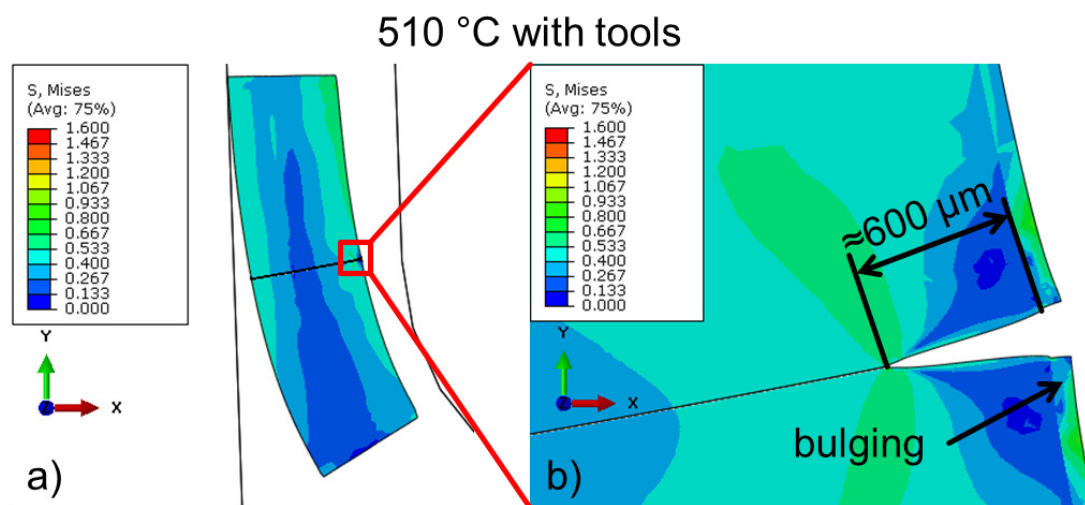


Figure 4-9: Cohesive contact submodel at  $x=102,5$  mm during the press-hardening process with tool contact. The plot shows the von-Mises stress in GPa of a) the whole submodel with tools and b) the crack area at the point of job abortion at 656 ms.

Contrary to the submodel with tool contact, the one with the force-based submodel boundary condition on the top and bottom surface and SLIDER MPC fully converges. Placed at the same  $x=102,5$  mm as the model with tools, the end position at 805 ms is displayed in Figure 4-10 a). The magnification of the crack in Figure 4-10 b) shows that the surface around the crack remains straight due to the SLIDER MPC. However, this imposes a deformation on the boundary between the zinc layer and the steel substrate, which is also the transition region from the initial crack to the growing crack. Nevertheless, the crack growth seems to be stabilized by this and the crack only extends about 8 μm into the steel, as opposed to the roughly 600 μm for the tool contact model.

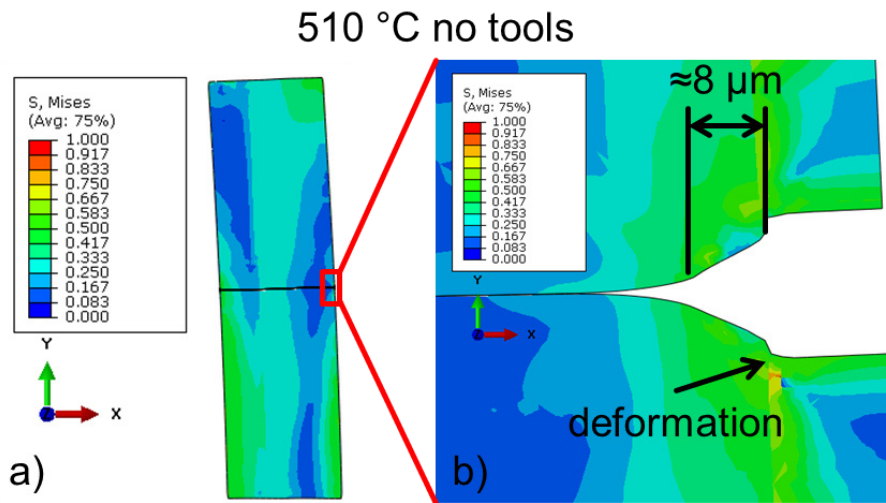


Figure 4-10: Press-hardening submodel at  $x=102,5$  mm without tool contact. The model exhibiting cohesive contact is shown in the final position at 805 ms. Both a) the whole submodel and b) the crack area show the von-Mises stress plot in GPa.

As for 510 °C, the calculation for 660 °C modelled with tool contact interaction is aborted at roughly the same time, i.e. 651 ms, although showing significantly less crack extension of about 22  $\mu\text{m}$  into the steel substrate. Magnifying the stress plot of the whole model displayed in Figure 4-11 a) onto the crack in b) reveals a stress concentration just outside the bulging zone around the crack, which is also slightly visible for 510 °C in Figure 4-9 b). Either this concentration of stress or potential rapid crack growth is assumed to be responsible for job abortion.

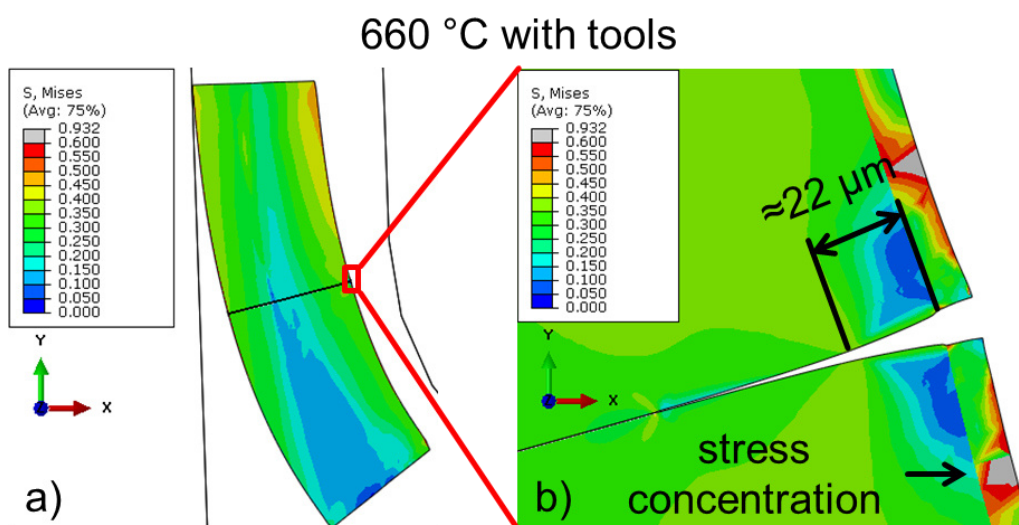


Figure 4-11: The press-hardening process with tool interaction for a submodel at  $x=102,5$  mm with cohesive contact. The von-Mises stress in GPa of a) the whole submodel with tools and b) the magnification of the crack area is plotted for the point of job abortion at 651 ms.

As opposed to the same modelling approach at 510 °C with this SLIDER MPC, the calculation for 660 °C has not completed, but abandoned at 611 ms most likely due to excessive stress concentration. Said effect can be clearly related to the SLIDER MPC, as shown in Figure 4-12 b). Both the whole model display and the close-up view on the potential crack area in Figure 4-12 a) and b) do not indicate any crack growth at all. Therefore the assumption about the concentration and unsteady transition of stress at both MPC ends being responsible for the unstable calculation seems valid.

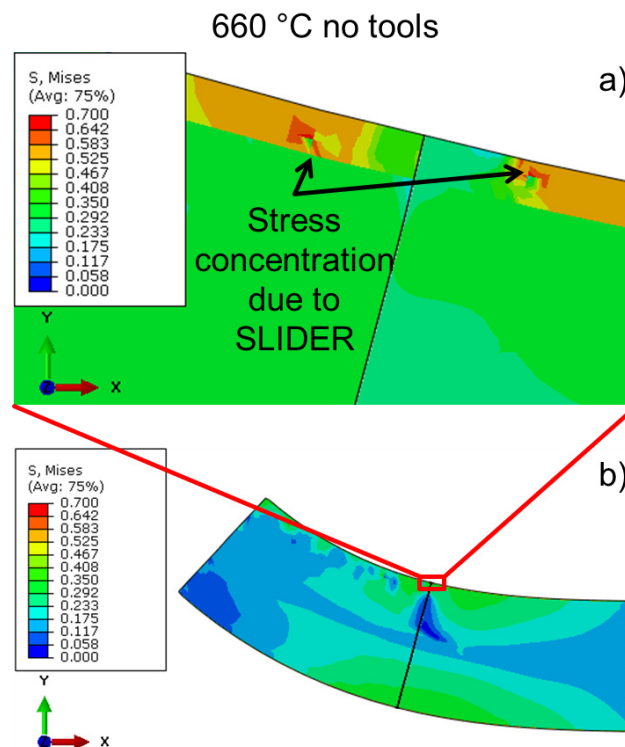


Figure 4-12: Submodel with force-based submodel boundary condition on the upper and lower surface for press-hardening simulation. From initial position  $x=102,5$  mm a) the potential cracking area and b) the full submodel are displayed. The von-Mises stress plot in GPa is taken at 611 ms, the point in time when calculation is abandoned.

In Figure 4-13 below the damage variable CSDMG from the slave surface is visualized as a function of the true distance alongside the predetermined crack path. As the first node being damaged is about one micron below the initial crack with length 10  $\mu\text{m}$ , CSDMG may only change in value from this point on. A value of zero indicates either undamaged cohesive behaviour or the initial crack, whereas unity denotes full damage. The crack lengths are measured from the coating interface at 10  $\mu\text{m}$  into the substrate and end where CSDMG is less than unity. Besides the two well identifiable values, Figure 4-13 also shows that no damage at all occurs for the model without tools at 660 °C. Other than that, the crack length



for the tool contact model at 510 °C exceeds the scale of the plot, but was determined as approximately 600  $\mu\text{m}$  in a similar manner on a larger scale figure.

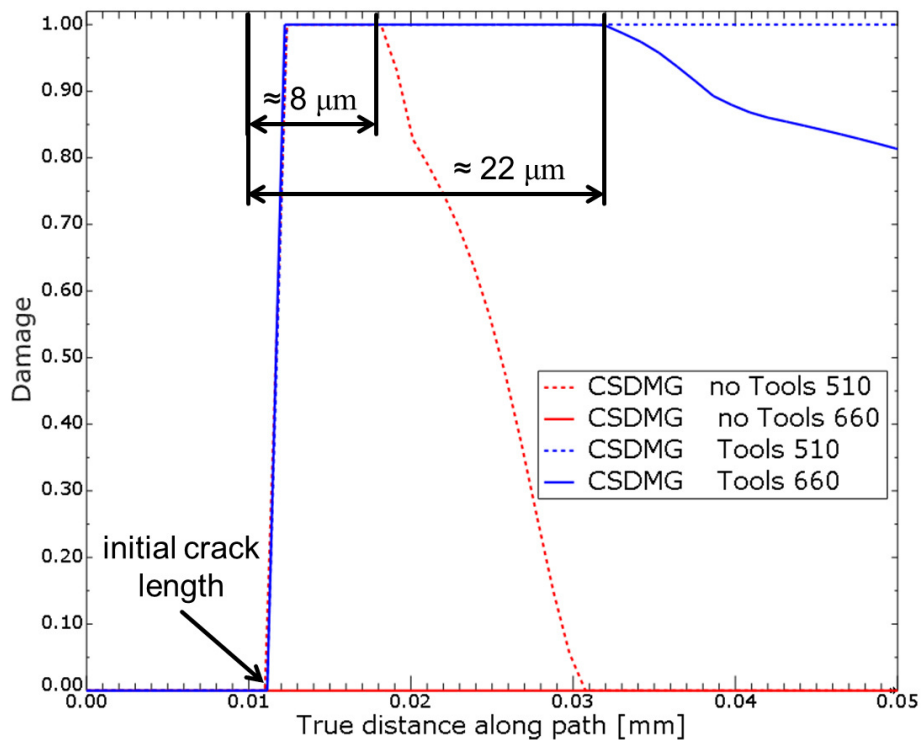


Figure 4-13: Slave surface damage variable CSDMG for tool interaction and submodel boundary condition approach at different temperatures. Damage is plotted against the true distance from the submodel top surface alongside the predefined crack path.

In conclusion, the model with tool contact interactions might be more desirable, because it can capture frictional contact between the model and the tools. However, the bulging around the crack cannot be avoided as expected with this model and it abandons calculation at roughly the same point regardless of the temperature. Furthermore the crack length of 600  $\mu\text{m}$  obtained at 510 °C does not seem to be very realistic. Although a lot of the calculation instabilities may stem from non-calibrated material data, especially for the traction-separation law, the submodel approach substituting the tool contact interactions with a force-based submodel boundary condition and SLIDER MPC is regarded as more stable in this calculation. On the one hand, it did fail earlier for 660 °C, but on the other, it was able to fully calculate the 510 °C simulation with a somewhat reasonable crack length. Also stress concentrations, which may lead to premature abortion of calculation, arise in both modelling approaches. In this regard no model approach has a clear advantage over the other.



## 4.2.2 Comparison of crack positions for 510 °C

After investigation of different modelling techniques, multiple positions are evaluated regarding their cracking behaviour. The cohesive contact submodel with trapezoidal TSL and no tool interaction is placed on three different positions according to the work of Tomasch et al. [69]. For these positions, simulations are carried out at 510 °C, as the calculation seems to be more stable for this temperature. Figure 4-14 a) displays the final crack positions on the blank, corresponding to different x-values as indicated in Figure 3-9 from section 3.3. Crack lengths for different positions are measured from the damage variable plot in Figure 4-14 b).

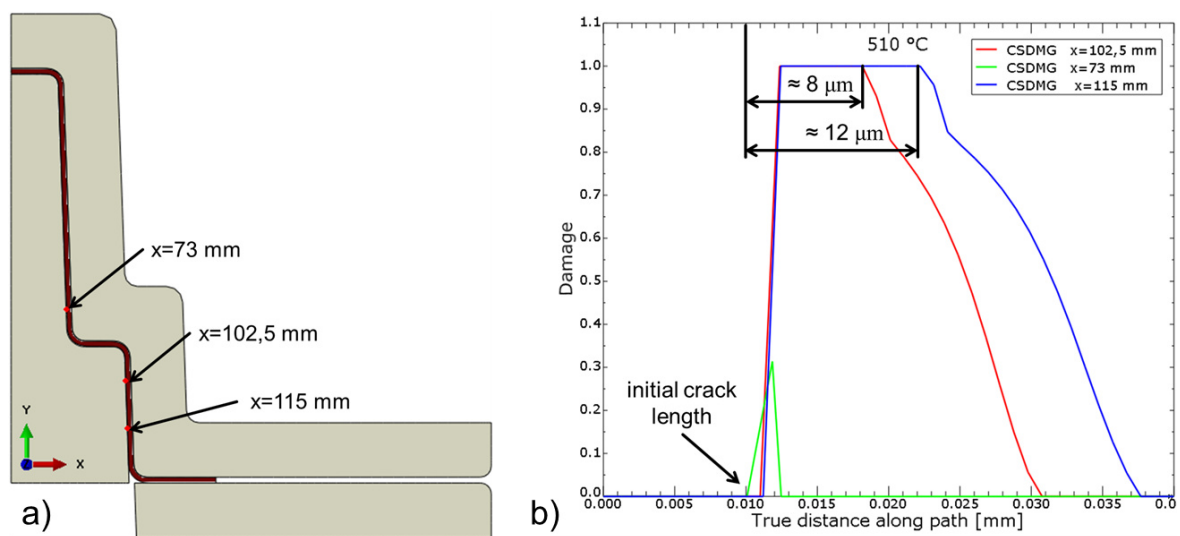


Figure 4-14: For the simulation without tool contact at 510 °C a) the matching end positions of the crack for different x-values in the original framework and b) the corresponding damage variable plot alongside the crack path are displayed.

Taken from Figure 4-14 b), the measured crack lengths are indicated in Figure 4-15. Both simulations at x=102,5 mm and 115 mm are displayed for the end point of 805 ms, whereas the calculation for x=73 mm aborted prematurely at 708 ms. The reason for that could be the onset of rapid crack growth at this time of the simulation due to bending. Figure 4-15 b) also indicates the start of damage development at this time. Nonetheless, the other two positions can successfully be compared at their final state, indicating that the outer side of the blank is more prone to cracking at x=115 mm than at x=102,5 mm.

In summary, some approaches to study crack growth during press-hardening have been developed. The finally proposed simulation technique could easily be applied to study multiple areas and temperatures regarding their cracking behaviour. The submodel could also be transferred to whatever tool geometry is desired, as long as the blank thickness remains constant.

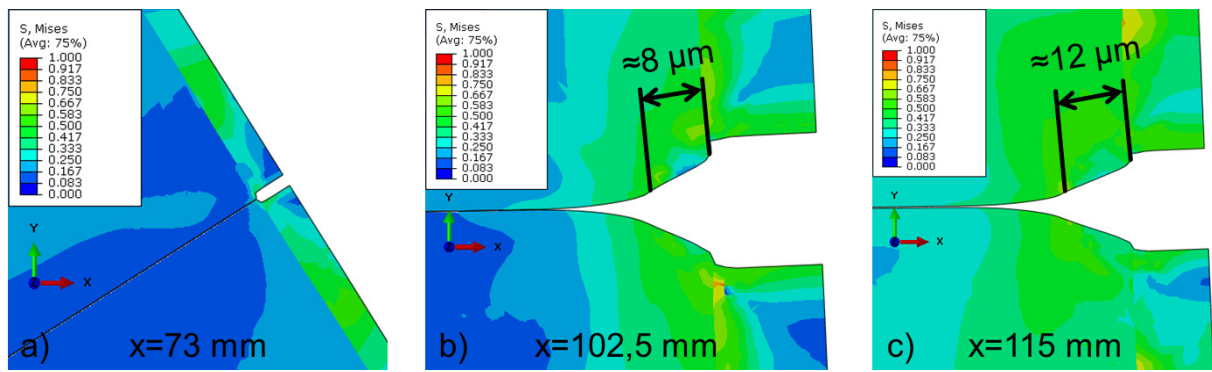


Figure 4-15: Magnifications of the crack region for different x-values. The von-Mises plot in GPa for position a) is shown at the state of job abortion at 708 ms, whereas b) and c) both display the crack at the final time of 805 ms.

## 5 Conclusion

In this thesis, the importance of direct press-hardening of coated steel for the automotive industry and the resulting danger of liquid metal embrittlement and crack growth is shortly addressed as introduction to this topic. A first thorough study on different ways to describe cracks in ABAQUS is carried out and the cohesive model is chosen to study crack growth in highly ductile material. By taking multiple modelling approaches in a three point bending test simulation, the cohesive contact formulation together with a trapezoidal traction-separation law for ductile material proved to be the most stable simulation technique. The three point bending test model not only serves the purpose of assessing different cohesive modelling techniques, but should also provide a possibility to calibrate the needed data with the aid of real material tests.

Investigation of the three point bending test simulations revealed a stepping behaviour in the force-displacement relation for cohesive elements. The same relation also indicates the clearly different behaviour of triangular and trapezoidal traction-separation laws. Additionally, the three point bending test serves to reveal possible difficulties that may arise during crack growth calculations, like bulging or spike formation.

Further development aims to investigate the cracking behaviour of different position on an already established press-hardening simulation model, created by Tomasch et al. [69; 70]. Thereby it is found that although deformable tools are necessary in the coupled-temperature simulation of the global model, rigid tools perform better in the crack simulation with the submodel, as no artificial “hooking” of mesh points takes place. The submodel also should be large enough in order to prevent interference effects from the cracking area on the boundary condition and vice versa. Ultimately, a force-based submodel boundary condition and SLIDER multipoint constraint replacing the tool contact interaction yield the best results regarding convergence behaviour and crack extension.

As best practice to study crack growth in larger-scale models it could be stated that a coupled temperature-displacement simulation of the original model is to be carried out first, which later drives the boundary condition as well as the temperature distribution of the crack-containing submodel. This submodel can later on be placed to investigate different regions of the original model regarding crack growth.

Establishing a reasonable traction-separation law without any physical tests for calibration, but solely relying on literature values, proved to be the most challenging part of this thesis. However, as mentioned before, the three point bending test model should provide also a

reasonable opportunity to calibrate material data, as done by Sung et al. [59] and Vanapalli et al. [62]. Once the traction-separation law is thoroughly calibrated, the developed model can further be extended with diffusion models (Sedlak et al. [55]) or phase transformation behaviour (Issa et al. [56]).

## 6 Literature

- [1] *Taylor, T., Clough, A.*: Critical review of automotive hot-stamped sheet steel from an industrial perspective. *Materials Science and Technology* 34 (2017), S. 809–861.
- [2] *Giampieri, A., Ling-Chin, J., Ma, Z., Smallbone, A., Roskilly, A. P.*: A review of the current automotive manufacturing practice from an energy perspective. *Applied Energy* 261 (2020), S. 114074.
- [3] *Billur, E.* (Hg.): *Hot Stamping of Ultra High-Strength Steels. From a Technological and Business Perspective.* Cham: Springer International Publishing 2019.
- [4] *Demeri, M. Y.*: *Advanced high-strength steels. Science, technology, and applications.* Materials Park, Ohio: ASM International 2013.
- [5] *Radlmayr, K. M., Kelsch, R., Sommer, A., Rouet, C., Kurz, T., Faderl, J.*: *Warmumformung verzinkter Stähle.*  
<https://www.voestalpine.com/ultralights/Produkte/Warmumformung>.
- [6] *Zhao, J., Jiang, Z.*: *Rolling of Advanced High Strength Steels. Theory, Simulation and Practice.* Portland: Taylor and Francis 2017.
- [7] *Hou, Z. R., Opitz, T., Xiong, X. C., Zhao, X. M., Yi, H. L.*: Bake-partitioning in a press-hardening steel. *Scripta Materialia* 162 (2019), S. 492–496.
- [8] *Aziz, N., Aqida, S. N.*: Optimization of quenching process in hot press forming of 22MnB5 steel for high strength properties for publication in. *IOP Conference Series: Materials Science and Engineering* 50 (2013), S. 12064.
- [9] *Tisza, M.*: Hot Forming of Boron Alloyed Manganese Steels. *Materials Science Forum* 885 (2017), S. 25–30.
- [10] *Hwang, B., Suh, D.-W., Kim, S.-J.*: Austenitizing temperature and hardenability of low-carbon boron steels. *Scripta Materialia* 64 (2011), S. 1118–1120.
- [11] *Degner, M.*: *Steel manual.* Düsseldorf: Verl. Stahleisen 2008.
- [12] *Ginzburg, V. B.*: *Metallurgical design of flat rolled steels.* New York: Dekker 2005.
- [13] *Inui, H., Okamoto, N. L., Yamaguchi, S.*: Crystal Structures and Mechanical Properties of Fe–Zn Intermetallic Compounds Formed in the Coating Layer of Galvannealed Steels. *ISIJ International* 58 (2018), S. 1550–1561.

- [14] *Marder, A. R.*: The metallurgy of zinc-coated steel. *Progress in Materials Science* (2000), S. 191–271.
- [15] *Han, K., Ohnuma, I., Okuda, K., Kainuma, R.*: Experimental determination of phase diagram in the Zn-Fe binary system. *Journal of Alloys and Compounds* 737 (2018), S. 490–504.
- [16] *Pokorny, P., Kolisko, J., Balik, L., Novak, P.*: Description of Structure of Fe-Zn Intermetallic Compounds Present in Hot-Dip Galvanized Coatings on Steel. *METALURGIJA* 54 (2015), S. 707–710.
- [17] *Peng, H., Peng, W., Lu, R., Wu, G., Zhang, J.*: Diffusion and cracking behavior involved in hot press forming of Zn coated 22MnB5. *Journal of Alloys and Compounds* 806 (2019), S. 195–205.
- [18] *Okamoto, N. L., Inomoto, M., Takebayashi, H., Inui, H.*: Crystal structure refinement of the  $\Gamma$ - and  $\Gamma$ 1-phase compounds in the Fe-Zn system and orientation relationships among  $\alpha$ -Fe,  $\Gamma$  and  $\Gamma$ 1 phases in the coating layer of galvanized steel. *Journal of Alloys and Compounds* 732 (2018), S. 52–63.
- [19] *Goldbeck, O. K.*: IRON-Binary Phase Diagrams. Berlin, Heidelberg, s.l.: Springer Berlin Heidelberg 1982.
- [20] *Hu, X., Watanabe, T.*: Relationship between the Crystallographic Structure of Electrodeposited Fe-Zn Alloy Film and Its Thermal Equilibrium Diagram. *MATERIALS TRANSACTIONS* 42 (2001), S. 1969–1976.
- [21] *Okamoto, N. L., Kashioka, D., Inomoto, M., Inui, H., Takebayashi, H., Yamaguchi, S.*: Compression deformability of  $\Gamma$  and  $\zeta$  Fe–Zn intermetallics to mitigate detachment of brittle intermetallic coating of galvanized steels. *Scripta Materialia* 69 (2013), S. 307–310.
- [22] *Okamoto, N. L., Michishita, S., Hashizume, Y., Inui, H.*: Fracture Toughness of the Fe–Zn Intermetallic Compounds Measured by Bend Testing of Chevron-Notched Single-Crystal Microbeams. *ISIJ International* 58 (2018), S. 1569–1577.
- [23] *He, J., Lian, J., Aretz, A., Vajragupta, N., Hangen, U., Goodwin, F., Münstermann, S.*: Fracture properties of zinc coating layers in a galvanized steel and an electrolytically galvanized steel. *Materials Science and Engineering: A* 732 (2018), S. 320–325.
- [24] *Golling, S., Frómeta, D., Casellas, D., Jonsén, P.*: Influence of microstructure on the fracture toughness of hot stamped boron steel. *Materials Science and Engineering: A* 743 (2019), S. 529–539.

- [25] Grydin, O., Andreiev, A., Holzweißig, M. J., Rüsing, C. J., Duschik, K., Frolov, Y., Schaper, M.: Short austenitization treatment with subsequent press hardening. Correlation between process parameters, microstructure and mechanical properties. *Materials Science and Engineering: A* 749 (2019), S. 176–195.
- [26] Wang, Z., Wang, K., Liu, Y., Zhu, B., Zhang, Y., Li, S.: Multi-scale simulation for hot stamping quenching & partitioning process of high-strength steel. *Journal of Materials Processing Technology* 269 (2019), S. 150–162.
- [27] Cho, L., Kang, H., Lee, C., Cooman, B. C. de: Microstructure of liquid metal embrittlement cracks on Zn-coated 22MnB5 press-hardened steel. *Scripta Materialia* 90-91 (2014), S. 25–28.
- [28] Razmpoosh, M. H., Macwan, A., Biro, E., Chen, D. L., Peng, Y., Goodwin, F., Zhou, Y.: Liquid metal embrittlement in laser beam welding of Zn-coated 22MnB5 steel. *Materials & Design* 155 (2018), S. 375–383.
- [29] Mechanics - Microstructure - Corrosion Coupling. Concepts, Experiments, Modeling and Cases: ISTE Press LTD - ELSEVIER 2019.
- [30] Koutromanos, I.: Fundamentals of finite element analysis. Linear finite element analysis. Hoboken, NJ, Chichester: Wiley 2018.
- [31] Klein, B.: FEM. Grundlagen und Anwendungen der Finite-Element-Methode im Maschinen- und Fahrzeugbau. Wiesbaden: Vieweg+Teubner Verlag 2012.
- [32] Zienkiewicz, O. C., Zhu, J. Z., Taylor, R. L.: The finite element method. Its basis and fundamentals. Oxford, UK: Butterworth-Heinemann 2013.
- [33] ABAQUS documentation. [www.simulia.com](http://www.simulia.com).
- [34] Belytschko, T., Black, T.: Elastic crack growth in finite elements with minimal remeshing. *International Journal for Numerical Methods in Engineering* 45 (1999), S. 601–620.
- [35] Du, Z.-z.: eXtended Finite Element Method (XFEM) in Abaqus.
- [36] Heidari-Rarani, M., Sayedain, M.: Finite element modeling strategies for 2D and 3D delamination propagation in composite DCB specimens using VCCT, CZM and XFEM approaches. *Theoretical and Applied Fracture Mechanics* 103 (2019), S. 102246.
- [37] Dugdale, D. S.: Yielding of steel sheets containing slits. *Journal of the Mechanics and Physics of Solids* 8 (1960), S. 100–104.

- [38] *Barenblatt, G. I.*: The Mathematical Theory of Equilibrium Cracks in Brittle Fracture. In: Dryden, H. L., Karman, T. von (Hg.): Advances in applied mechanics. New York: Academic P, S. 55–129.
- [39] *Cornec, A., Scheider, I., Schwalbe, K.-H.*: On the practical application of the cohesive model. *Engineering Fracture Mechanics* 70 (2003), S. 1963–1987.
- [40] *Scheider, I.*: Cohesive model for crack propagation analyses of structures with elastic–plastic material behavior. *Foundations and implementation* 2001.
- [41] *Ajinkya K. Salve, Sudhindra N. Jalwadi*: Implementation of Cohesive Zone in ABAQUS to Investigate Fracture Problems.
- [42] *Ibrahim, G. R., Albarbar, A.*: A new approach to the cohesive zone model that includes thermal effects. *Composites Part B: Engineering* 167 (2019), S. 370–376.
- [43] *Chakraborty, P., Biner, S. B.*: A unified cohesive zone approach to model the ductile to brittle transition of fracture toughness in reactor pressure vessel steels. *Engineering Fracture Mechanics* 131 (2014), S. 194–209.
- [44] *Park, K., Choi, H., Paulino, G. H.*: Assessment of cohesive traction-separation relationships in ABAQUS. A comparative study. *Mechanics Research Communications* 78 (2016), S. 71–78.
- [45] *Turon, A., Davila, C. G., Camanho, P. P., Costa, J.*: An Engineering Solution for solving Mesh Size An engineering solution for mesh size effects in the simulation of delamination using cohesive zone models (2005).
- [46] *Song, K.*: Guidelines and Parameter Selection for the Simulation of Progressive Delamination 2008.
- [47] *Uthaisangasuk, V., Prah, U., Bleck, W.*: Micromechanical modelling of damage behaviour of multiphase steels. *Computational Materials Science* 43 (2008), S. 27–35.
- [48] *Scheider, I.*: Derivation of separation laws for cohesive models in the course of ductile fracture. *Engineering Fracture Mechanics* 76 (2009), S. 1450–1459.
- [49] *Turon, A., Camanho, P. P., Costa, J., Renart, J.*: Accurate simulation of delamination growth under mixed-mode loading using cohesive elements. Definition of interlaminar strengths and elastic stiffness. *Composite Structures* 92 (2010), S. 1857–1864.
- [50] *Turon, A., Camanho, P. P., Costa, J., Dávila, C. G.*: A damage model for the simulation of delamination in advanced composites under variable-mode loading. *Mechanics of Materials* 38 (2006), S. 1072–1089.



- [51] *Harper, P. W., Sun, L., Hallett, S. R.*: A study on the influence of cohesive zone interface element strength parameters on mixed mode behaviour. *Composites Part A: Applied Science and Manufacturing* 43 (2012), S. 722–734.
- [52] *Heidari-Rarani, M., Ghasemi, A. R.*: Appropriate shape of cohesive zone model for delamination propagation in ENF specimens with R-curve effects. *Theoretical and Applied Fracture Mechanics* 90 (2017), S. 174–181.
- [53] *Tvergaard, V., Hutchinson, J. W.*: The relation between crack growth resistance and fracture process parameters in elastic-plastic solids. *Journal of the Mechanics and Physics of Solids* 40 (1992), S. 1377–1397.
- [54] *Jemblie, L., Olden, V., Akselsen, O. M.*: A coupled diffusion and cohesive zone modelling approach for numerically assessing hydrogen embrittlement of steel structures. *International Journal of Hydrogen Energy* 42 (2017), S. 11980–11995.
- [55] *Sedlak, M., Alfredsson, B., Efsing, P.*: A coupled diffusion and cohesive zone model for intergranular stress corrosion cracking in 316L stainless steel exposed to cold work in primary water conditions. *Engineering Fracture Mechanics* 217 (2019), S. 106543.
- [56] *Issa, S., Eliasson, S., Lundberg, A., Wallin, M., Hallberg, H.*: Cohesive zone modeling of crack propagation influenced by martensitic phase transformation. *Materials Science and Engineering: A* 712 (2018), S. 564–573.
- [57] *Scheider, I.*: Micromechanical based derivation of traction-separation laws for cohesive model simulations. *Procedia Engineering* 1 (2009), S. 17–21.
- [58] *Borst, R. de*: Numerical aspects of cohesive-zone models. *Engineering Fracture Mechanics* 70 (2003), S. 1743–1757.
- [59] *Sung, S.-J., Pan, J., Korinko, P. S., Morgan, M., McWilliams, A.*: Simulations of fracture tests of uncharged and hydrogen-charged additively manufactured 304 stainless steel specimens using cohesive zone modeling. *Engineering Fracture Mechanics* 209 (2019), S. 125–146.
- [60] *Viggo Tvergaard*: Theoretical investigation of the effect of plasticity on crack growth along a functionally graded region between dissimilar elastic–plastic solids. *Engineering Fracture Mechanics* 69 (2002), S. 1635–1645.
- [61] *Janssen, M., Zuidema, J., Wanhill, R. J. H.*: *Fracture mechanics*. London, New York: Spon Press 2004.

- [62] *Vanapalli, V. T., Dutta, B. K., Chattopadhyay, J., Jose, N. M.*: Stress triaxiality based transferability of cohesive zone parameters. *Engineering Fracture Mechanics* 224 (2020), S. 106789.
- [63] *Wu, W., Wang, Y., Tao, P., Li, X., Gong, J.*: Cohesive zone modeling of hydrogen-induced delayed intergranular fracture in high strength steels. *Results in Physics* 11 (2018), S. 591–598.
- [64] *M. Elices, G.V. Guinea, J. Gómez, J. Planas*: The cohesive zone model: advantages, limitations and challenges. *Engineering Fracture Mechanics* 69 (2002), S. 137–163.
- [65] *Vanapalli, V. T., Chattopadhyay, J., Jose, N. M., Dutta, B. K.*: Determination and verification of triaxiality dependent cohesive zone parameters of SA333 Grade 6 steel. *Procedia Structural Integrity* 14 (2019), S. 521–528.
- [66] *Pandolfi, A., Guduru, P. R., Ortiz, M., Rosakis, A. J.*: Three dimensional cohesive-element analysis and experiments of dynamic fracture in C300 steel. *International Journal of Solids and Structures* 37 (2000), S. 3733–3760.
- [67] *Dakshinamurthy, M., Ma, A.*: Crack propagation in TRIP assisted steels modeled by crystal plasticity and cohesive zone method. *Theoretical and Applied Fracture Mechanics* 96 (2018), S. 545–555.
- [68] *Wang, Y. J., Ru, C. Q.*: Determination of two key parameters of a cohesive zone model for pipeline steels based on uniaxial stress-strain curve. *Engineering Fracture Mechanics* 163 (2016), S. 55–65.
- [69] *Tomasch, M., Antretter, T., Pichler, M., Ecker, W.*: Scanning electron microscope investigation on zinc induced cracks of coated press hardened components: 12th International Conference on Zinc & Zinc Alloy Coated Steel Sheet - GALVATECH 2021.
- [70] *Tomasch, M., Ecker, W., Kaiser, R., Antretter, T.*: Deep drawing of press hardening steels. *Journal of Physics: Conference Series* 1063 (2018), S. 12038.
- [71] *Olden, V., Thaulow, C., Johnsen, R., Østby, E., Berstad, T.*: Influence of hydrogen from cathodic protection on the fracture susceptibility of 25%Cr duplex stainless steel – Constant load SENT testing and FE-modelling using hydrogen influenced cohesive zone elements. *Engineering Fracture Mechanics* 76 (2009), S. 827–844.
- [72] *Huan Li, Huang Yuan (Hg.)*: Simulation of fracture and fatigue damage in stainless steel 304 using a cohesive zone model 2013.